UNIVERSITY OF CALIFORNIA
RIVERSIDE

Electrical Transport of Topological Insulator-Bi_2Se_3 and Thermoelectric Properties of Graphene

A Dissertation submitted in partial satisfaction
of the requirements for the degree of

Doctor of Philosophy

in

Physics

by

Peng Wei

June 2011

Thesis Committee:
Prof. Jing Shi, Chairperson
Prof. Jeanie Lau
Prof. Chandra Varma

The Dissertation of Peng Wei is approved:

Committee Chairperson

University of California, Riverside

Acknowledgements

I am very grateful to my advisor Prof. Jing Shi's for his support and advice on my Ph.D. studies in his group. Without his support, I can not achieve these. I have learned a lot from him. He guides me all the way along my research work and leads me through many difficulties that I have encountered during my research projects. Working with him, I can feel his dedication as a physicist and whole hearted support as an advisor. Besides these, I find great helpful by talking and discussing with him. He has a good sense on physics and can always raises good questions that stimulated me to think further on my researches. His ingenious suggestions on my experiments have also helped me many times in solving difficult experimental problems. It is my great pleasure to work with Prof. Jing Shi during the six years on my Ph.D. study of physics.

I would like to thank my committee members, Prof. Jeanie Lau and Prof. Chandra Varma. Thank you very much for your support. I find really helpful in interacting with all the members of my committee. I would like to thank Prof. Chandra Varma for those great discussions on physics topics and physics concepts related to my research. Those discussions have brought me a dramatically deeper view of physics on my research areas. I would like to thank Prof. Jeanie Lau for her great suggestions on my experiments. I have learned many useful experimental techniques from her.

I would also like to thank the professors in our physics department. In fact, I feel really enjoyed in interacting with them. Thanks to Prof. Vivek Aji for those many discussions on the physics of topological insulators. Thanks to Prof. Kirill Shtengel for the discussions on Majorana Fermions. Thanks to Prof. Allen Mills for his great ideas on the device fabrications of Bi_2Se_3. Thanks to Prof. Ward Beyermann for those many helpful discussions and suggestions on the experiments of my research projects. Thanks to Prof. Leonid Pryadko for the discussions on quantum Hall effect and Shubnikov-de Haas oscillations. Thanks to Prof. Shan-Wen Tsai for the discussions on the thermoelectric properties of graphene. Thanks to Prof. Marc Bockrath for the discussions on the nano-fabrication skills.

Thanks to all my labmates and friends in the physics department. First, I would like to thank Dr. Di Wu for teaching me many useful experimental skills and for working together on many research projects. I would like to specially thank to my labmate Zhiyong Wang for working together on our projects of topological insulators. I would also like to specially thank to Wenzhong Bao for working together on our project of graphene thermoelectrics. I would also like to thank many others. They are Yong Pu, Tao Lin, Xinfei Liu, Deqi Wang, Zuhong Xiong, Hamad Mohamed Al Yahyaei, Raymond Sachs, Vincent Ugarte, Gang Liu, Yan Li, Keyu Pi, Dong Gui, Wei Han, Jairo Velasco, Hulya Atmacan, Mayra Tovar, Ling Yang, Henry Choi, Kyungwook Kim and many other friends.

I would like to thank my wife Hsiang-Ku Lin for her love and for those discussions and debates on many physics topics.

In the end and in the most, I would like to thank my parents for their love and support.

ABSTRACT OF THE DISSERTATION

Electrical Transport of Topological Insulator-Bi_2Se_3 and Thermoelectric Properties of Graphene

by

Peng Wei

Doctor of Philosophy, Graduate Program in Physics
University of California, Riverside, June 2011
Dr. Jing Shi, Chairperson

This thesis summarizes our work in the past four years in the field of transport studies of the topological insulator materials and thermoelectric properties of graphene. The first half of the thesis is focused on the transport properties of topological insulator material-Bi_2Se_3. In our research, we systematically tune the position of the chemical potential in p-type Ca-doped Bi_2Se_3 thin devices first by eliminating excess holes with controlled post-fabrication electron beam irradiation that results in an insulating bulk state. In spite of the fact that the energetic electron beam creates defects to localize the bulk carriers and inevitably to cause additional scattering, we find a tenfold increase in carrier mobility associated with the extended states in the band gap. In addition, the resistance undergoes a fivefold increase and passes the maximum as the chemical potential is further tuned by electrostatic gating. A cusp-like low-field magnetoresistance feature also emerges which is indicative of strong spin-orbit interaction. The observed gate-tunable high-mobility is a signature of massless Dirac fermions in the band gap of Bi_2Se_3.

The second half of this thesis is focused on graphene. Our work first reported the thermoelectric study of graphene and demonstrated the anomalous thermoelectric transport of massless Dirac fermions. As a direct consequence of the linear dispersion of massless particles, we find that the Seebeck coefficient S_{xx} diverges with $1/\sqrt{|n_{2D}|}$, where n_{2D} is the carrier density. We observe a very large Nernst signal S_{xy} (~ 50 μV/K at 8 T) at the Dirac point, and an oscillatory dependence of both S_{xx} and S_{xy} on n_{2D} at low temperatures. Our results underscore the anomalous thermoelectric transport in graphene, which may be used as a highly sensitive probe for impurity bands near the Dirac point.

Table of Contents

Chapter 1 Introductions to topological insulator and graphene……..1

1.1 Topological insulator……....2

1.2 Graphene……...6

Chapter 2 Fabrication techniques of Bi_2Se_3 device and experimental setup…….10

2.1 Bi_2Se_3 thin flake preparation……...10

2.1.1 Crystal structure of Bi_2Se_3…….10

2.1.2 Bi2Se3 crystal and thin flake preparation…….12

2.1.3 Thin flake location and identification……...16

2.2 Device fabrications on Bi_2Se_3 thin flake…….19

2.2.1 Strong degradation of Bi_2Se_3 material under ambient condition……..19

2.2.2 LOR protected device fabrication process……21

2.2.3 Low energy electron beam lithography…….24

2.2.4 Lithography free fabrication techniques……...27

2.3 Experimental setup……..30

2.3.1 Device mounting……...30

2.3.2 Electrical transport measurements……31

Chapter 3 Electrical transport properties of the high mobility states in Bi_2Se_3 band gap…...35

3.1 Control the Fermi level in Bi_2Se_3 thin flakes……..35

3.1.1 Issues of the Fermi level modulation……35

3.1.2 Achieve the insulating device and p-type device……..39

3.1.3 The effect of the electron beam irradiation……...41

3.1.4 Fermi level modulation using electrostatic gating……42

3.2 Temperature dependence of the device resistivity and the position of the Fermi level……..44

3.2.1 Experimental data……..45

3.2.2 The model of the temperature dependence……...47

3.2.3 Discussions……51

3.3 Gate dependence of the device resistivity and the field-effect mobility…….52

3.3.1 Experimental data……..52

3.3.2 High mobility states inside the band gap……..53

3.3.3 Discussions……54

3.4 Electrical transport under magnetic field……57

3.4.1 Experimental Data……57

3.4.2 Possible origins of the low field cusp and the modulations through electrostatic gate……59

3.4.3 Signature of the gate tunable Shubnikov de Hass oscillations…….60

3.4.4 Thomas-Fermi screening length……66

Chapter 4 Techniques for the thermoelectric transport measurement in nano-devices……..67

4.1 Introductions to thermoelectric effects……67

4.1.1 Seebeck effect……...68

4.1.2 Peltier effect……..69

4.1.3 Nernst effect……..70

4.1.4 Boltzmann transport equation and thermoelectric coefficients…….71

4.2 Measurements of thermoelectric properties in micron-scale device……...73

4.2.1 Introduction……...73

4.2.2 Design of the micron-scale devices……...75

4.2.3 Design of the device holder in the use under cryogenic environment……..78

4.2.4 Techniques for thermoelectric measurements……...82

4.2.5 Nernst signal under magnetic field……89

Chapter 5 Anomalous thermoelectric transport of Dirac particles in graphene……..92

5.1 Modulation of the thermopower through electrostatic gate……92

5.2 Diverging behavior of the thermopower v.s. carrier density……...95

5.3 Temperature dependence of the thermopower……98

5.4 Thermopower and Nernst signal in the quantum Hall regime……..102

5.4.1 The effect of the Landau Level……...102

5.4.2 The Nernst peak at low carrier density……107

List of Figures

Fig 1.1 The edge states in quantum Hall (QH) effect and quantum spin Hall effect (QSH)…….....3

Fig 1.2 The calculated bulk and surface energy band structures of Bi_2Se_3 and Bi_2Te_3…….4

Fig 1.3 The spin-momentum locking for the surface states of 3D topological insulator……..5

Fig 1.4 The honeycomb lattice of graphene and the sp^2 hybridization…….7

Fig 1.5 The energy band structure of graphene…….8

Fig. 2.1 Crystal structure of Bi_2Se_3……...12

Fig 2.2 Bulk crystal of Bi_2Se_3……...13

Fig 2.3 The cloverleaf geometry of a Bi_2Se_3 flake for the vdP measurement…….13

Fig 2.4 The temperature dependence of the Ca doped Bi_2Se_3 as a function of doping level……..14

Fig 2.5 The optical microscope image of bare Bi_2Se_3 flakes on 300nm SiO_2…….16

Fig 2.6 The thickness of PMMA electron beam resist as a function of the coating speed……..17

Fig 2.7 The optical microscope image of Bi_2Se_3 flakes covered by 200nm thick PMMA…….18

Fig 2.8 Double confirm of the color contrast of the Bi_2Se_3 flakes by the AFM……..19

Fig 2.9 The ARPES data of the changing of the Fermi level in Bi_2Se_3 film in ultrahigh vacuum…..20

Fig 2.10 The strong degradation of Bi_2Se_3 sample under atmospheric exposure……..21

Fig 2.11 Schematic graph of the side view of the conventional Bi_2Se_3 device…….22

Fig 2.12 Nano-fabrication processes of the LOR protected Bi_2Se_3 device……...23

Fig 2.13 The LOR protected Bi_2Se_3 device……...23

Fig 2.14 Schematic graph of the penetration depth of the electron beam in the SEM……..24

Fig 2.15 Penetration depth of the electron beam in SEM with respect to the beam energy……..25

Fig 2.16 Nano-fabrication processes of the low energy electron beam lithography…….26

Fig 2.17 The optical image of the Bi_2Se_3 device made by low energy electron beam lithography…..27

Fig 2.18 Problems encountered in conventional Bi_2Se_3 devices……...28

Fig 2.19 The schematic graph of the device fabricating process for lithography-free method…….29

Fig 2.20 One typical nano-device made through lithograph free method…….30

Fig 2.21 The dimensions of the chip carrier for the device mounting……...31

Fig 2.22 The typical circuit diagram of the lock-in measurement of the device resistance……..32

Fig 2.23 The arbitrary geometry of the sample film for the vdP analysis…….33

Fig 2.24 Geometry of the sample film in the vdP measurement of the Hall resistance……34

Fig 3.1 Strong effect of lithography processing on the electron density increase in nano-device…..37

Fig 3.2 The quantum well states for n-type Bi_2Se_3……..38

Fig 3.3 Insulating behavior in the lithography-free device…….40

Fig 3.4 Large dose electron beam irradiation for a pristine lithography-free device……..42

Fig 3.5 The geometry of the back gating of a conventional Bi_2Se_3 device…….43

Fig 3.6 The gate tuning of the carrier density in a conventional Bi_2Se_3 device……..44

Fig 3.7 The advantage of the p-type Bi_2Se_3 device…….45

Fig 3.8 Device geometry for the electron beam irradiation…….46

Fig 3.9 Electron beam irradiation on the temperature dependence of the device resistance……...47

Fig 3.10 The fitting with the thermal activation model…….49

Fig 3.11 Electron beam irradiation on the gate dependence of the device resistance……...52

Fig 3.12 Enhanced field effect mobility in insulating device……54

Fig 3.13 Demonstration of the reversibility of electron beam irradiation……..56

Fig 3.14 The magnetoresistance at different gate voltages……...58

Fig 3.15 The 2D plot of calculated MR ratio vs. magnetic field and gate voltage……58

Fig 3.16 The Gate voltage tuning of the low-field MR feature……60

Fig 3.17 The 8 points moving average of the MR data……61

Fig 3.18 Magnetoresistance data and a smooth fourth-order polynomial fit……62

Fig 3.19 The SdH oscillations after the background removal……...63

Fig 3.20 The shift of the oscillation features at different gate voltages……64

Fig 3.21 A plot of the filling factor ν v.s. 1/B for three different gate voltages……65

Fig 4.1 The schematic graph of the Seebeck effect in a p-type sample……..68

Fig 4.2 The standard geometry for the measurement of the thermo-voltage……..68

Fig 4.3 The geometry for the measurement of the Peltier effect……69

Fig 4.4 The schematic graph for the Nernst effect……..71

Fig 4.5 The setup for the low temperature measurement of the thermopower……73

Fig 4.6 The device setup for the thermopower measurement of individual carbon nanotube…….74

Fig 4.7 The geometry of the device for the measurement of thermopower in graphene…….75

Fig 4.8 The thermal conductance of graphene and SiO_2 supporting layer……..76

Fig 4.9 The circuit diagraph of the heat flow in graphene device……...77

Fig 4.10 The optical image of our thermopower device for Bi_xTe_y nanoribbon……...78

Fig 4.11 The low temperature setup for thermopower measurement……80

Fig 4.12 The processes of mounting the low temperature thermopower setup……81

Fig 4.13 The thermo-voltage signal response upon changing of the thermopower……..83

Fig 4.14 The averaging sequences in the measurement of thermo-voltage……...84

Fig 4.15 The temperature dependence of the metal thermometer wire……85

Fig 4.16 The method for extracting the Seebeck coefficient of graphene……86

Fig 4.17 The simulated heater voltage and heater power in AC measurement……88

Fig 4.18 The AC measurement of the thermo-voltage……..89

Fig 4.19 The schematic graph in determine the temperature gradient near the Nernst leads……90

Fig 5.1 The gate tuning of graphene conductivity and Hall resistance……...93

Fig 5.2 Gate voltage tuning of the carrier density……...94

Fig 5.3 Gate voltage tuning of the thermopower……95

Fig 5.4 Diverging behavior of the Seebeck coefficient v.s. carrier density……97

Fig 5.5 V_g-dependence and temperature dependence of longitudinal Seebeck coefficient S_{xx}……99

Fig 5.6 The temperature and gate dependence of the thermopower in Device #19……..101

Fig 5.7 The two terminal resistance of the graphene device in quantum Hall regime……..102

Fig 5.8 The quantized Hall conductivity $\sigma_{xy} \sim 1/\rho_{yx}$ for Device #19…….…...…….103

Fig 5.9 The conductance and Seebeck coefficient in the quantum Hall regime……105

Fig 5.10 2D density plot of the S_{xx} and S_{xy} v.s. magnetic field and gate voltage for Device #19…...106

Fig 5.11 Field dependence of the Nernst signal……..108

List of Table

Table 3.1 Electron dose and electron energy vs. resulting chemical potential position.....….....50

Chapter 1 Introductions to topological insulators and graphene

The discovery and study of the novel materials or novel state of materials have been the central focus of condensed matter physics. The researches on these novel materials have not only deepened people's understanding in fundamental physics of matter but also brought the advances in technologies, which propel the advances of our world. For example, the discoveries of the quantum Hall state and superconducting state had demonstrated people with dramatically exotic properties of matter, among which quantum mechanics plays an important role even on the macroscopic scale. Furthermore, in the application of microelectronics, faster and smaller personal computers, energy efficient electronic devices and orders of magnitude increase in the capacity of information storage are all products of the research of materials science.

Graphene and topological insulators are two novel types of materials discovered between 2004 and 2006.[1-6] They possess novel properties, which originates from their unique crystal structures and symmetries and have attracted the interest of many researchers since then. Both of them carry massless Dirac fermions that have to be described by the relativistic Dirac equation, which results in electrical transport properties completely different from that in conventional semiconductors where Schrodinger equation is applied.[7,8] Furthermore, different from graphene, the Dirac fermions of a topological insulator exist only on its boundary and are protected by the time reversal symmetry while its interior is insulating. The most interesting part of a topological insulator is the edge state or boundary state. It belongs to a new class of matter and has its properties only determined by the topology of the material.[8,9] With this type of edge states, the high-mobility dissipationless electrical transport can be achieved and is robust to impurity scattering.[7] The similar state exists in the quantum Hall effect, but its

applications are restricted due to the requirement of a strong magnetic field. However, the topological insulator state exists without any external magnetic field and is time reversal invariant, which makes it a superior material for both fundamental researches and actual applications.

1.1 Topological insulator

The quantum Hall effect, discovered in 1980, reveals a new state of matter where in two-dimensions the conduction of a current is only carried by the one-dimensional channels located at the edge of that material, while the inner bulk material behaves insulating. Each channel contributes a conductance of exactly e^2/h (***h*** is the Planck constant) and total conductance of the material is determined by the total number of the edge channels.[10] Furthermore, the flow of electrons is only allowed in single direction at each edge while the opposite flow of the electrons is located in the opposite edges (Fig 1.1 (a)). This type of channel separation naturally prevents the backscattering of the electrons during their transport and results in very high mobility. However, the prerequisite of a quantum Hall state is the presence of a large external magnetic field, which cannot be simply achieved in electronics especially in nano-electronic.

In 2005 and 2006, theorists predicted the existence of the quantum spin Hall (QSH) state with the time reversal symmetry maintained due to its intrinsic spin-orbit coupling.[1,3] It first demonstrates that the quantum Hall state does exist in a time reversal invariant form and does not require an external magnetic field. As demonstrated in Fig 1.1 (b), at each sample edge, the channels with opposite current flow consist of electrons with opposite spin directions and the spin of the electrons is directly locked to its momentum, thus maintains its time reversal symmetry. At the one dimensional edge of the quantum spin Hall state, the electrons can only move forward or backward. Due to the time reversal symmetry,

if the conducting electron is scattered by a non-magnetic impurity, there are two time reversal symmetric paths for the scattering. However because the electron spin is locked to its momentum, the two paths carry opposite directions of spin. Hence, they exactly cancel each other and will result in a restriction of backscattering.[9] As a result of this, the edge state of a topological insulator is immune of non-magnetic impurity scattering and possesses strong potential for its applications.

(a) (b)

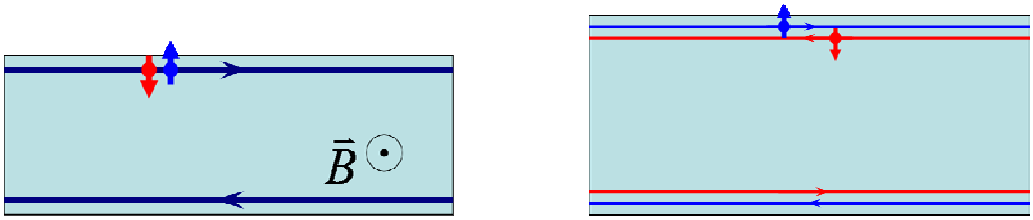

Fig 1.1 (a) The edge states in the quantum Hall (QH) effect. A magnetic field is present and time reversal symmetry is broken. (b) The edge states in the quantum spin Hall effect (QSH). Time reversal symmetry is preserved

In 2007, experimentalists first demonstrated the quantum spin Hall insulator state in HgTe quantum well structure.[11] They found an edge conductance of $2e^2/h$ (indicating two edge channels) independent of the geometry of the sample as shown in Fig 1.1, as well as a dramatic destruction of the edge conductance upon applying an external magnetic field. Further theoretical work in 2008 generalized the theory of the quantum spin Hall insulator such as HgTe by the topological filed theory and defined a new class of material called topological insulator.[8]

Besides the two-dimensional (2D) topological insulator HgTe, three-dimensional (3D) topological insulator materials are also predicted to exist.[12,13] Fig 1.2 demonstrates the calculated band structure of

3D topological insulator materials Bi_2Se_3 and Bi_2Te_3. Both of them have a surface band with a linear dispersion in the gap of the bulk energy band structure and a single Dirac cone.[13] The single Dirac cone consists of one Kramer's pair, which is protected by time reversal symmetry and is crucial for the robustness of the surface states. Furthermore, for intrinsic Bi_2Se_3 crystal, the Fermi level is situated right across the Dirac cone in the gap of the bulk energy band (Fig 1.2), which serves a good candidate for the study of transport properties of topological insulators.

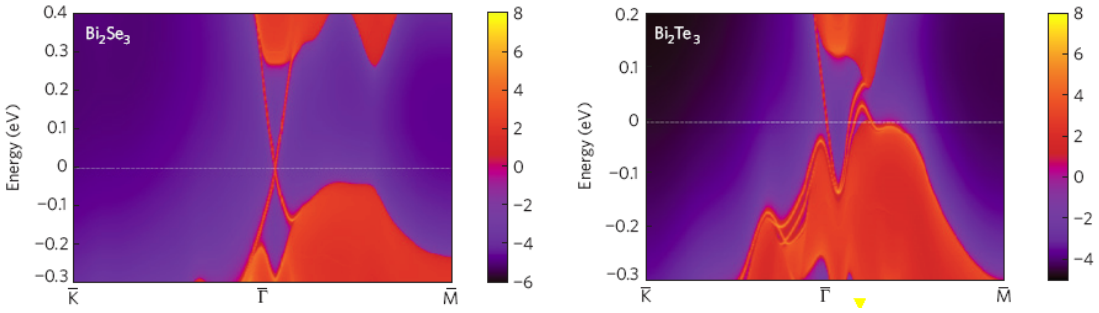

Fig 1.2 The calculated bulk and surface energy band structures of Bi_2Se_3 and Bi_2Te_3. The red area denotes the conduction band and valence band of the bulk material. The blue region is the band gap. The two crossed red lines indicate the topological surface states, which are situated inside the gap of the bulk energy band. The color scales on the right of the graphs denote the local density of states. (*Zhang, H. J. Nat Phys* ***5****, 438-442*)

Similar to HgTe material, electrons on the surface Dirac cone of Bi_2Se_3 also have their momentum locked to their spin. The momentum of surface electrons is a two-dimensional vector, thus the spin of the electrons form a helical structure as demonstrated in Fig 1.3(b). When the surface electron is scattered by non-magnetic impurities, similar backscattering restriction applies here. Because the momentum can take any value within the two-dimensional plane, there are possibilities that the

electrons are scattered side way (Fig 1.3(a)). However, the overall backscattering is still suppressed, which will result in a high mobility electrical transport.

(a) (b)

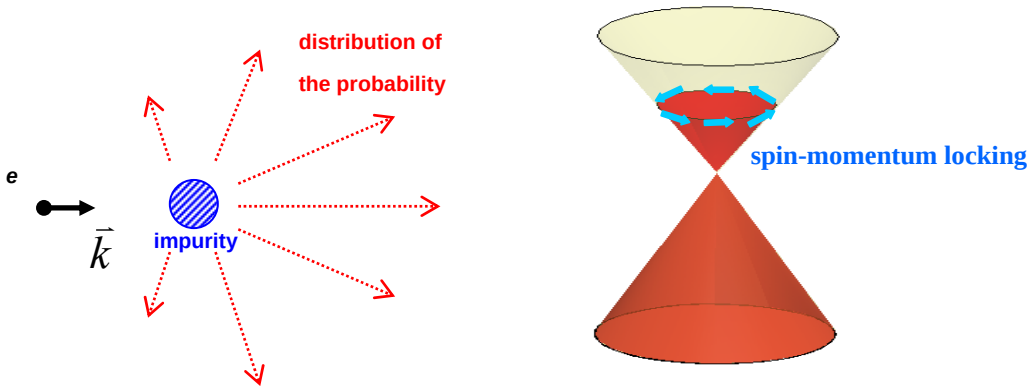

Fig 1.3 (a) The suppression of backscattering for the surface states of a 3D topological insulator. The red dotted line indicates the probabilities at each direction after the electrons are scattered. (b) The Dirac cone structure of the surface states of 3D TI with spin-momentum locking.

Up to now, 3D topological insulator materials have been confirmed by many surface sensitive experiments, for example ARPES (Angle Resolved Photoemission Spectroscopy) and STM (Scanning Tunneling Microscopy).[14-17] The suppressed backscattering on the surface of a 3D topological insulator has also been confirmed by STM studies.[16,17] However, the transport study of topological insulator materials has largely been hindered by the high bulk carrier density that short-circuits the non-trivial surface channel. Much attention has been focused on reducing the unwanted bulk charge carriers in order to utilize the extraordinary properties of topological surface states in novel electronics.[18-25]

In this thesis, we demonstrate a systematic study and control of the bulk carrier density in Bi_2Se_3 thin flake devices. By tuning the position of the chemical potential in p-type Ca-doped Bi_2Se_3 thin flake devices we achieved an insulating bulk state and a dramatic increase of the field effect mobility. The magneto transport studies also reveal interesting behaviors of the devices. These experiments become possible only after the development of a set of proper lithography techniques that prevent the damage to the Bi_2Se_3 devices due to the instability of the Se atoms inside the material. The details about these experiments will be discussed in Chapter 2 and Chapter3.

1.2 Graphene

Although the unusual band structure of graphene had been predicted as early as in 1946,[26] the actual graphene material was first isolated only after 2004.[4,5] Graphene can be easily obtained by exfoliating bulk graphite materials with scotch tape onto SiO_2 substrates in the form of graphene flakes with a size of tens of microns. The graphene flakes are then identified and fabricated into electronic devices through the methods of modern nano-technologies.

The unique properties of graphene come from its unique lattice structures.[7] As demonstrated in Fig 1.4(a), the graphene material consists of a plane of carbon atoms packed in a honeycomb lattice. One s-orbital and two p-orbitals of the carbon atom undergo sp^2 hybridization, which form three identical orbitals sitting in the plane of the graphene. The other p_z-orbital is perpendicular to the graphene plane (Fig 1.4(b)). The three in-plane orbitals form the σ bonds, which results in the honeycomb lattice structure. The perpendicular p_z-orbital forms π bond and contributes to the electronic structure of graphene.

Each unit cell of graphene has two distinctly different atomic sites we label as atom “A” and “B”. By solving the tight-binding model, the energy band of graphene can be written as:

$$E_{\pm}(\vec{k}) = \pm t\sqrt{3 + f(\vec{k})} - t'f(\vec{k}) \qquad \text{(Eq 1.1)}$$

with $$f(\vec{k}) = 2\cos(\sqrt{3}k_y a) + 4\cos(\frac{\sqrt{3}}{2}k_y a)\cos(\frac{\sqrt{3}}{2}k_x a)\,.$$

The “+” and “-” sign here denotes the electron and hole energy bands. The quantity “*a*” is the lattice constant of graphene. *t* and *t’* denote the nearest neighbor hopping and the next nearest neighbor hopping energies. If only the nearest neighbor hopping is considered, the energy bands of electron and hole are symmetric. Fig 1.5 demonstrates the energy band of graphene. We can clearly see that the energy band with linear dispersion appears at six Brillouin zone corners, which can be expressed as $E(\vec{k}) = \hbar v_F |\vec{k}|$ with the Fermi velocity $v_F \sim 1\times 10^6$ m/s.[7]

(a) (b)

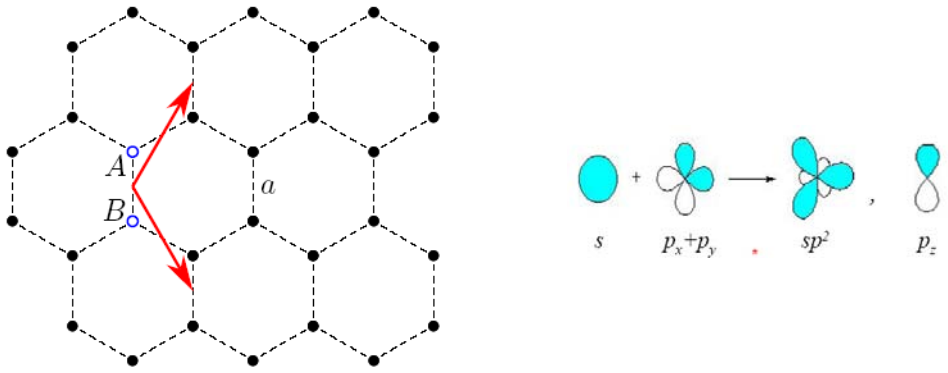

Fig 1.4 (a) The honeycomb lattice of graphene. Each unit cell of graphene consists of two different atomic sites “A” and “B”. The red vectors are the primitive vector of the unit cell. (b) The sp^2 hybridization of electron orbitals of carbon in graphene.

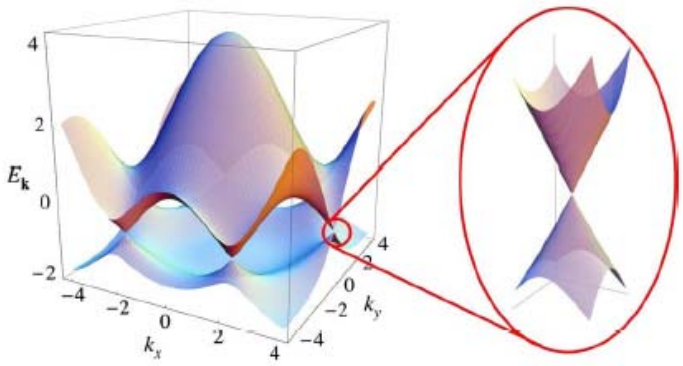

Fig 1.5 The energy band structure of graphene. In the Brillouin zone, there are two energy bands corresponding to π and π* orbitals. The linear dispersion is demonstrated at the Brillouin zone conner. (*Castro Neto et al.,Rev Mod Phys* ***81****, 109-162*)

If we consider only the nearest neighbor hopping ($t' = 0$ in Eq 1.1), the Hamiltonian of graphene can be written exactly in the form as in the relativistic Dirac equation with zero effective mass and electron-hole symmetry.[7] This gives rise to many interesting properties, for example the half integer quantum Hall effect and the Klein tunneling etc.[5,6,27,28] The relativistic nature of graphene ensures it to carry electrical transport at very high mobility, making it a good candidate for fast electronics. While the unusual band structure of graphene gives rise to many interesting phenomena in electrical transport properties that have been under extensive experimental investigations. In solids, both charge and heat flows are simultaneously generated when an electrochemical potential or a temperature gradient is present, leading to additional effects. Fundamentally related to the electrical conductivity, other transport coefficients such as thermal conductivity and thermoelectric coefficients are also determined by the band structure and scattering mechanisms. In Chapter 4 and Chapter 5 of this thesis, we will demonstrate our thermoelectric study of the Dirac fermions in graphene, especially under the quantum

Hall regime, where the anomalous properties of the thermoelectric transport of the Dirac fermions are demonstrated.

Chapter 2 Fabrication techniques of Bi_2Se_3 devices and experimental setup

A major issue of the application of topological insulator materials in electrical transport is the control of the Fermi level.[18-25,29] The electron or hole carriers near the Fermi level determine the electrical transport properties of a material. In order to utilize the novel properties of topological surface carriers, the Fermi level has to be controlled to only cross the surface energy band, i.e. to stay inside the gap of the energy band of the bulk material. Among all the topological insulator materials, Bi_2Se_3 hosts the largest band gap (300 meV) and a single surface Dirac cone inside it.[13] Nano-scale Bi_2Se_3 material, such as thin flakes, also has an enhanced surface to volume ratio compared to its bulk counterpart, which results in a lower bulk carrier density. The 2D carrier density of a Bi_2Se_3 thin flake is scaled as 1/thickness. Hence, methods of thinning down the bulk Bi_2Se_3 materials are performed and will be demonstrated in this chapter. Furthermore, the decrease of the bulk carrier density in the nano-device also enables the tuning of both the surface and the bulk Fermi level with an electrostatic gate, which provides the advantage of electronically controlled transport of the topological surface states.[24,25,30,31]

2.1 Bi_2Se_3 thin flake preparation

2.1.1 Crystal structure of Bi_2Se_3

Bi_2Se_3 is a binary compound with rhombohedral structure. Fig 2.1 shows the unit cell of the crystal. Eight Se atoms forms a structure that resembles a cube stretched along its diagonal direction (111), while another two Se atoms and two Bi atoms are evenly distributed along that direction. If we look from the (111) direction, the crystal structure of Bi_2Se_3 can be set equivalent to a hexagonal lattice. The Se layer and Bi layer are stacked in sequence onto the hexagon sites. From Fig 2.1, we can see that

the stacking sequence is repeated by the block Se-Bi-Se-Bi-Se so called a quintuple layer. The adjacent quintuple layers have two Se atoms as neighbors, which are bonded by Van der Waals force. Inside the Se-Bi-Se-Bi-Se block, the bonding is covalent. The strength of the Van der Waals force is much weaker than the covalence bonding force. Hence, Bi_2Se_3 is much easier to be cleaved between the quintuple layers and form a thin piece by repeated cleaving. If proper techniques are taken, it can even be thinned down to one quintuple layer, which is about 1nm in its thickness.[30,31] With this unique structure, peeling-off process is superior to form thin flake Bi_2Se_3 crystal in order to reduce the bulk to surface carrier ratio and obtain electrostatic gate control.

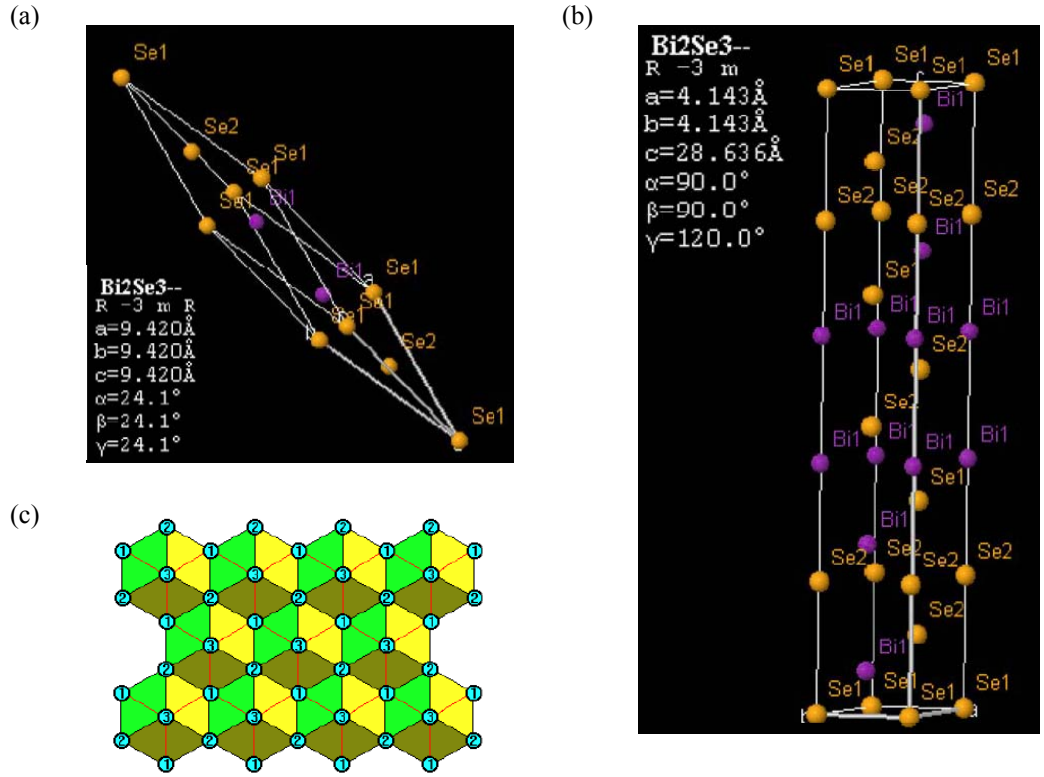

Fig. 2.1 Crystal structure of Bi_2Se_3. (a) The unit cell of Bi_2Se_3. (b) The crystal structure along the c-axis direction. The clear Se-Bi-Se-Bi-Se quintuple layer can be seen. (c) The packing sequence from the top view in (b).

2.1.2 Bi2Se3 crystal and thin flake preparation

Single crystal Bi_2Se_3 is synthesized by the solid-state reaction method. A multistep heating process is performed to form the final crystal as described in the paper *Z. Wang Appl. Phys. Lett. (2010)* [32]. The resulting compound can be easily cleaved from the crystal chunk of as shown in Fig 2.2. The thickness of the cleaved piece is in the range of 10 to 100 μm. The resistivity and Hall coefficient of the cleaved piece are measured via Van der Pauw method. Fig 2.3 shows typical measurement

geometry. Thin gold wires are attached to the sample with indium dot. The clover-leaf shape of the thin piece is designed to minimize the irregularity of the shape of the indium dot contact to the transport measurements. The measurements demonstrate that the pure Bi_2Se_3 crystal piece is always metallic with n-doping. However, theoretically, all the conduction bands of a Bi_2Se_3 crystal should be empty and all the valence bands should be filled up.[13] Hence, the Fermi level should stay exactly in the band gap. The n-doping observed from the experiment is not intrinsic. Previous researches attributed the n-doping to Se vacancies.[29,33,34] The negatively charged Se vacancy defects pin the Fermi level of the material inside the bulk conduction band.

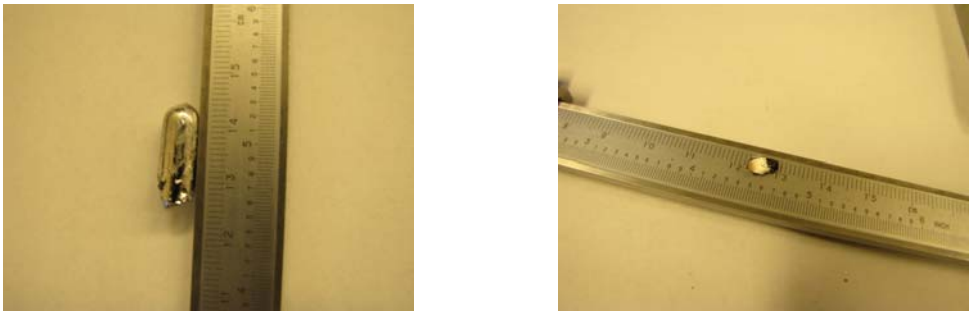

Fig 2.2 Bulk crystal of Bi_2Se_3. The method of preparing the crystal is discussed in the paper *Z. Wang Appl. Phys. Lett. (2010)* [32]

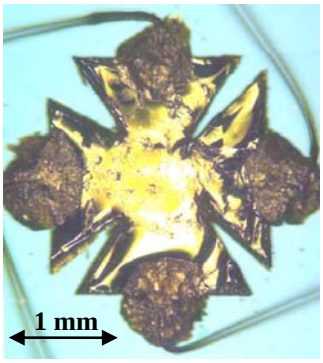

Fig 2.3 The cloverleaf geometry of a Bi_2Se_3 flake for the vdP measurement.

To push the Fermi level down into the band gap, Ca-doping is utilized. The purpose of the Ca-doping is to use Ca atoms to substitute the Bi atoms, which creates holes. It forms a compound with the form of $Ca_xBi_{2-x}Se_3$.[29] Systematically doping of Ca effectively brings the Fermi level into the band gap resulting in an insulating material.[32]. Fig 2.4 demonstrates the typical insulating behavior of the temperature dependence of the resistance as Ca atoms are doped into the material.

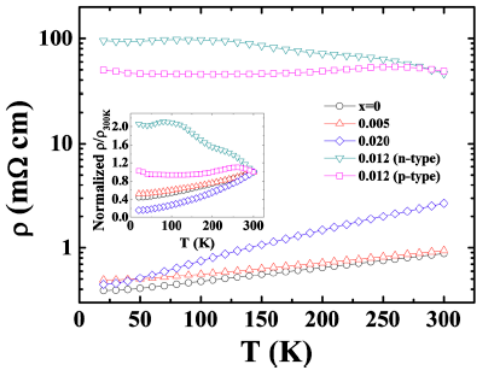

Fig 2.4 The temperature dependence of the Ca doped Bi_2Se_3 as a function of doping level. This data is from the paper: *Z. Wang Appl. Phys. Lett. (2010)* [32]

Further thinning down is performed on the compensated $Ca_xBi_{2-x}Se_3$ compound. In our material, the compensated doping condition happens at 1.2% Ca doping level, where the carrier density changes sign. The layered structure of Bi_2Se_3 as introduced in section 2.1.1 is very similar to the layered structure of graphite. The binding force between the adjacent quintuple layers is Van der Waals force. The process of peeling-off graphene from graphite is already well known and has been widely used.[4] Similar exfoliation procedures are taken to further thin down the cleaved $Ca_xBi_{2-x}Se_3$ piece. The $Ca_xBi_{2-x}Se_3$ piece is first sandwiched between two scotch tapes. Then the two scotch tapes are detached to exfoliate the crystal into thinner pieces. This process is repeated until very faint region of the crystal

is left on the tape. The tape is then attached onto SiO_2 wafer surface and pressed with tweezers. After about 10~20 mins, the tape is carefully detached from the SiO2 wafer. The scotch tape should be detached starting from one side of the wafer and slowly to the other side. In the end, the thin flakes of $Ca_xBi_{2-x}Se_3$ compound with the size of ~10 μm are left on top of the SiO_2 wafer and can be located through an optical microscope. The condition of the wafer surface is important to whether thin flakes can be exfoliated. The detailed recipe of the wafer cleaning that we use is listed below:

(1.) The Si/SiO_2 wafer is soaked inside acetone at temperature 60 degree C for about half an hour. This process is taken to remove the organic layer covered on top of SiO_2.

(2.) The wafer is then rinsed with acetone (20 sec), IPA (20 sec) and DI water (20 sec). Clean nitrogen gas is used to dry the wafer.

(3.) The wafer is then soaked in side 29% ~ 36% H_2O_2 solutions for about 20 min and rinsed with DI water in the end. The oxidation provided by H_2O_2 further cleans the wafer surface. The sticking between the SiO_2 and the Bi_2Se_3 flake are proven to be better after this process. RIE cleaning can also be taken; however, it may induce extra charges and damages to the wafer surface.

Another type of tape is also used to minimize the tape residue on wafer surface. The order information is Clear Low Tack Roll, part# 19161 from Semiconductor Equipment Corporation. This recipe is first invented by Xinfei Liu in our group and is widely used in our group now. The same procedure can also be utilized to exfoliate Bi_2Se_3 on top of $SrTiO_3$ (STO) insulating surface.

2.1.3 Thin flake location and identification

Thin flakes of Bi_2Se_3 are located under an optical microscope. Similar to the identification of graphene flakes, the color contrast examine method is used here to tell the thicknesses. However, different from graphene, under the microscope it is hard to tell the color contrast of bare Bi_2Se_3 flakes with different thicknesses on top of SiO_2 wafer as shown in Fig 2.5.

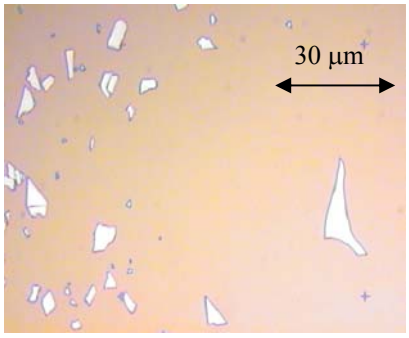

Fig 2.5 The optical microscope image of bare Bi_2Se_3 flakes on 300nm SiO_2. The optical color contrast is low and is hard to tell the difference between thick flakes and thin flakes.

In order to enhance the color contrast, after exfoliation of the thin flakes, we coat a layer of PMMA on top of the wafer surface without baking. PMMA (polymethyl methacrylate) is a polymeric material commonly used as the masking material in electron beam lithography processes. In our method, the wafer is coated with 950 PMMA A-4 under 4000 rpm for 45 sec, which will result in a polymer thickness of around 200 nm (Fig 2.6).

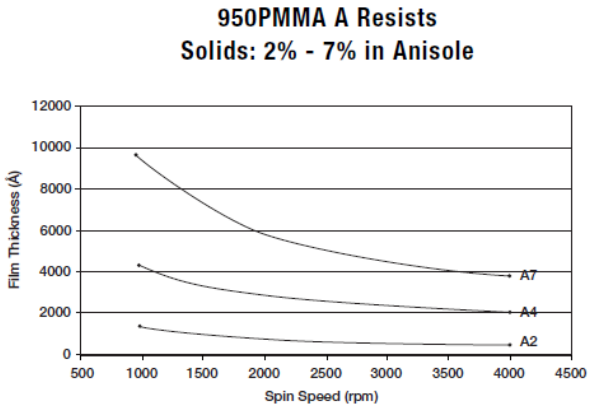

Fig 2.6 The thickness of PMMA electron beam resist as a function of the coating speed. (from MICRO CHEM PMMA data sheet)

After the PMMA coating, the wafer surface is then examined under the microscope. As a result of the coating, the color contrast of the flakes becomes sharper. As shown in Fig 2.7, the flake color becomes red. The thinner the flake, the darker its color looks. Over the view of the microscope, we can see clearly a variation of the color on different flakes. The reason of the color contrast can be simply explained in the following way. As show in Fig 2.7(b), the light source of the microscope shines light on to the surface of the wafer. Because the surface is covered with PMMA, the light needs to penetrate through it in order to be reflected by the thin flake surface. The thickness of the PMMA layer is 200 nm comparable to the typical thickness of the thin flakes, which is between 10 to 100 nm (Fig 2.8). The thinner the flake, the longer the light needs to travel inside the PMMA in order to be reflected back to the object lens of the microscope, hence the lower intensity of the light. This method provides a convenient way in telling the thickness differences of the thin Bi_2Se_3 flakes.

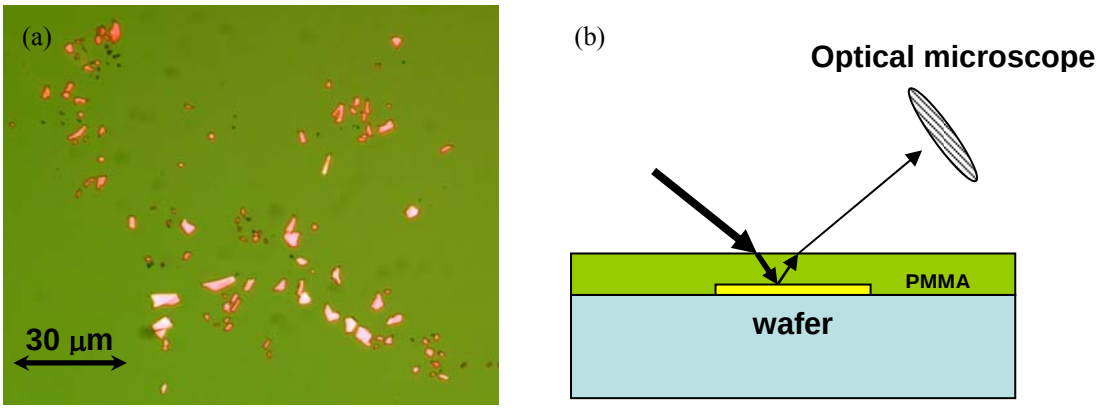

Fig 2.7 (a) The optical microscope image of Bi_2Se_3 flakes covered by 200 nm thick PMMA on 300 nm SiO_2. The color contrast between thick and thin flakes is more obvious. (b) The schematic demonstration of the light absorbed through the PMMA layer.

The color contrast is then confirmed by the atomic force microscopy (AFM) measurements. Fig 2.8 shows an AFM scan over a region of the flakes in the optical image of Fig 2.7. The upper-left image is the optical image. Within the boxed region, thicknesses of two flakes I and II are measured with AFM. Their thicknesses are ~ 30 nm and ~ 20 nm. The dark flake has a lower thickness. With this technique examined by AFM measurements, we are able to quickly select flakes of different thicknesses before fabricating devices from them. It largely shortens the processing time of the nano-fabrication process.

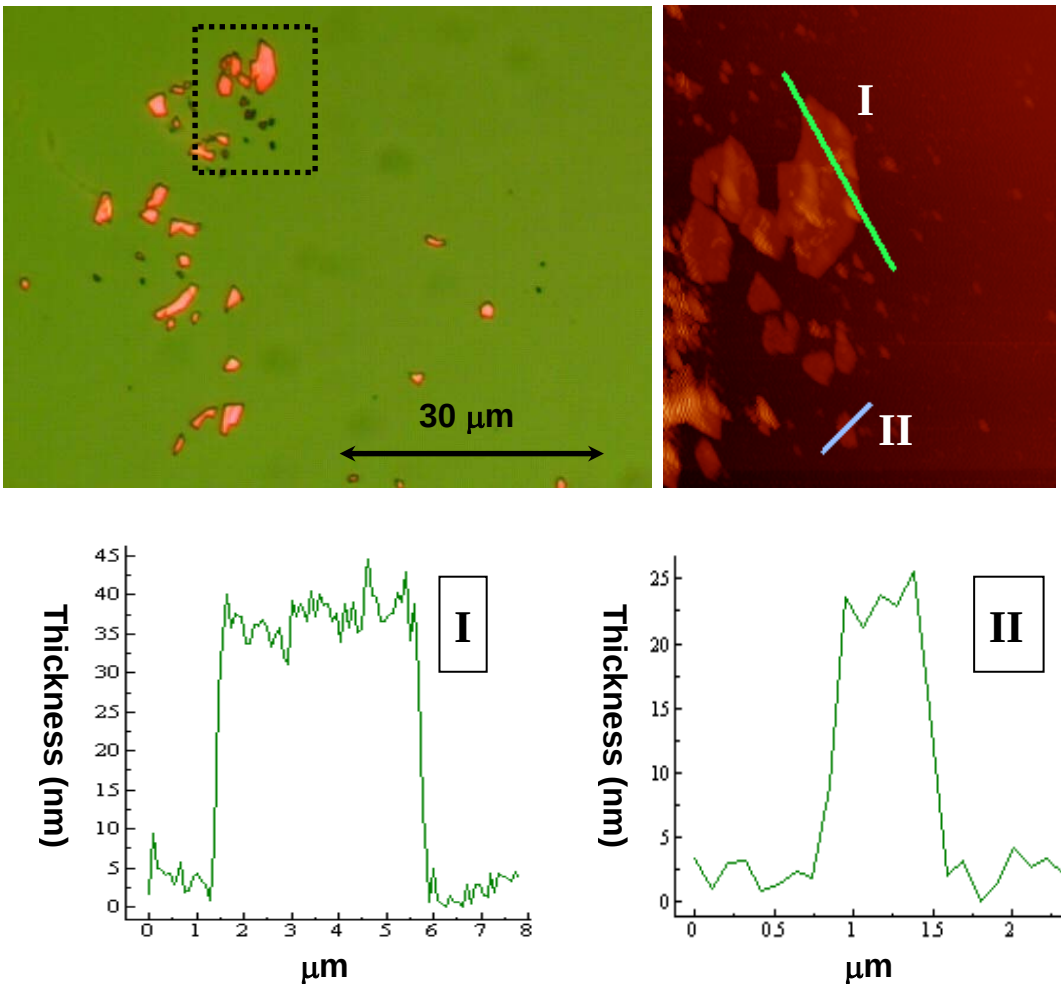

Fig 2.8 The color contrast of the Bi_2Se_3 flakes is confirmed by the AFM measurements. The upper-left is the optical image and the right top is the AFM image of the same region of flakes.

2.2 Device fabrications of Bi_2Se_3 thin flake

In this section, three device fabrication techniques are introduced. The purpose is to minimize the damage to the Bi_2Se_3 thin flakes.

2.2.1 Strong degradation of Bi_2Se_3 material under ambient condition

With all the beautiful properties of Bi_2Se_3 predicted, however, in experiments people find that the surface of this material is unstable even in an ultra-high vacuum. ARPES measurements show that

upon cleavage of the Bi_2Se_3 crystal, the Fermi level is evolving with time. Fig 2.9 shows a typical ARPES measurement by *D. Hsieh et al.* from Princeton group in ultra-high vacuum.[35] Clearly we can see that 15 min after cleavage the Fermi level still stays inside the bulk energy band gap. However, it keeps rising until it reaches to the bottom of the conduction band after about 18 hours. The reason of this is attributed to the forming of the Se vacancies on the cleaved surface of the material, which shifts the Fermi level and results an n-doping to the material.

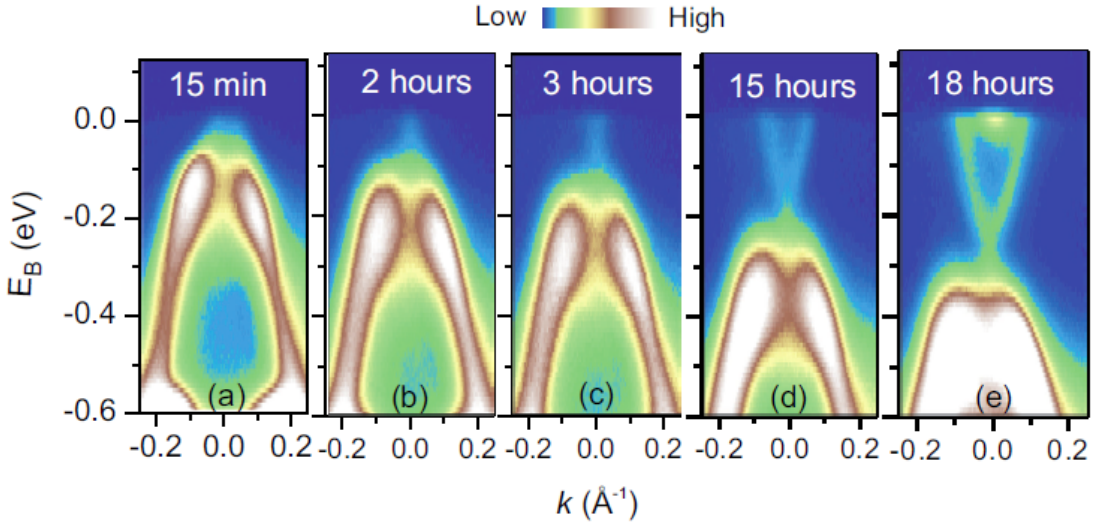

Fig 2.9 The ARPES data of the changing of the Fermi level in Bi_2Se_3 film in ultrahigh vacuum. This data is from the supplementary information in the paper *Hsieh, D. et al. Nature* ***460****, 1101-1159*.

The transport studies revealed the same effect. Fig 2.10 shows the systematic results of the environmental effects to the transport properties of Bi_2Se_3 by *J. G. Analytis et al.* from Stanford group.[20,21] In Fig 2.10(a), a short exposure (1~2 hours) of the material to atmospheric environment sharply removes the surface quantum oscillations features from the data of the original sample. In Fig 2.10(b), the sample is exposed under humid environment at 50 degree C for an extended time. From the

temperature dependence of the resistivity data, a clear decrease of the insulating behavior can be seen. The degradation becomes stronger as the exposure extends longer. All these evidences demonstrate that special care needs to be taken in order to protect the Bi_2Se_3 material during the transport studies.

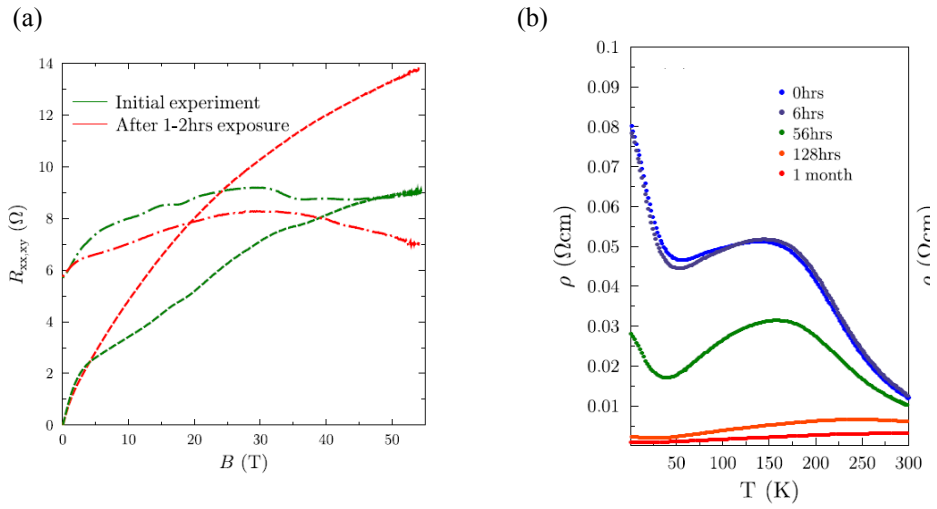

Fig 2.10 The strong degradation of Bi_2Se_3 sample under atmospheric exposure (a) and under moisture condition (b). This data is from the supplementary information in the paper *Analytis, J. G. et al. Nat Phys* ***6****, 960-964*.

2.2.2 LOR protected device fabrication process

The fabrication of Bi2Se3 thin flake devices can take the standard electron beam lithography process similar to graphene as mentioned in a lot of references.[23-25] I will not go through the detailed process of the standard lithography here. However, during that process, the flake is exposed to atmospheric environment whenever a lift-off is performed and the final device is also exposed to air during transport measurements (Fig 2.11).

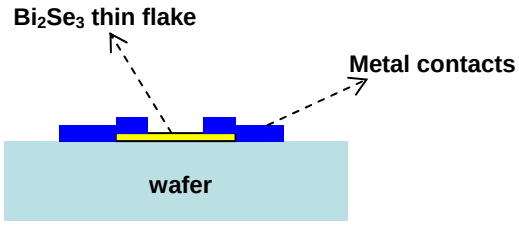

Fig 2.11 Schematic side view of a conventional Bi_2Se_3 device after nano-fabrication.

I demonstrate another special lithography process here (Fig 2.12), which always provides protection to the Bi_2Se_3 thin flake after it is exfoliated. A critical part is the proper utilization of the Lift-Off Resist (LOR). LOR resists are based on the PMGI (polymethylglutarimide) material. After the exfoliation of Bi2Se3 thin flake, the whole wafer is spin-coated with LOR and PMMA. Then the device pattern is written by the electron beam lithography (EBL). The energetic electron beam only changes the properties of the PMMA within the pattern region. After writing, the top PMMA pattern is dissolved in MIBK + IPA (1:3) solution for 65 sec. With the pattern of the PMMA as a mask, the device is soaked into MF-319 solution for 2~3 sec to dissolve the LOR. So the pattern is then transferred down to the LOR layer. A Ti/Au (10/120 nm) metal layer is then deposited on top of the wafer. It fills the pattern slot also. The PMMA dissolves in acetone, however, the LOR doesn't. In the lift-off step, acetone is used to remove the PMMA layer as well as the metal layer on top. In the end, the device is fabricated with a LOR layer covering the Bi_2Se_3 thin flake. Note that the Bi_2Se_3 thin flake is covered with LOR right after it is exfoliated. It provides a shield over the flake to protect it from the degradation to the atmospheric environment. In Fig 2.13, a typical optical microscope image of the device has been shown, which is fabricated with this method.

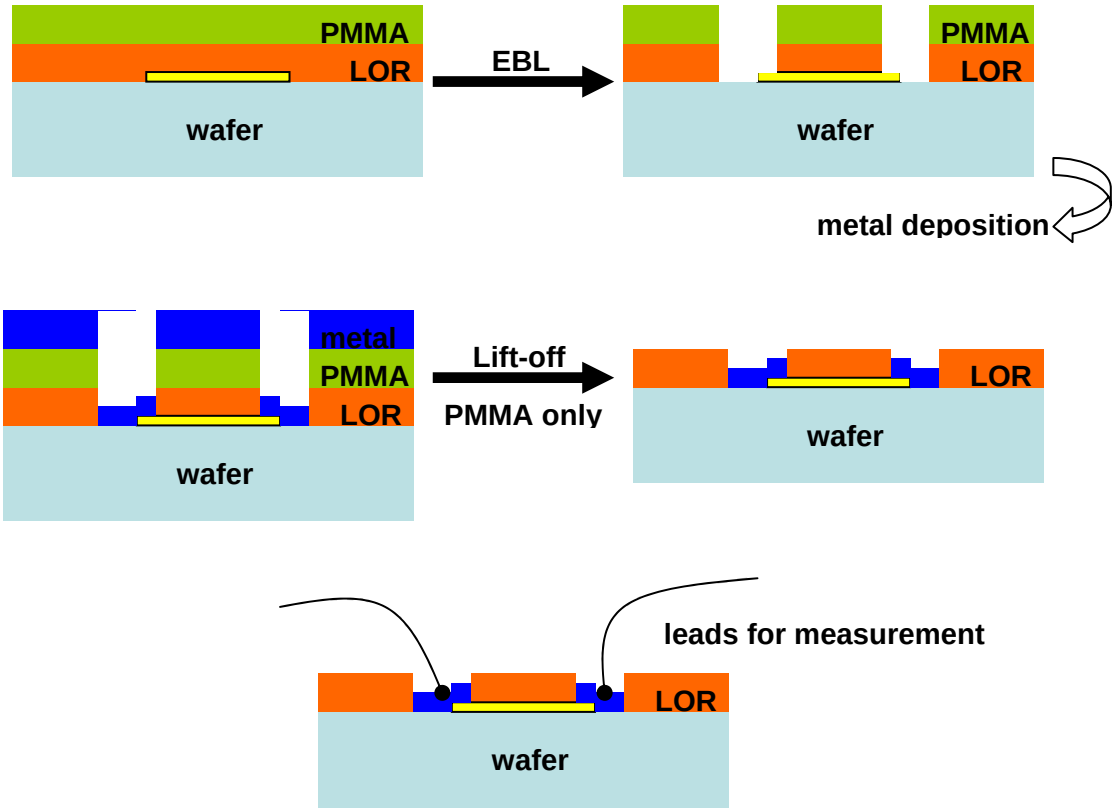

Fig 2.12 Demonstration of the nano-fabrication processes of the LOR protected Bi_2Se_3 device.

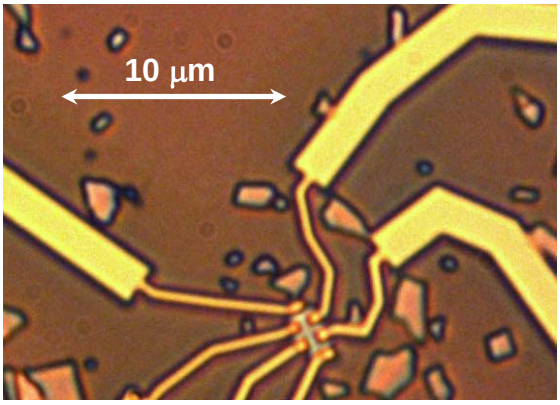

Fig 2.13 Optical image of one of the LOR protected Bi_2Se_3 device. The device is covered by a LOR resist and the image of the flake is not as clear as the one for bare Bi_2Se_3 device.

2.2.3 Low energy electron beam lithography

Although method 2.2.2 provides a convenient way to protect Bi_2Se_3 thin flakes from the atmosphere, it is not the only source of degradation to the flake. In our experiment, we also found that the electron beam irradiation also affects the device. High energy or large beam current electron beam irradiations strongly destroy the device mobility. The detailed discussion will be provided in chapter 3.

In conventional EBL writing process, the electron beam energy is in the range of 20 ~ 30 keV. The purpose of the electron beam is to locally irradiate a positive resist so that only the exposed region of the resist is washed away in the later dissolving process. However, the energetic electron beam has the ability to interact with the irradiated material. The higher the electron beam energy the larger the beam-specimen interaction will be. Fig 2.14 shows the qualitative dependence of the beam-specimen interaction volume v.s. beam energy.

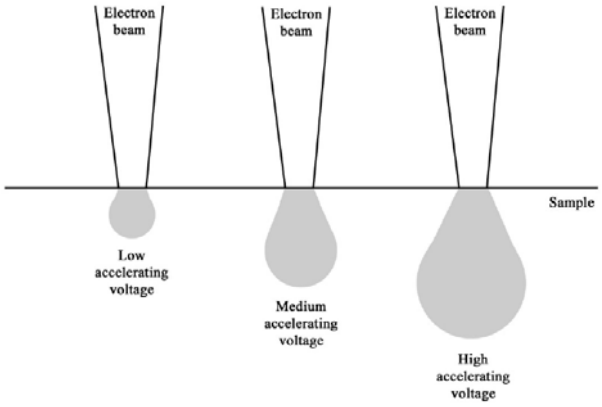

Fig 2.14 Schematic view of the penetration depth of the electron beam in the SEM with respect to the beam energy.

Furthermore, the electron beam with energy of 20 or 30keV can easily penetrate through the lithography resist and reach the Bi_2Se_3 thin flake underneath.[36] Fig 2.15 shows the theoretical

calculation of the penetration capability of electron beams with different energies through a 200 nm PMMA and a 300 nm PMMA. 5 keV is already enough to penetrate through 300 nm PMMA layer.

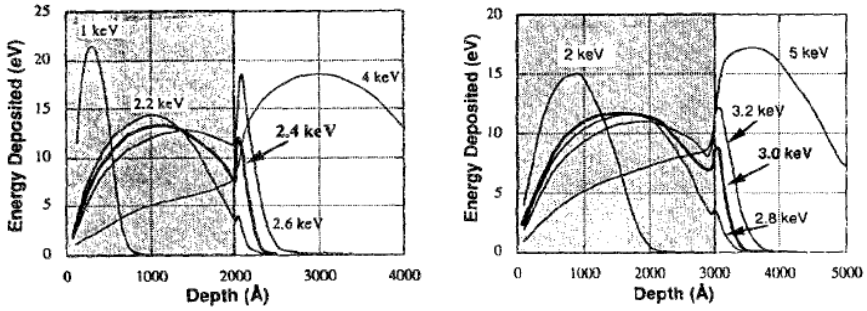

Fig 2.15 Calculation of the penetration depth of the electron beam in SEM with respect to the beam energy. This data is from the paper *Peterson, P. A. et. al., J Vac Sci Technol B (1992)*.[36]

I demonstrate here a special lithography technique in order to prevent the electron beam irradiation to the thin flake. This method uses bi-layer lithography resist LOR-3B + PMMA (thickness: 300 nm+200 nm). The electron beam energy used for writing is only 4 keV. The idea of this method is to control the electron beam to only interact with the top PMMA layer rather than penetrating through both LOR and PMMA layers. The LOR layer does not require electron beam exposure and the pattern can be transferred onto it with the top PMMA layer acting as a mask, which is similar to the process shown in Fig 2.12.

Fig 2.16 shows the comparison between conventional EBL and low energy EBL. The recipe is tested in the following way. Different electron beam energies (2keV, 3keV and 4keV) are used to write test patterns onto the LOR+PMMA bi-layer resist. After that, PMMA is developed to form a mask. Then MF-319 solution is used to etch the LOR through the mask. If the LOR can not be etched, it means that the PMMA is not fully penetrated by the electron beam. Then larger beam dosage is used to

test again. If sufficiently large beam dosage is used and it still can not penetrate through the PMMA, a higher acceleration voltage is used to repeat the test. In our recipe, we use a 4 keV electron beam with a 70 μC/cm^2 for the writing of thin lines (~ 0.8 to 2.0 μm) and 150 μC/cm^2 for the writing of thick lines (> 2.0 μm).

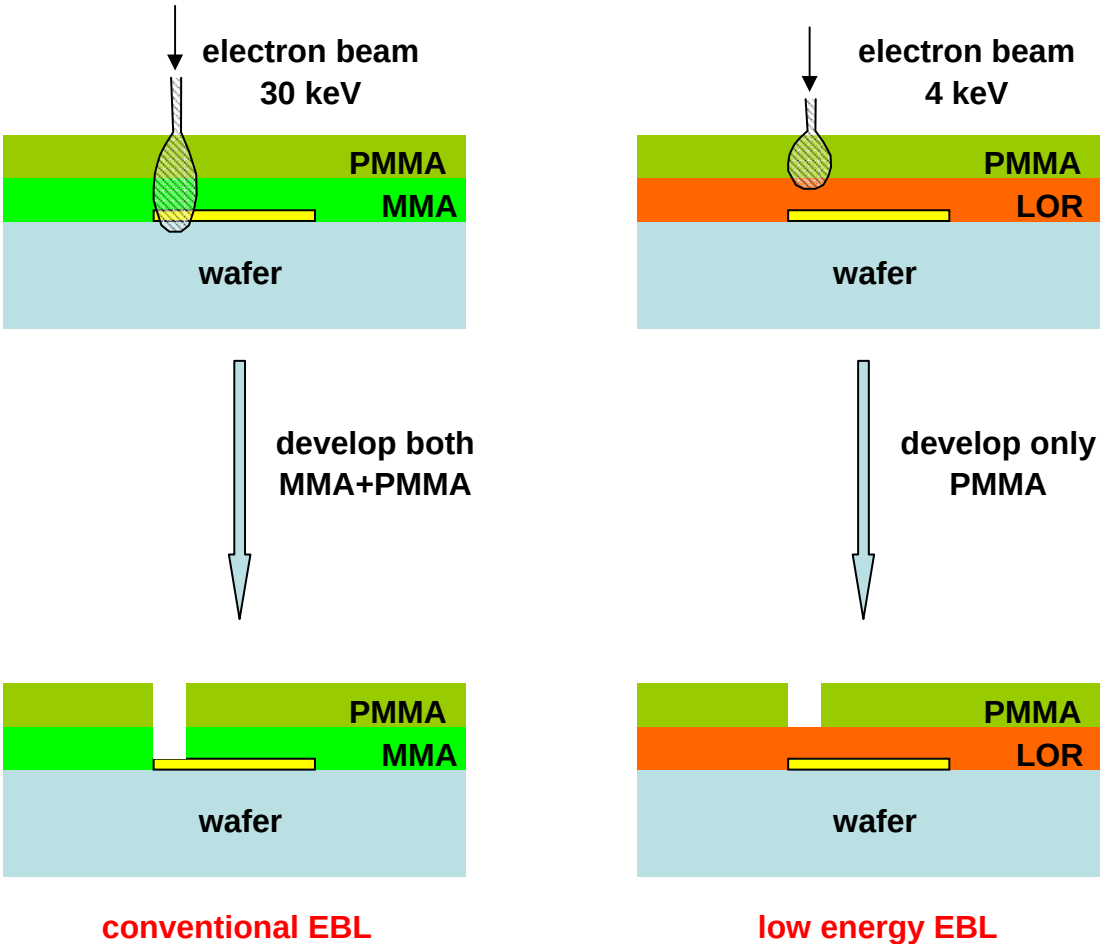

Fig 2.16 Demonstration of the nano-fabrication processes of the low energy electron beam lithography.

Fig 2.17 shows an optical image of a typical device fabricated using low energy electron beam lithography. The Bi_2Se_3 flake is also covered by LOR layer after the exfoliation as mentioned in section

2.2.2. With this method, we can protect the device both from the affect of atmospheric environment and from electron beam irradiation.

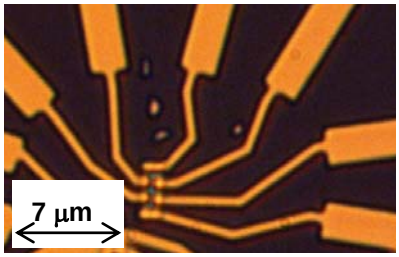

Fig 2.17 Optical image of the Bi_2Se_3 device made by low energy electron beam lithography. The Bi_2Se_3 flake is also covered by the LOR resist here.

2.2.4 Lithography free fabrication techniques

Although the two methods introduced in section 2.2.2 and 2.2.3 protect the Bi_2Se_3 thin flake to some extent, the resulting devices still behave strong n-type doping compared to its original bulk material. Very clear evidence is from temperature dependence of the resistivity. As it is shown in Fig 2.18, even though the thin flake is exfoliated from insulating bulk material, the nano-device still behaves metallic. The field effect mobility of these devices is also very small (around or less than 1000 cm^2/Vs).

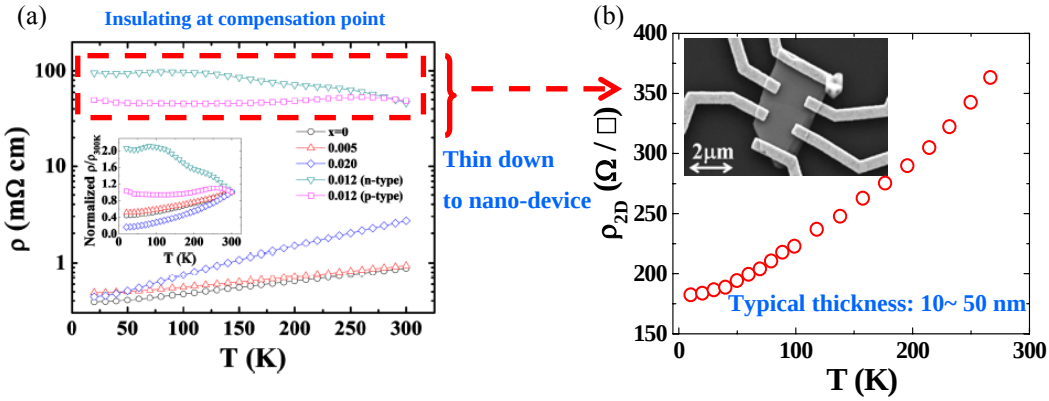

Fig 2.18 (a) Temperature dependence data of the bulk Bi2Se3 material the same as in Fig 2.4. (b) The temperature dependence of the device made from the compensated material as in (a), however, its shows a metallic behavior. A SEM image of one typical device is in the inset.

Some other sources must still exist that affect the Bi_2Se_3 device. Comparing the methods in section 2.2.2 and 2.2.3 with the conventional EBL processes, the common process that is still not improved is the spin coating and baking of the lithography resist. The lithography resist is one kind of solvent. After the spin coating, hotplate baking is used to remove the solvent. The baking temperature is as high as 170 °C. From the discussions in the second part of section 2.2.1, the degradation of the Bi_2Se_3 material becomes extremely strong under the warm humid environment.[20,21] Hence, an effective method is needed to overcome the damage from this process.

Here we introduce our lithography free fabrication method. As shown in Fig 2.19, the measurement electrodes are pre-patterned on a blank wafer. The Bi_2Se_3 thin flakes are then exfoliated onto the electrodes. The exfoliation is achieved with similar scotch tap method as mentioned in section 2.1.2. A rough alignment is performed under an optical microscope to aim the flake region on the tape toward the electrode region on the wafer. However, extra care needs to be taken to press the tape firmly

to the surface of the electrodes and to peel-off slowly in order to achieve good contact. The design of the electrodes is also important. First, it needs to provide basic measurement capabilities, for example, four-terminal resistance or van der Pauw measurements. Then, the pattern needs to be dense enough so that there is a higher chance for the randomly exfoliated Bi_2Se_3 thin flakes to sit on top of the electrodes.

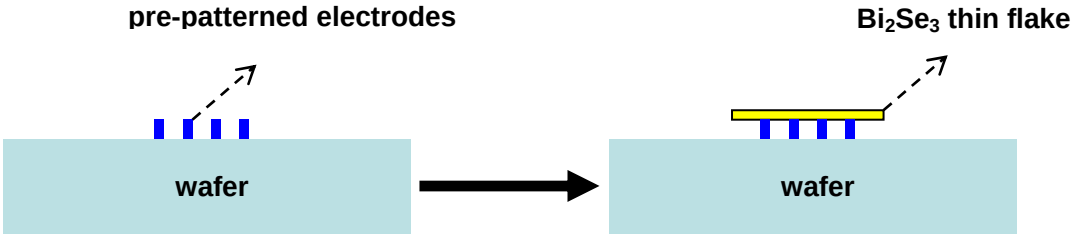

Fig 2.19 Schematic pictures of the lithography free device fabrication method.

Fig 2.20 shows one demonstration device for four terminal resistance measurements. The typical contact resistance is on the order of 1 kΩ. This type of device can be taken for transport measurement immediately after exfoliated and does not go through any lithography process that degrades its properties. Our transport measurements on this type of device show a preserved insulating behavior similar to its original bulk material, which indicates the minimized degradation. Detailed measurement results will be demonstrated in Chapter 3.

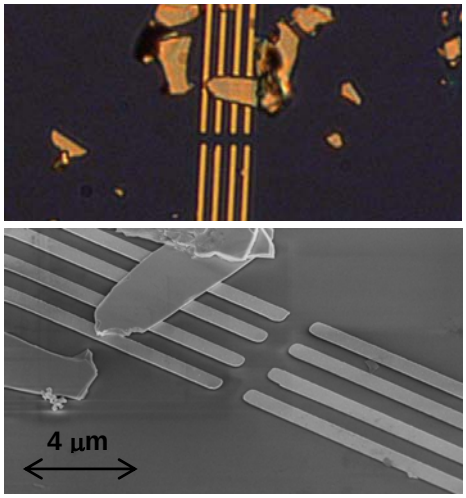

Fig 2.20 One typical nano-device made through the lithography-free method. The top image is an optical image and the bottom image is a SEM image.

2.3 Experimental setup

2.3.1 Device mounting

After device fabrication, the device-containing chip is directly held onto a chip carrier with silver paste. The 20-pin chip carrier is purchased from SPECTRUM SEMICONDUCTOR MATERIAL, Inc. (part number: CSB02039). The dimensions of the chip carrier are displayed in Fig 2.21 with the unit in inches. The substrate has two layers. The top layer is 300 nm SiO_2 and bottom layer is 500 μm highly doped silicon (0.001~0.005 Ω • cm). The surface of the chip carrier is coated with a gold conducting layer and is directly connected to pin "DB" while electrically insulating to all other pins. Because the device-containing chip is glued on to the chip carrier with conductive silver paste, the pin "DB" is connected directly to the back gate of the device. During the mounting, all the pins of the chip carrier are kept inserted in conductive foam to make sure every pin is properly grounded until the device is

going to be loaded into the transport measurement system. Then wire bonder is used to connect the electrodes of the device to the pins on the socket.

(a) top view:

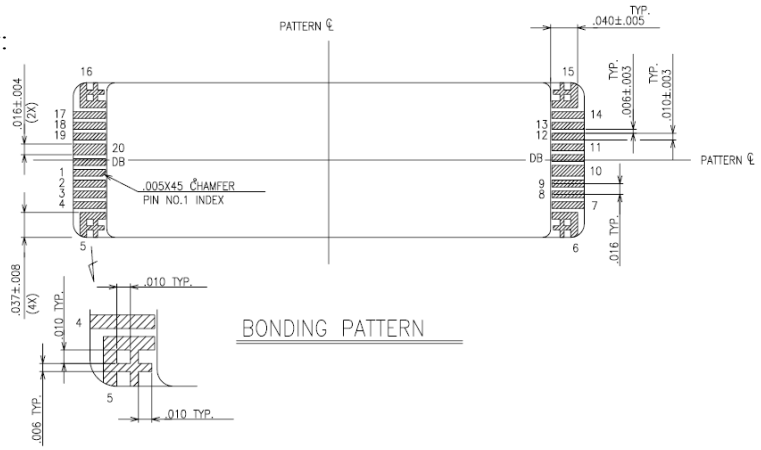

(a) side view:

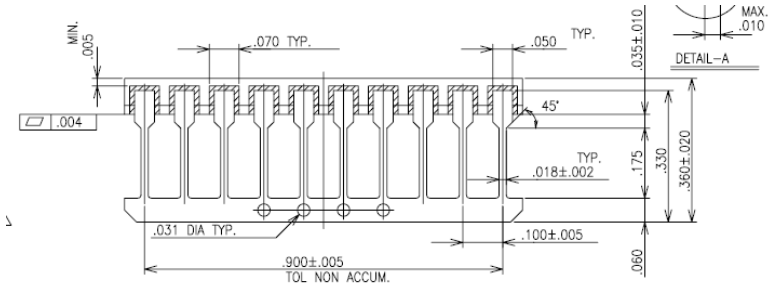

Fig 2.21 Dimensions of the chip carrier for the device mounting. This design image is from the manual of the 20-pin socket from SPECTRUM SEMICONDUCTOR MATERIAL, Inc.

2.3.2 Electrical transport measurements

The transport measurements are performed in an OXFORD VTI (variable temperature inert) system covering a temperature range from 1.5 up to 300 K. A standard SR830 lock-in amplifier is used for the resistance and Hall resistance measurements. Because the lock-in amplifier has a voltage output which can be used as a source, we anchor it with a large constant resistor R_0 to hold the current of the

measurement circuit as a constant. The value of the resistance R_0 needs to be much larger that the device resistance (Fig 2.22). We use a 15 MOhm resistance as the anchor resistor while the device resistance is at the level of several kOhm. The lock-in frequency we use is 1.2727 kHz with a time constant of 30 ms.

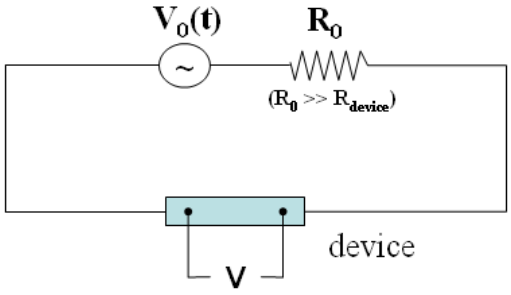

Fig 2.22 Typical circuit diagram of the lock-in measurements of the device resistance.

For the samples with larger and thicker flake size, we utilize the Van der Pauw (vdP) measurement geometry.[37] The sample flake can be cut into a rectangular shape or into a clover-leaf shape as shown in Fig 2.3. In vdP measurements, it states that for a sample with uniform thickness but an irregular shape as in Fig 2.23, the sample resistivity can be determined by measuring the resistances as $R_{MN,OP} = \frac{V_P - V_o}{I_{MN}}$ and $R_{NO,PM} = \frac{V_M - V_P}{I_{NO}}$. Then the sample resistivity is determined by the following equation:

$$\exp(-\frac{\pi d}{\rho} R_{MN,OP}) + \exp(-\frac{\pi d}{\rho} R_{NO,PM}) = 1 \qquad \text{(Eq 2.1)}$$

Here d is the thickness of the sample film and ρ is the resistivity. This equation can be solved numerically through Mathematica software. Although vdP method doesn't depend on the shape of the

samples, in real cases it is still better to cut the sample as regular as possible to get rid of the problem related to the uniformity ness of the sample.

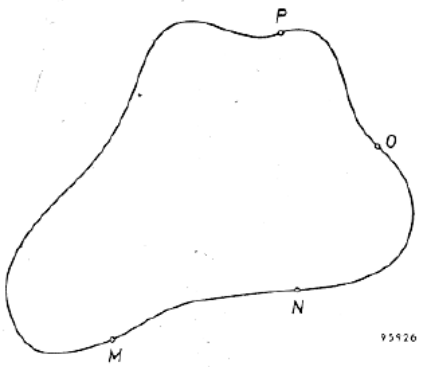

Fig 2.23 The arbitrary geometry of the sample film for the vdP analysis. Four contacts leads are made at the edge of the sample at the points “P”, “O”, “N” and “M”.

For the Hall measurements in vdP geometry, the voltage leads of “P” and “N” do not have to be perpendicular to the flow of the current, because the voltage between “P” and “N” is identical to the voltage path from “P” to “ N’ ” and from “ N’ ” to “N”. The path of P-N’ is perpendicular to the current flow. The voltage between N’ and N will be canceled before and after applying the magnetic field. This is only true when we don’t consider the magnetoresistance of the sample. If magnetoresistance exists, the voltage between N’ and N before and after applying the magnetic field will not cancel each other. However, this can be solved by applying negative direction of the magnetic. Upon applying negative direction of the magnetic field, the voltage between P and N’ will changes sign, while the voltage between N’ and N stays constant. Hence subtracting these two signal will give twice of the Hall voltage in vdP geometry.

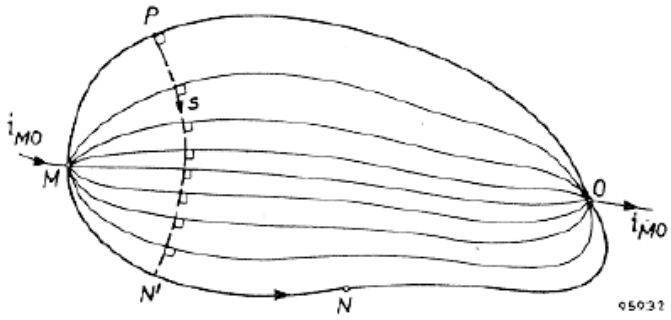

Fig 2.24 The geometry of the sample film in the vdP measurement of the Hall resistance. vdP method states that the transverse leads do not need to be perpendicular to the flow of the current, which makes vdP method still valid in the measurement of the Hall resistance.

Chapter 3 Electrical transport properties of the high mobility states in Bi_2Se_3 band gap

One of the promising properties of the surface states of a topological insulator is its spin-momentum locking. As a consequence of this, an extra energy is required to reverse the momentum of the electron, because it also requires spin flipping. Hence, on the surface of a 3D topological insulator with non-magnetic impurities, the momentum scattering is suppressed.[16,17] The suppression of the momentum scattering will lead to high mobility electrical transport. This property is quite similar to the condition in the Quantum Hall state; however, no external magnetic field is necessary in the case of a topological insulator. In our research on the electrical transport of topological insulators, we aim to demonstrate this enhanced mobility for the topological surface states.

3.1 Control the Fermi level in Bi_2Se_3 thin flakes

3.1.1 Issues of the Fermi level modulation

Two major issues exist in the Fermi level modulation of the Bi_2Se_3 thin flakes.

The first issue is the atmospheric doping and degradation induced Fermi level change after the exfoliation of the thin flakes as mentioned in section 2.2.1. The consequence of this makes it very hard to control the Fermi level in thin flakes even though the doping of the bulk material is properly controlled. The effect of degradation becomes much stronger in smaller and thinner nano-devices.

In our studies, more than a hundred nano-devices have been made through nano-fabrication processes. These devices are always n-type metallic even the original materials is at the compensation point (Fig 2.18). To reach p-type device, very large p-doping material is necessary. Fig 3.1 shows two typical devices exfoliated from p-type bulk material. The bulk material is $Ca_{0.02}Bi_{1.98}Se_3$, which has a

Ca doping level of 2%. As indicated in the paper *Z. Wang Appl. Phys. Lett. (2010)* [32], 2.0% Ca is the highest doping among all our materials. The bulk material we used to make the devices in Fig 3.1 has a p-type carrier density of about 3.62×10^{18} cm^{-3}. However, after exfoliation and device fabrication, Device (I) has a p-type carrier density of about 1.42×10^{19} cm^{-3}, while Device (II) has a n-type carrier density of about 8.25×10^{18} cm^{-3}. The decrease and even the sign change of the Hall coefficient in nano-device strongly indicates that the nano-fabrication processes increase the Fermi level of the thin flake material. From the device images we can see that Device (I) is a very large (~10 μm size) and thicker (70 nm) piece and Device (II) is extremely small (~1 μm size) and relatively thinner (approximately ~ 20 nm). The results indicate a stronger degradation in smaller samples. Furthermore, as shown in Fig 3.1, the gate modulation of the resistivity is very small and the field effect mobility is only about 400 cm^2/Vs, which indicates the trivial carriers dominate the electrical transport.

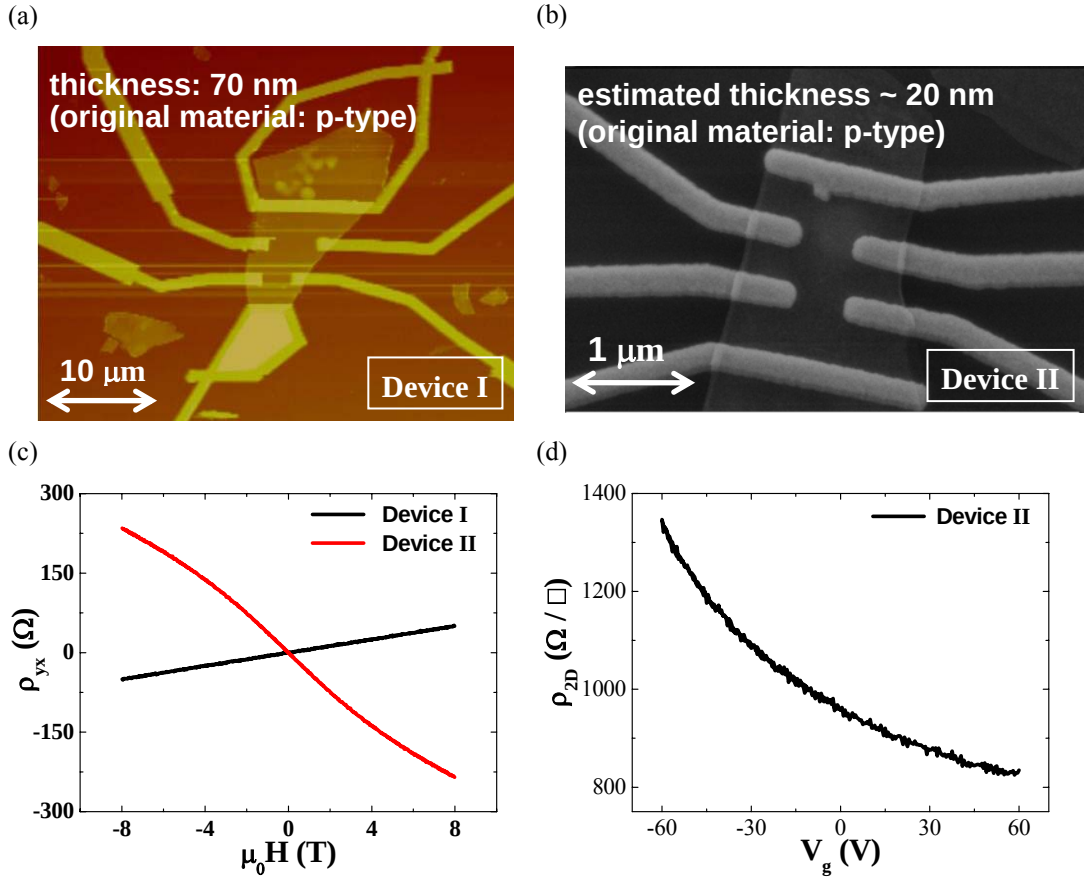

Fig 3.1 Devices made from the p-type Bi_2Se_3 material with 2.0% Ca doping. The device in (a) has a size of 10 μm and thickness of 70 nm. The device in (b) has a size of 2 μm and an estimated thickness around 20 nm. The results in (c) and (d) demonstrate that both of the devices have their Hall coefficients changed after the lithography compared to the value in the bulk material and Device II even becomes n-type.

The second issue is the surface band bending, which has a similar effect to the electrostatic gate modulation of the Fermi level.[35,38] In Fig 3.2, a schematic band structure of Bi_2Se_3 is demonstrated. The surface of Bi_2Se_3 material is exposed to a vacuum or atmosphere. It tends to be n-doped due to the formation of Se vacancies and results an increase of the surface chemical potential with respect to the

inner bulk. The electrons will then diffuse from Bi_2Se_3 surface toward the bulk to align the overall Fermi level. In the end, positively charged Se vacancies sites are left, which forms local electric field near the surface and bends the energy band downward. The bending of the bulk energy band will form 2D electron gas states near the surface as well as shift the relative surface Fermi level. Hence, even though the bulk material has its Fermi level staying inside the band gap, the surface energy band could still be n-doped and could be covered by surface 2DEG states.[38] In Bi_2Se_3 nano-devices, this band bending can be overcome by utilizing both top and bottom electrostatic gating.

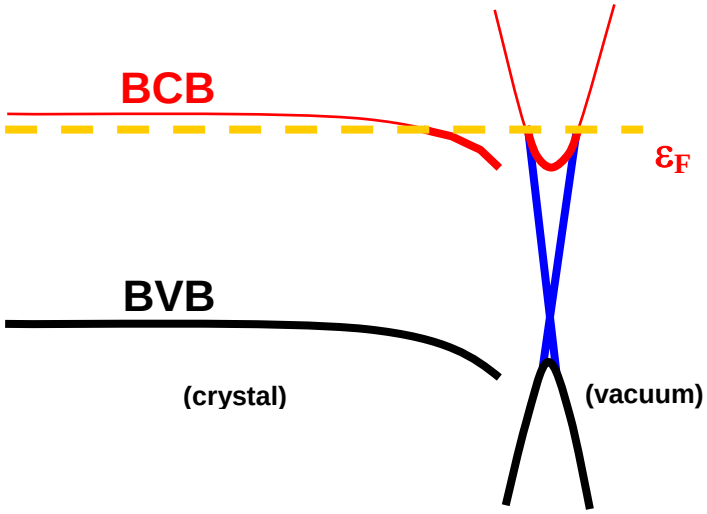

Fig 3.2 Formation of the surface quantum well states for n-type Bi_2Se_3 due to the existence of Se vacancies on the sample surface.

However, in order to achieve surface dominated transport, the overall Fermi level has to be controlled inside the bulk band gap, which will be represented by an insulating behavior of the temperature dependence of the resistance in the nano-devices.

3.1.2 Achieve insulating devices and p-type devices

With the lithography-free method presented in section 2.2.4, the degradation to the nano-devices can be minimized and the Fermi level of the thin flake devices can be maintained similar to its original bulk material. The devices can be taken for measurements right after the exfoliation. Contrary to the results shown in Fig 2.18, which always gives metallic devices from the compensated material, Fig 3.3 shows the resistivity vs. temperature for two typical devices made by the lithography-free method from 1.2% Ca doped compensated $Ca_xBi_{2-x}Se_3$ material. Comparing to the data shown in Fig 2.18, the nano-fabricated device has a resistivity of about 1mΩ • cm at low temperatures, however the lithography-free devices have a resistivity about one order larger. More over, the device resistance increases as temperature decreases, which indicates an insulating behavior and cannot be observed in all devices made by nano-fabrication methods. The p-type devices can also be obtained with this method by exfoliating thin flakes from p-type bulk materials.

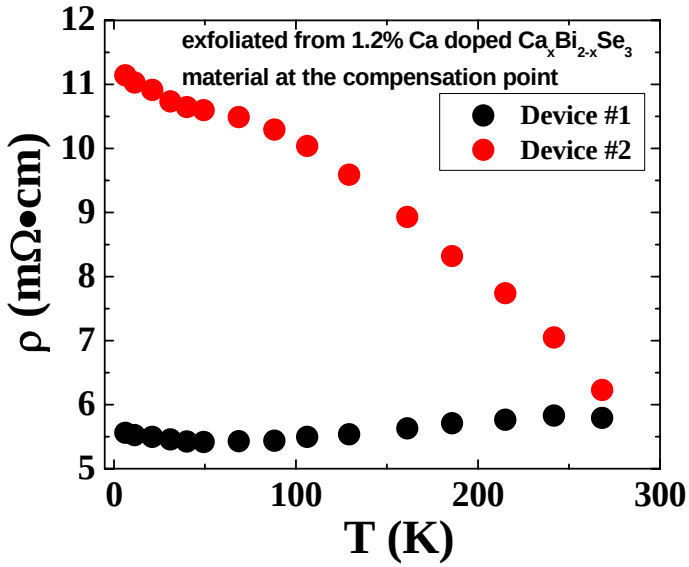

Fig 3.3 The temperature dependence of the devices made by lithography-free method from the compensated material. Both of the devices show insulating behavior.

The two devices in Fig 3.3 are exfoliated from the same bulk material; however, their temperature dependences are different. This probably comes from the non-uniformity of the bulk material near the compensation doping level. The temperature dependence does not resemble a simple activated behavior, which also indicates some degree of non-uniformity. The existence of the non-uniformity results certain randomness on the position of the Fermi level among exfoliated thin flakes. To achieve a systematic continuous control of the Fermi level, other methods are necessary, which should be able to induce a large change of the carrier density directly to the nano-devices. Furthermore, as discussed in chapter 1, the Dirac point of Ca doped Bi_2Se_3 is closer to the valence band top rather than to the conduction band minimum. Starting from p-type device will be more convenient to access the information of the Dirac point. In the following section, I will demonstrate the effect of the electron

beam irradiation on the electron density in nano-devices. Together with the p-type device and electron beam irradiation, we are able to systematically sweep the Fermi level from valence band up across the Dirac point.

3.1.3 The effect of the electron beam irradiation

In our transport studies of Bi_2Se_3 nano-devices, we found a strong effect of electron beam irradiation, which will increase the electron density. Fig. 3.4 demonstrates a typical device made by lithography-free method. The unique character of this device is that it is on top of a gapped cross bar. This character provides a possibility of performing Hall measurements.

The temperature dependence of the pristine device resistance (Fig 3.4 (a)) behaves insulating, while the Hall resistance is non-linear and dominated by electron carriers. As the temperature drops, the resistance increases by more than two-fold and the resistivity at low temperature (1.5 K) is about 11.2 mΩ • cm. The pristine device is then exposed to high density electron beam irradiation, which has a total dosage of about 0.56 C/cm^2 (equals to about 3.52×10^{18} electrons/cm^2), and cooled down to low temperature quickly after the irradiation. After the exposure, the divergent behavior of the temperature dependence of the resistance becomes much weaker (red curve in Fig 3.4 (a)) and the resistivity at 1.5 K drops to about 6.6 mΩ • cm. From the Hall resistance measurements (Fig 3.4 (b)), we can see that before exposure the electron density is about 4.1×10^{13} cm^{-2} at 1.5 K, but after exposure it becomes 1.3 $\times10^{14}$ cm^{-2}. This strongly supports that the electron beam irradiation increases the electron density in thin flake devices.

The Hall mobility of the device is also estimated. It is about 403 cm^2/Vs before the exposure, and changes to about 214 cm^2/Vs after the electron beam irradiation. Although the temperature dependence

of the resistance shows an insulating behavior, it is not a simply activated behavior with a single barrier. Combining the fact that the Hall resistance is non-linear and is dominated by electron carriers, multiple conducting channels should exist together inside the system and the Fermi level position should be similar to the position in Fig 3.2. Hence, rather than dominated by high mobility surface states, the mobility of the pristine device is still low. The effect of the electron beam irradiation increases the Fermi level up closer to the bulk conduction band and, as a result, lowers the Hall mobility of the device. To utilize the effect of the electron beam irradiation and extract the topological surface states in transport, we need p-type starting device.

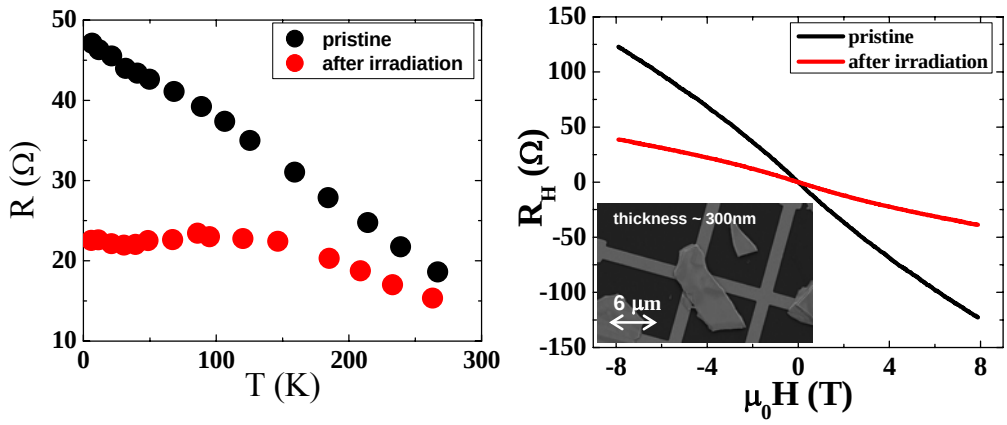

Fig 3.4 Effect of large dose electron beam irradiation for a pristine lithography-free device. After the irradiation, the temperature dependence becomes more metallic and the electron density increases.

3.1.4 Fermi level modulation using electrostatic gating

Another method of tuning Fermi level in thin flake device is the electrostatic gating. Extra electrons can be added or extracted from Bi_2Se_3 thin flakes utilizing the geometry of a parallel capacitor. This geometry has been widely used in graphene devices. Fig 3.5 demonstrates the geometry.

The Bi_2Se_3 thin flake is considered as one of the capacitor plates. The doped silicon wafer is considered as the other plate. The SiO_2 layer is the dielectric layer inside the capacitor. In the measurement, the Bi_2Se_3 thin flake is set to ground and the gate voltage is applied through the doped silicon wafer.

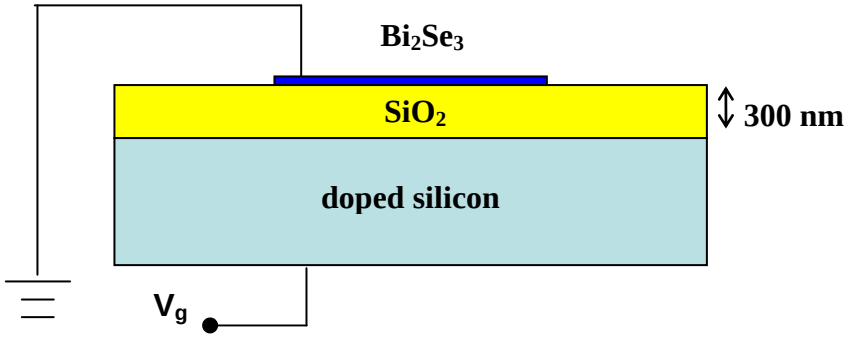

Fig 3.5 The geometry of the back gating of a conventional Bi_2Se_3 device.

The added charge can be calculated with Eq. 3.1, which reflects the carrier density change inside the device. Here ε_0 and ε are the vacuum permittivity and the dielectric constant of the insulating layer (ε = 3.9 for SiO_2). The thickness of the layer is d ~ 300 nm. Fig 3.6 demonstrates the electrostatic gating data of a typical device. The carrier density is measured from Hall resistance. The plot of the carrier density vs. gate voltage shows a straight line with a slope of 7.43×10^{10} cm^{-2}/V, which is close to the value calculated from 300 nm SiO_2. In our measurements we found that normally a gate voltage sweep from -60 to +60 V is safe for the nano-devices. Larger gate voltage sweeping is relatively dangerous and will burn the device sometime. With a gate voltage sweeping of about 100 V, the carrier density can be tuned by ~ 1×10^{13} cm^{-2}, which is relatively small and is suitable to fine tune the Fermi level.

$$\Delta n_{2D} = \frac{\varepsilon_0 \varepsilon}{ed} \Delta V_g \qquad \text{(Eq. 3.1)}$$

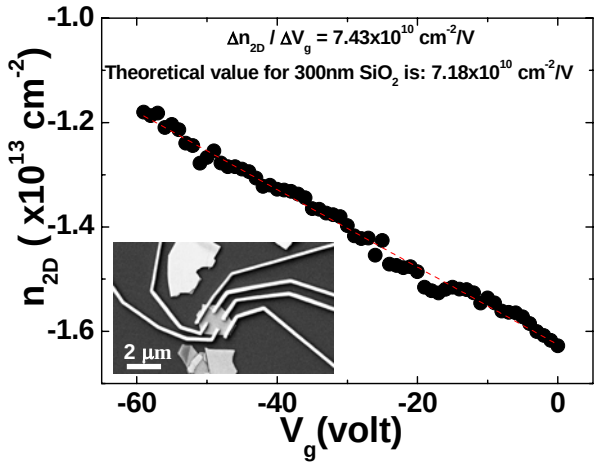

Fig 3.6 The gate tuning of the carrier density in a conventional Bi_2Se_3 device. The carrier density is determined from the Hall measurement.

Different from graphene, which is a single atomic layer, the Bi_2Se_3 device always has a certain thickness of several tens of nanometers. The charge induced by the electrostatic gate tends to accumulate within a very thin layer near the interface between Bi_2Se_3 and SiO_2. Hence, this method is most effective to tune the density of Bi_2Se_3 surface that is adjacent to the SiO_2 layer. The details of the gate tuning will be further discussed in section 3.3.

3.2 Temperature dependence of the device resistivity and the position of the Fermi level

Another superior advantage of p-type device can be seen by comparing Fig 3.2 with Fig 3.7. As mentioned in section 3.1.1, because of the formation of Se vacancies on the surface of Bi_2Se_3, the bulk energy bands bend downward in the depletion layer near the surface. The conduction band bottom near the surface is partially filled up (as demonstrated in Fig 3.2) and forms trivial 2D electron gas states, which participate in electrical transport and mask the properties of topological surface states. The existence of the 2D electron gas makes the device transport complicated, even though the Fermi level is

placed inside the bulk band gap. However, if the Fermi level is placed close or into the bulk valence band, such 2D states can not be formed. As demonstrated in Fig 3.7, because of the downward bending of the energy bend, the bulk valence band inside the depletion layer is fully filled up and does not contribute to electrical transport. Only the hole states inside the crystal and the gapless topological surface states contribute to the transport. Based on this initial p-type condition, if we can shift the Fermi level up out of the bulk valence band, then the only channels contributing to the transport will be topological surface channels and the temperature dependence of the device resistance will change from metallic type into insulating type.

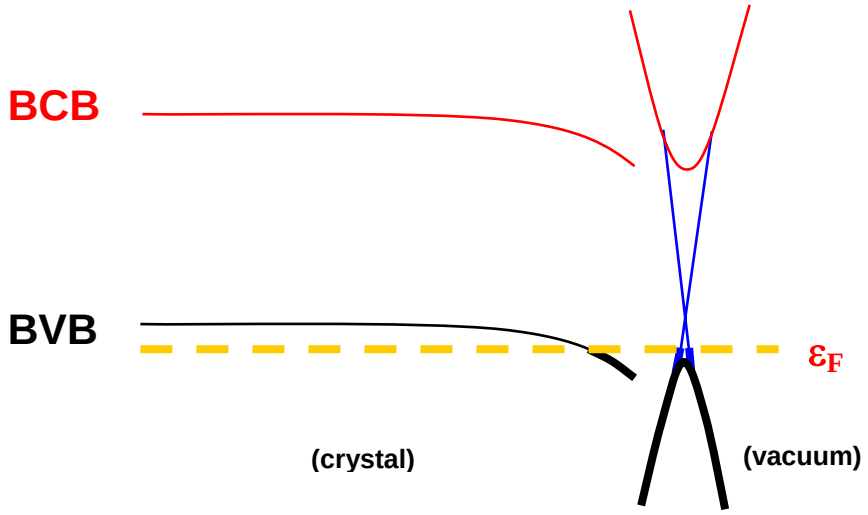

Fig 3.7 The demonstration that the quantum well states won't be able to form on the surface of the p-type Bi_2Se_3 device, which shows the advantage of the p-type material.

3.2.1 Experimental data

The p-type devices can be obtained from 1.4% Ca doped Bi_2Se_3 bulk material with lithography free method as mentioned in section 3.1.2. The device is then exposed under electron beam irradiation with controlled dosage. Fig 3.8 demonstrates a typical device, which is scanned by the electron beam.

The thickness of the device is around 200 nm. The temperature dependence of the device resistivity is shown in Fig 3.9 for different electron beam irradiation conditions as represented by the dosage listed in Table 3.1.

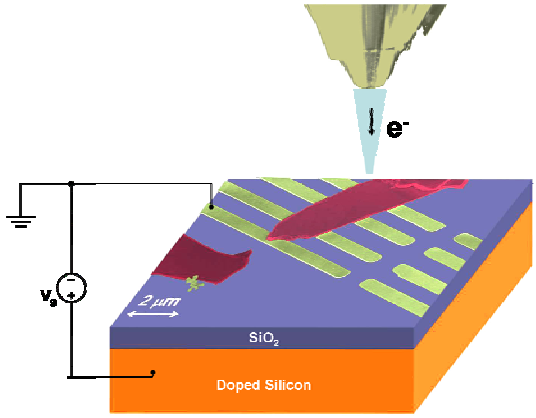

Fig 3.8 The demonstration of the electron beam treatment to the pristine lithography-free device.

In its pristine state or D_0 (Fig 3.9 (a)), the device clearly behaves metallic as indicated by a monotonic decrease of the resistivity as the temperature is lowered, with a residual 2D resistivity or sheet resistance of ~ 110 Ω/□ at 1.5 K, confirming that its chemical potential is located inside Bulk Valence Band (BVB). Upon receiving electron irradiation, a resistivity upturn appears at low temperatures, indicating an activated behavior. The higher the electron dose, the larger the increase in resistivity and consequently the onset of the resistance upturn is at a higher temperature. At sufficiently low temperatures, the activated behavior is taken over by saturation. The saturation resistivity value increases by nearly an order of magnitude, from 110 to 860 Ω/□, as the electron beam dosage progressively increases. Above some intermediate temperature ~150 K, the device returns to the metallic behavior, recovering the same temperature dependence as in the pristine state. This can be attributed to the dominance of the BVB carriers in the degenerate state. The temperature dependence is

completely reversible and the metallic behavior at high temperature is exactly repeated, suggesting that the electron beam irradiation only shifts the position of the chemical potential but does not destroy the properties of the device.

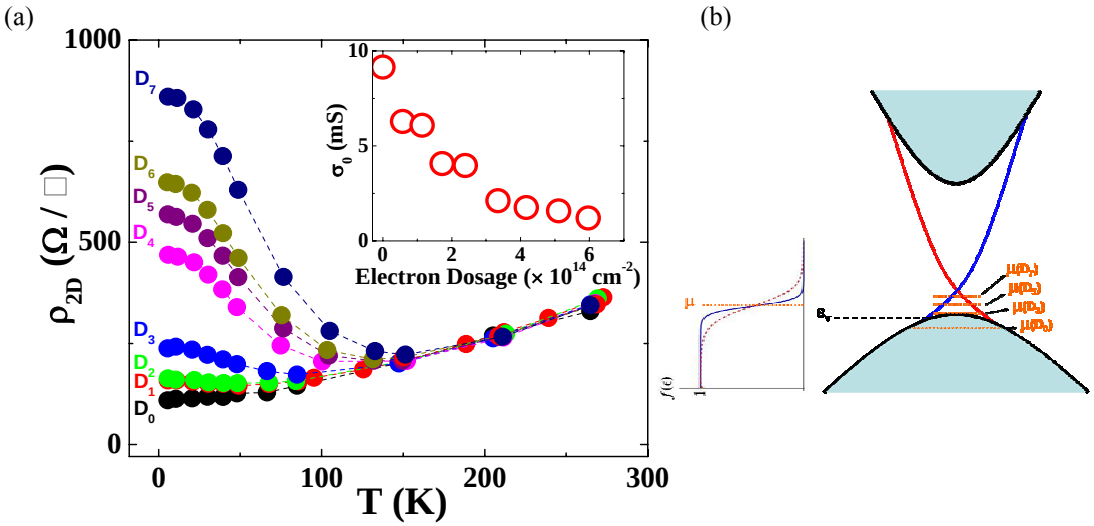

Fig 3.9 (a) Temperature dependence of the device sheet resistance under different electron beam exposure conditions with a +60 V in gate voltage. The low-temperature residual resistance starts to rise as the device receives a higher dosage of electron beam irradiation. The inset shows the dependence of the zero-temperature sheet resistance as a function of electron beam dosage. The zero-temperature sheet resistance is obtained from fitting the curves in Fig 3.10 with the model described in the text. (b) Illustration of the chemical potential position for different electron beam exposures. The highest chemical potential is ~8 meV above BVB.

3.2.2 The model of the temperature dependence

We then model the conductivity by $\sigma(T) = \sigma_B(T) + \sigma_0$, where $\sigma_B(T)$ represents the contribution from the thermally excited bulk carriers, which can be expressed in terms of the bulk

carrier mobility $\mu_B(T)$ and the hole density $n_h(T)$, i.e. $\sigma_B(T) = e\mu_B(T)n_h(T)$. The total hole density n_h in BVB can be obtained by integrating over all unoccupied states, $n_h = \int_{-\infty}^{\varepsilon_v} D_h(\varepsilon)[1-f(\varepsilon)]d\varepsilon$ with $f(\varepsilon) = \frac{1}{1+e^{(\varepsilon-\mu)/k_BT}}$, and μ being the chemical potential. Here we assume a 3D density-of-states $D_h(\varepsilon)$ for bulk carriers with an effective mass m_h*, and then we have $n_h = 2(\frac{m_h^* k_B T}{2\pi\hbar^2})^{3/2} e^{(\varepsilon_v-\mu)/k_BT}$. Based on the fact that the resistivity curves overlap with each other in the degenerate state, we assume that the bulk mobility $\mu_B(T)$ is not sensitive to electron dosage. In the pristine state D_0, the chemical potential is always located inside BVB. Just as in degenerate semiconductors or metals, its resistivity $\rho_{D_0}(T)$ or conductivity $\sigma_{D_0}(T)$ derives primarily from $\mu_B(T)$, i.e. $\sigma_{D_0}(T) \sim \mu_B(T)$, which is assumed to be independent of electron dosage. Then the total conductivity is expressed as $\sigma(T) = A\frac{T^{3/2}}{\rho_{D_0}(T)} e^{-(\mu-\varepsilon_v)/k_BT} + \sigma_0$, which fits very well to our low-temperature data with three fitting parameters: A, σ_0 and $(\mu-\varepsilon_v)$ (Fig 3.10 (a)). In the inset of Fig 3.10 (a), the activation energy $(\mu-\varepsilon_V)$, which is the slope of the straight lines in the $\log[(\sigma-\sigma_0)\rho_{D_0}T^{-3/2}]$ vs. 1/T plot, increases as the electron dosage increases. At the largest dose, μ is shifted by the maximum amount to ~8.2 meV above the BVB edge, well into the band gap.

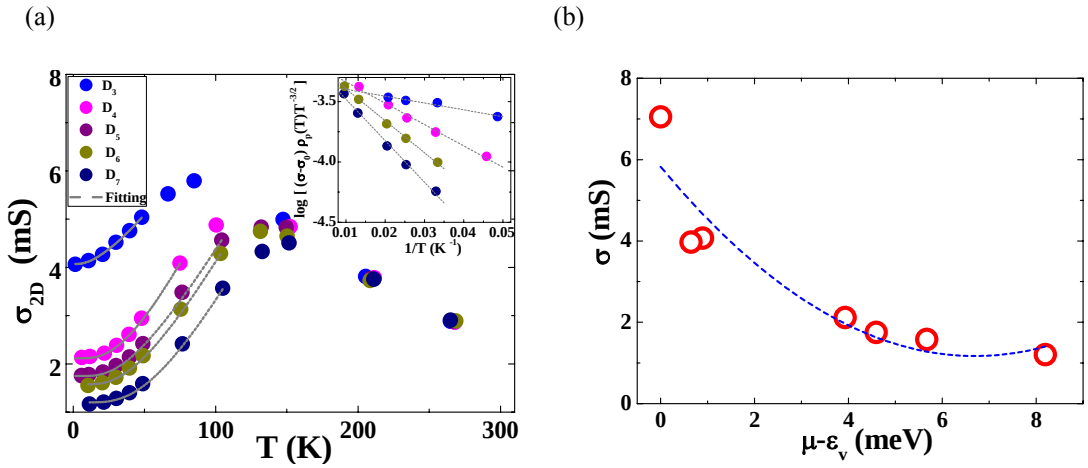

Fig 3.10 (a) Device conductivity as a function of temperature for different electron doses. Solid lines are the fits as described in the text. The inset shows the linear dependence of $\log[(\sigma-\sigma_0)\rho_{D_0}T^{-3/2}]$ on 1/T, a thermally activated behavior. (b) Zero-temperature conductivity vs. chemical potential measured form the BVB edge. The blue dotted line is the quadratic fit described in the text.

	Electron Beam Dose ($x10^{14}$ cm^{-2})	Electron Energy (keV)	$\mu - \varepsilon_v$ (meV)
D_0	-	-	< 0
D_1	0.58	4.0	< 0
D_2	1.14	4.0	< 0
D_3	1.72	6.0	0.89
D_4	3.35	8.0	3.93
D_5	4.17	10.0	4.59
D_6	5.11	9.0	5.67
D_7	5.97	12.0	8.20

Table 3.1 Electron dose (electron counts per unit area) and electron energy vs. resulting chemical potential position under different exposures.

σ_0 is the conductivity at T=0, which decreases as a function of the electron dosage as displayed in the inset of Fig 3.9. σ_0 stems from the extended states within the gap. Fig 3.10 (b) shows how σ_0 varies with (μ-ε_V), the position of the chemical potential measured from the BVB edge. In general, σ_0 is described by the mobility μ_g and the density of these carriers $n(\mu)$ in the gap, i.e. $\sigma_0(\mu) = e\mu_g n(\mu)$. If the conductivity is solely contributed by the gapless Dirac fermions, it should go to its minimum as the chemical potential inches towards the Dirac point. Let us assume that μ_g does not sensitively depend on the carrier density (shown in Fig 3.11), and the gapless surface states follow a linear dispersion relation. Then we have $\sigma_0 \propto (\varepsilon_D - \mu)^2 = [(\varepsilon_D - \varepsilon_v) - (\mu - \varepsilon_v)]^2$, here ε_D being the

energy of the Dirac point and parameter (ε_D-ε_v) being the Dirac point position measured from the BVB edge. We fit this μ-dependence to the data in Fig 3.10 (b) and find that the Dirac point is located at ~6.7 meV above the BVB edge where the minimum conductivity is located. In the range from 4 to 8 meV, the conductivity stays finite, which is probably caused by another parallel conduction channel which will be discussed in section 3.3.

3.2.3 Discussions

Although the exact role of the electron beam is not completely known, the excess electrons introduced by the electron beam irradiation may act as defects that localize the free holes that are abundant in the initial p-type material, resulting in an up-shift of the chemical potential. With more electron beam irradiation, the chemical potential leaves the BVB and enters the band gap (Fig 3.9 (b)). Thus, the free holes in BVB can only be thermally activated; as a result, the chemical potential sinks towards BVB at high temperatures. Below 10 K where the thermally activated carriers are exponentially suppressed, however, a finite resistivity or a residual conductivity σ_0 exists, which can only originate from the extended states in the bulk band gap.

3.3 Gate dependence of the device resistivity and the field-effect mobility

3.3.1 Experimental data

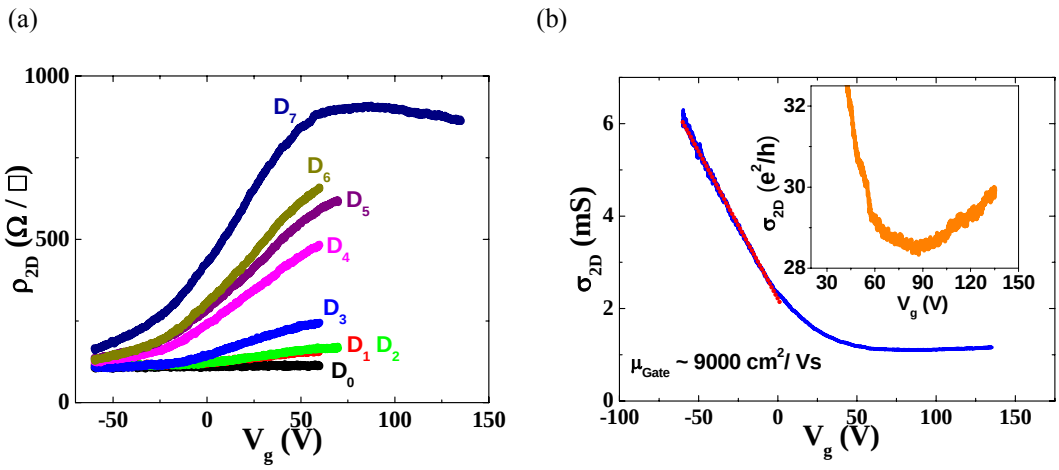

Fig 3.11 (a) Gate dependence of the sheet resistance for different electron irradiation conditions measured at 1.5 K. As the dosage increases, the resistance modulation becomes larger. (b) Gate dependence of the resistance for D_7 at 1.5 K. The linear fit yields a field effect mobility of ~9000 cm^2/Vs. The inset magnifies the gate voltage range between 30 and 140 V. A clear conductivity minimum can be seen, which corresponds to ~28.5 times of the quantum conductance (e^2/h).

At 1.5 K, the thermally activated carriers are exponentially suppressed; therefore, only the extended states in the gap are responsible for the finite resistivity ρ_{2D}. The V_g-dependence of ρ_{2D} is shown for all electron beam doses, i.e. from D_0 to D_7 in Fig 3.11 (a). Clearly, the pristine state D_0 has negligible V_g-dependence, which is expected because the gate modulation of the carrier density is relatively small in the degenerate state. Upon electron beam irradiation, as the chemical potential moves towards and then enters the band gap, ρ_{2D} starts to rise as V_g sweeps from -60 to +60 V. This

occurs since large V_g tends to deplete the holes, which results in a more rapid rise of the chemical potential. With more electron beam irradiation, the gate response becomes stronger. The largest resistance modulation occurs in D_7, i.e. from 165 Ω/□ (-60 V) to 910 Ω/□ (+80 V). Fig 3.11 (b) inset shows a zoom-in plot with a clear minimum of $\sim 28.5\frac{e^2}{h}$ for state D_7. This minimum conductivity is still much greater than $\frac{e^2}{h}$, the order of the minimum conductivity expected for 2D Dirac fermions.[5,7] The excess conductivity could originate from either electron and hole density fluctuations due to charged impurities near the Dirac point of the surface states as often seen in graphene, or the 3D impurity band in the gap as discussed by other groups.[19,39]

3.3.2 High mobility states inside the band gap

To quantify the gate tunability, we calculate the field effect mobility μ_g from the slope of conductivity vs. V_g using $\sigma_{2D} = e\mu_g n_{2D} = e\mu_g \frac{C_g}{e} V_g$. Here we first assume that the electrostatic gating only induces a surface Dirac fermion density modulation. C_g is the capacitance per unit area. In our device geometry, the flake is supported by 50 nm-thick gold electrodes on a 300 nm thick SiO_2 dielectric layer, which yields an effective C_g ~70 aF/μm^2. Then the slope of the conductivity in Fig 3.11 gives rise to μ_g ~9000 cm^2/Vs. Fig 3.12 displays the effective mobility μ_g as a function of ρ_{2D} evaluated from several conductivity curves with different irradiation doses, which represents how mobility varies as the chemical potential rises. This result is rather surprising. In the pristine state, the mobility is as low as 800 cm^2/Vs, which can be viewed as the mobility of the bulk carriers in $Ca_xBi_{2-x}Se_3$. As the electron beam pierces through the device, it induces defects to localize the bulk carriers, and we would expect the mobility to degrade. On the contrary, the field-effect mobility

increases by more than a factor of 10. Note that the charge modulation due to gating does not only affect the Dirac fermion state density but also that of the other aforementioned parallel channel. Hence, the charge modulation of the gapless surface states is apparently overestimated, which leads to an underestimation of the field effect mobility. Nevertheless, this mobility value represents a lower bound for the gapless surface states. As the conductivity decreases further at higher gate voltages, it approaches a plateau near the minimum, and the field-effect mobility is expected to drop to zero.

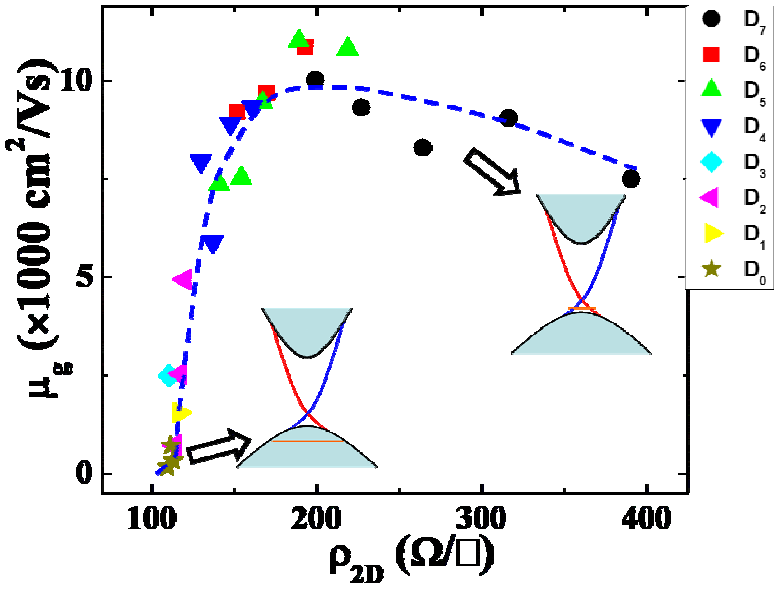

Fig 3.12 Field effect mobility as a function of the sheet resistance calculated in several different states of the device at 1.5 K.

3.3.3 Discussions

To better understand the effect of the electron beam irradiation, we compare the consequence between the electron beam exposure and an applied gate voltage. Fig 3.13(a) displays the temperature dependence of the resistivity in the most resistive state D_7 for two gate voltages: +60 and 0 V. Compared with +60 V, the activated behavior is evidently weaker at 0 V, which brings the resistivity

curve close to that of state D_4 at +60 V (Fig 3.9 (a)). Clearly, the gain of additional holes due to the lowering of V_g from +60 to 0 V just offsets the loss of holes removed by the electron beam irradiation from D_4 to D_7. The mutual equivalence of these two processes reveals that the electron beam irradiation merely shifts the chemical potential without causing any irreversible effects.

We also found that the effect of the EBI can be negated by exposing it in air at room temperature. Fig 3.13(b) displays the temperature dependence of the device resistivity at V_g=0 V. After the device is processed with EBI, its temperature dependence becomes insulating (orange curve in Fig 3.13(b)). The insulating behavior can be maintained if the device is kept at low temperatures inside the transport measurement chamber. We then take the device out of the chamber and leave it in air at room temperature for a long period (~ 48 hours). It becomes metallic again (green curve in Fig 3.13(b)). However, the air exposure does not cause any permanent change to the device. If we perform EBI again and quickly start the measurement, we find that the insulating state is restored (blue curve in Fig 3.13(b)). Hence, we believe that the low-intensity EBI (~10^{14} electrons/cm^2) simply affects the position of the Fermi level and the effect is reversible.

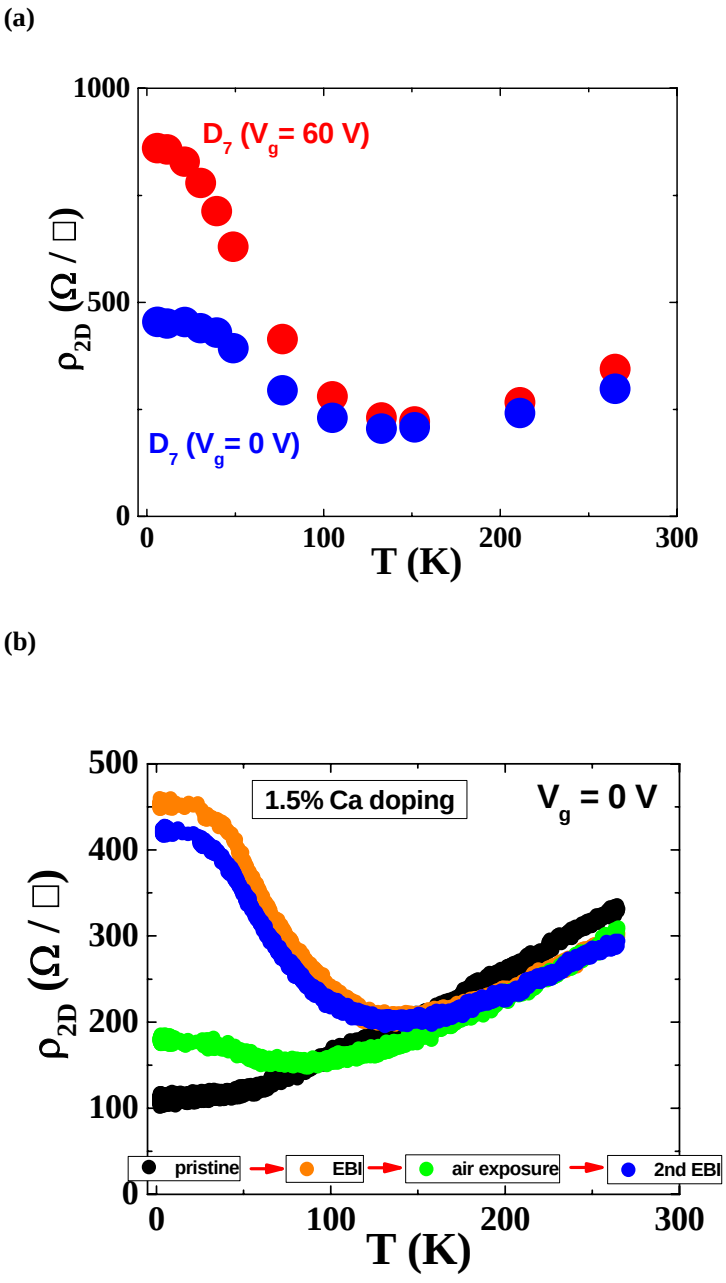

Fig 3.13 (a) Effect of gate voltage on the temperature dependence of the device resistance of D_7. A lower positive gate voltage negates the effect of a high dosage electron beam exposure. (b) The effect of atmospheric exposure after EBI. This data is from the same device whose results are shown in Fig 3.9 (a).

3.4 Electrical transport under magnetic fields

3.4.1 Experimental Data

We have also systematically performed magnetoresistance (MR) measurements in the most resistive state D_7 as we gradually shift the chemical potential away from BVB with electrostatic gating. Fig 3.14 shows the evolution of MR as a function of V_g at 1.5 K. At -60 V, σ_{2D} is ~6.1 mS. As seen in Fig 3.10 (b), this is the case when the chemical potential touches the BVB edge, i.e. $(\mu - \varepsilon_v) \sim 0.3$ meV, and the bulk band holes dominate the transport. At +60 V, σ_{2D} is ~1.1 mS, corresponding to a $(\mu - \varepsilon_v)$ value of ~8 meV, which is close to the Dirac point. Besides some minor features, the most distinct characteristic is the evolution of the overall MR behavior. In the high field region (> 4 T), the slope of MR steadily decreases as the chemical potential is moved into the band gap and turns negative. This feature can be better seen in Fig 3.15, where a MR ratio is calculated with respect to the zero field resistance. At -60 V, the maximum MR ratio is ~60%, the largest to begin with. It decreases as the chemical potential enters the band gap. At ~+30 V, the maximum MR region in the 2D plot marks the sign change of the MR slope.

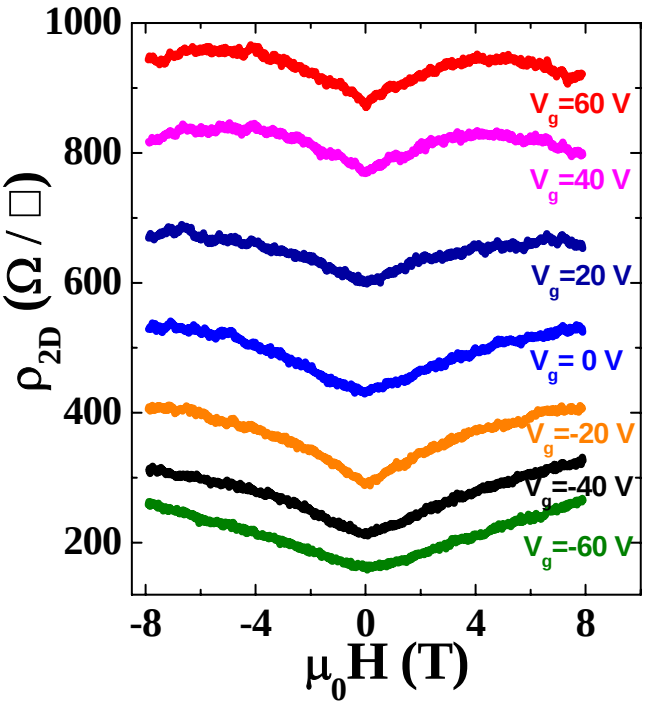

Fig 3.14　Magnetic field dependence of the sheet resistance at different gate voltages at 1.5 K.

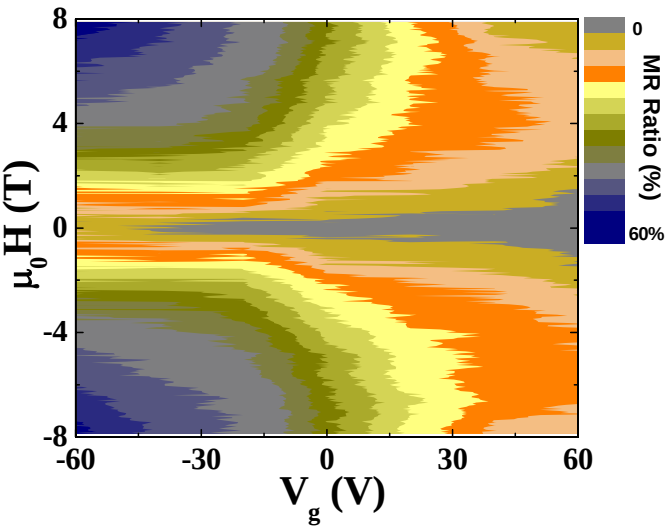

Fig 3.15　2D plot of calculated MR ratio vs. magnetic field and gate voltage. A negative MR slope region can be clearly seen.

3.4.2 Possible origins of the low field cusp and the modulations through electrostatic gate

Another distinct feature is the low-field behavior shown in Fig 3.16, which singles out the two extreme cases. At +60 V, which corresponds to the highest chemical potential position in the gap, the low-field MR develops a clear cusp which can be fitted well with the weak-anti-localization (WAL) model,[40] i.e. $\Delta\sigma = \sigma(B) - \sigma(0) = \frac{\alpha e^2}{2\pi^2\hbar}[\ln\frac{\hbar}{4Bel_\phi^2} - \Psi(\frac{1}{2} + \frac{\hbar}{4Bel_\phi^2})]$ with $\alpha \sim 0.5$, here l_Φ being the de-coherence length and Ψ being the digamma function. The fit gives l_Φ~324 nm. l_Φ drops to ~170 nm at V_g=40 V. As the de-coherence length approaches the mean-free-path, the magnitude of the low-field cusp dramatically decreases. This is consistent with the WAL phenomenon in the symplectic limit, i.e. due to the strong spin-orbit coupling in two-dimensional electron systems. Similar expression was derived for two-dimensional electron systems and graphene in the context of strong spin-orbit scattering. For gapless surface states of 3D TI, the spin-orbit interaction is inherently strong; therefore, the WAL effect naturally arises as the chemical potential rises above the BVB edge and well-defined two-dimensional surface states gradually develop.[23,41,42] In contrast, the cusp feature is absent in the other case when the transport is dominated by 3D band carriers.

The high-field negative MR could arise from two possible origins: the weak-localization (WL) effect and a Zeeman gap opening near the Dirac point. In the latter scenario, the states near the Dirac point are pushed downward to lower the chemical potential and consequently to cause the resistance to decrease. More experimental evidence is needed to elucidate the physical origin of this negative MR.

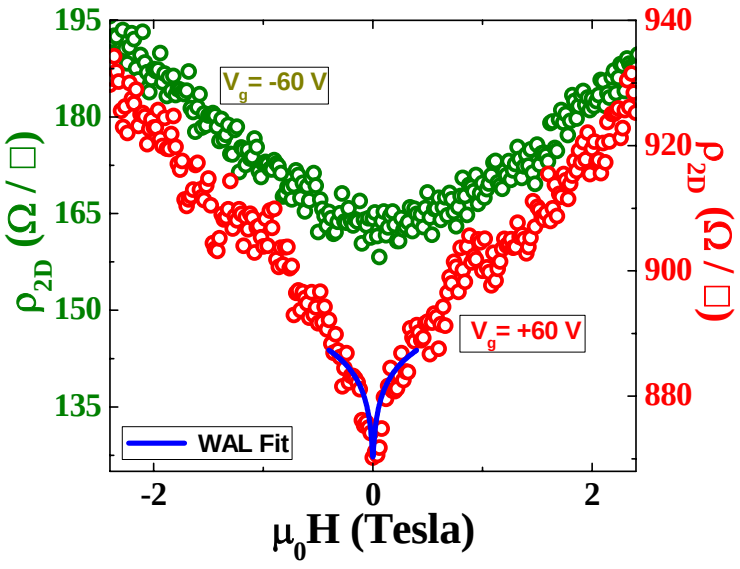

Fig 3.16 Two extreme cases showing the contrast of the low-field MR feature. The blue line for V_g= +60 V is a fit with the weak-anti-localization model in the symplectic regime. The fitting yields a de-coherence length of ~324 nm.

3.4.3 Signature of the gate tunable Shubnikov de Hass oscillations

Besides the overall features of the MR data, there are also small modulations on the MR raw data that are symmetric to the magnetic field. For example, red curve in Fig 3.16, symmetric features appear at +1.1 T and -1.1 T, although there is a background shift on the y-axis. To analyze these, we first take a moving average to the raw data. In Fig 3.17, the MR data at V_g = +60 V (red curve in Fig 3.16) is shown. The raw data is shown in black, from which we can already see many small modulations. The orange curve shows the data after the moving average within adjacent 8 points. In the raw data, the points are measured in an interval of 0.02 T. Then, the window for the 8 points moving average is 0.16T, which is much smaller than the width of the modulations. The overall MR background should be even to the magnetic field. The asymmetric in our MR data is attributed to the mixing of Hall

contribution, which is odd to the magnetic field. To remove the contribution of the Hall contribution, we symmetrize the MR data as $\frac{\rho_{2D}(B)+\rho_{2D}(-B)}{2}$. Based on this data, we fit the MR curve with the 4th order polynomial fitting (Fig 3.18). Then by removing the fitted background curve from the original data, we can single out the field dependence of the small modulations.

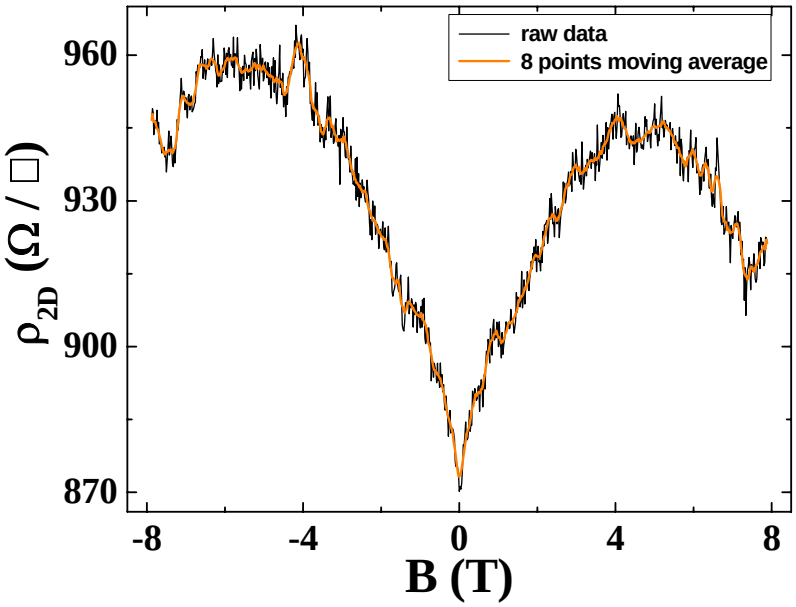

Fig 3.17 The 8-point moving average of the MR data at V_g = +60 V (red curve in Fig 3.16).

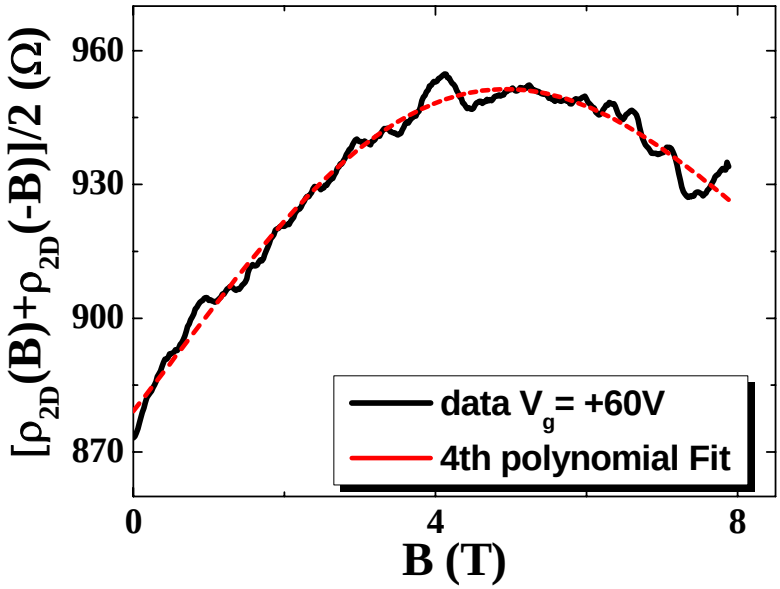

Fig 3.18 Magnetoresistance data in positive magnetic fields and a smooth fourth-order polynomial fit.

We call the difference between the fitted background curve and the original data as $\Delta\rho_{2D}$. Fig 3.19 plots $\Delta\rho_{2D}$ v.s. 1/B. We can see clear oscillations which are evenly spaced as plotted against 1/B. For the Landau Level analysis, we have $2\pi(n+\gamma) = S_F \frac{\hbar}{eB}$, where γ is the Berry phase, n is the Landau Level indices and $S_F = \pi k_F^2$ is the cross-section Fermi surface area. We then can calculate the filling factor as $\nu = n + \gamma = \frac{2\pi k_F^2}{(2\pi)^2} / (\frac{2eB}{h}) = \frac{n_{2D} h}{2eB} = \frac{B_F}{B}$. Here we include the Berry phase inside the filling factor ν. At filling ν = 2, it should be a dip, but it shows a peak on the data. This could be caused by another set of SdH oscillations. There are apparently two sets of oscillations in Fig 3.19: slow and fast ones in 1/B. The Fourier transform of the slow set is shown in the inset and the peak gives the SdH oscillation frequency B_F in 1/B of ~10.3 T. This B_F corresponds to a carrier density of ~4.99x10^{11} cm^{-2}. There are not enough data points for the fast oscillations to obtain the frequency or the

carrier density. At this gate voltage (+60 V), the resistance is near its maximum; therefore, the carrier density obtained from B_F is close to its minimum.

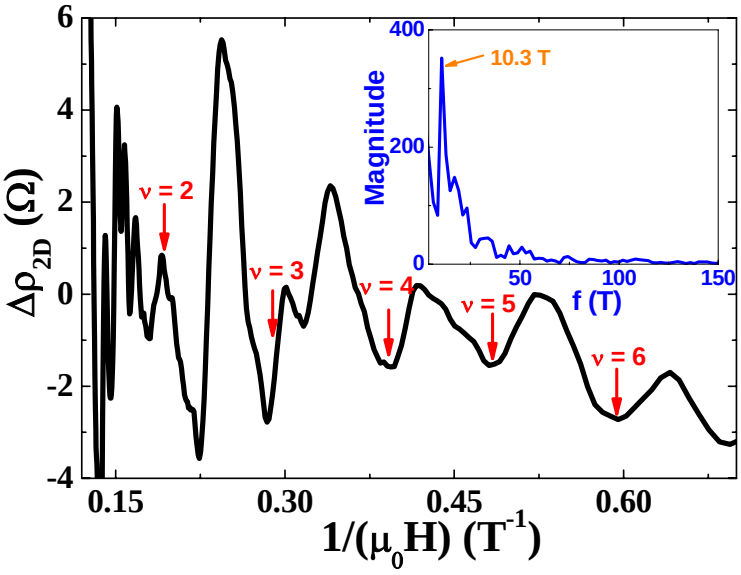

Fig 3.19 After the background removal, the SdH oscillations become much clearer. At high fields, another fast SdH oscillation set exists, which overlaps with the ν=2 feature in the slow SdH set. The inset shows the FFT spectrum of the low-field oscillations.

We also did the similar analysis to the data at other gate voltages. Fig 3.20 is the MR data before the removal of the background and is plotted against the magnetic field B. In order to clearly compare them, each data is added by an arbitrary y-axis offset, which won't affect the magnetic field position of the small modulations. After labeling them with the filling factors, a clearly trend of the Landau Level shift can be seen, especially for the ν = 6 filling.

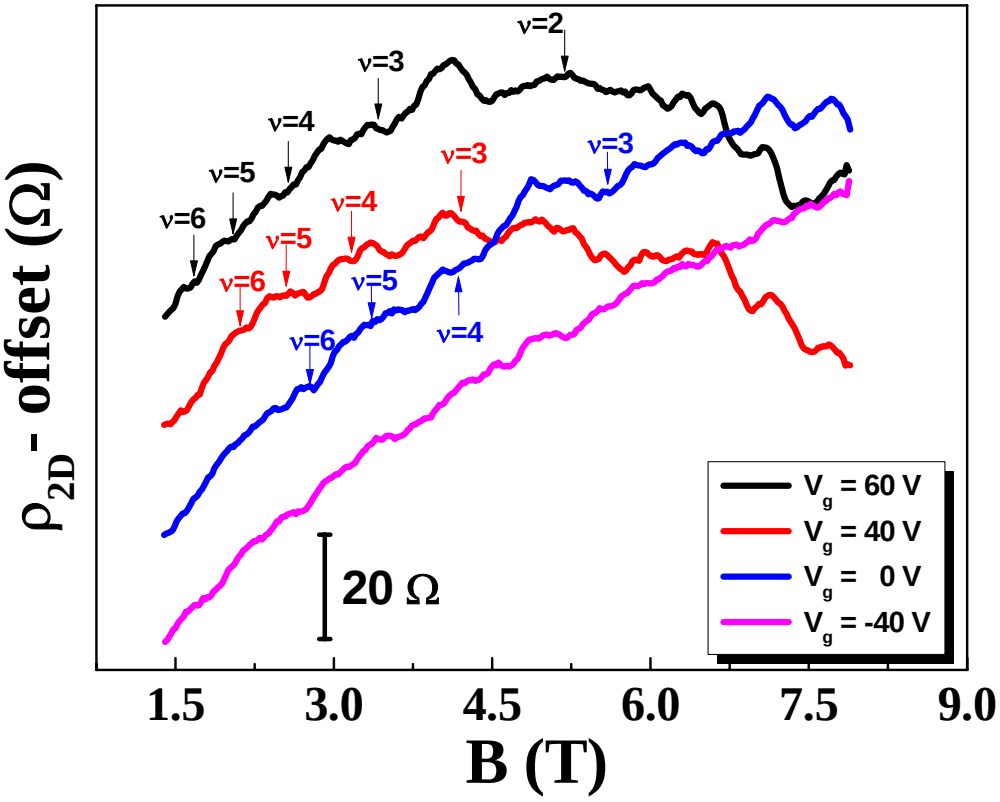

Fig 3.20 The shift of the oscillation features on the raw MR data at different gate voltages. There is an y-axis offset applied to each curve in order to compare them in the same scale. Although the oscillations are small, the filling factors can be correctly labeled and the ν=6 filling shows a clear shift.

We assume that this density is the density of the bottom surface, which can be easily modulated by the back gate. Then the fast SdH oscillations probably correspond to the top surface, which should not be very sensitive to the gate voltage. Our estimation of the Thomas-Fermi screening length also supports this in section 3.4.4. In Fig 3.21, the filling factor ν v.s. 1/B is plotted for three gate voltages. We see a clear gate voltage dependence of the carrier density, indicating a gate modulation of the surface Dirac fermion density.

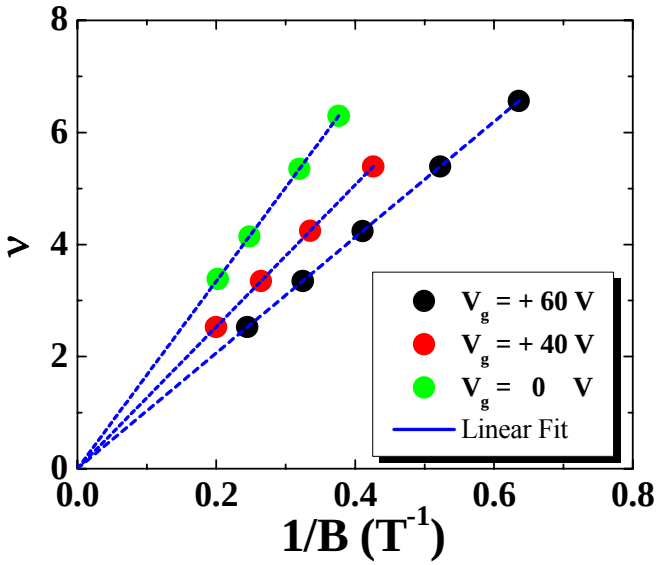

Fig 3.21 A plot of the filling factor ν v.s. 1/B for three different gate voltages.

From the SdH analysis of the bottom surface, we obtained the following carrier density. At +60 V, B_F = 10.319 T, n_{SdH} = 4.99x10^{11} cm^{-2}; at +40 V, B_F = 12.661 T, n_{SdH} = 6.12 x 10^{11} cm^{-2}; at 0 V, B_F = 16.726 T, n_{SdH} = 8.09 x 10^{11} cm^{-2}. Therefore, from +60 to +40 V, the carrier density change calculated from the SdH data is Δn_{SdH} = 1.13 x 10^{11} cm^{-2}; from +40 to 0V, this change is Δn_{SdH} = 1.97 x 10^{11} cm^{-2}. The latter is 1.74 times as large as the former (roughly ~ 2). On the other hand, the total carrier density change in the capacitor due to the gate voltage change is ~4.37 x 10^{10} $cm^{-2}V^{-1}$. For a 20 V gate voltage change, Δn_{Gate} = 8.74 x 10^{11} cm^{-2}. For a 40 V gate voltage change, then Δn_{Gate} = 1.75 x 10^{12} cm^{-2}. Hence, from +60 to +40 V, the ratio $\Delta n_{SdH}/\Delta n_{Gate}$ is ~12.9%. From +40 to 0V, $\Delta n_{SdH}/\Delta n_{Gate}$ is about 11.3%.

Clearly, only a small fraction of the Dirac fermion surface carriers are affected by the gate voltage sweeps. From those data and the field-effect mobility we obtained from the gate dependence, we can estimate the mobility of the surface Dirac fermions that are responsible for the SdH oscillations. From

+60 to +40 V, $d\sigma/dV_g$ gives a field-effect mobility of 1112 cm^2/Vs. Therefore, the surface state mobility is 8620 cm^2/Vs. From +40 to 0V, $d\sigma/dV_g$ gives a field-effect mobility of 3776 cm^2/Vs, which corresponds to a surface mobility of 33415 cm^2/Vs. These mobility values are much greater than that of 3D carriers from the bulk. This indicates that the field-effect mobility represents a lower-bound for the Dirac fermion surface states.

3.4.4 Thomas-Fermi screening length

We believe that the fast SdH oscillations are due to the top surface which is ~ 200 nm away from the bottom surface in the device shown in Fig 3.8. Unlike in thin film devices, here the gate voltage should leave the top surface carrier density relatively untouched, since the Thomas-Fermi screening length is much shorter than the sample thickness *d*. Here is how we estimate the screening length λ_{TF}.

First, we have $\lambda_{TF} = 1/k_{TF}$ and $k_{TF}^2 = \frac{e^2}{\varepsilon\varepsilon_0}\frac{\partial n}{\partial \mu}$. In the band gap, the screening carriers are from the bulk impurities. We can obtain the Fermi energy change as a function of the carrier density from our experimental data. For example, for state D_7, the Fermi level (μ-ε_V) is ~ 0 meV when the gate voltage is at -58.06 V, which corresponds to the conductivity of ~ 6 mS; (μ-ε_V) is ~ 2.99 meV when the gate voltage is at -5.96 V for the conductivity of ~2.6 mS. We again assume that most of the gate modulated carriers affect the bulk impurity states. The total gate modulated carrier density change is then $\Delta n_{2D} = \Delta V_g * C_g/e$. The device thickness is d=200 nm. The 3D carrier density can be calculated as $\Delta n_{3D} = \Delta n_{2D}/d$. For $\Delta\mu$ = 2.99 meV in the Fermi energy change, the carrier density change is ~ Δn_{3D} =1.14 x 10^{17} cm^{-3}. The dielectric constant ε is taken to be 9. Then, the Thomas-Fermi screening length is λ_{TF} = 3.6 nm, which is much smaller than the sample thickness. Therefore, we believe that the top surface carrier density is not significantly affected by the gate voltage.

Chapter 4 Techniques for the thermoelectric transport measurement in nano-devices

4.1 Introductions to thermoelectric effects

In the transport studies of the materials, we always provide a "driving field" that causes the carriers to mobilize. As a response to the "driving field", a current flow of carriers inside the material is formed. The basic two types of current flows are charge current $\vec{j}$ and heat current $\vec{j}^{q}$. With thermodynamic relations, the flow of the energy or energy current $\vec{j}^{\varepsilon}$ can then be expressed as $\vec{j}^{\varepsilon} = \vec{j}^{q} + \mu \cdot \vec{j}^{n}$, where μ is the chemical potential and $\vec{j} = -e \cdot \vec{j}^{n}$. The mobile carriers interact with the material and the responses normally tell us the properties of the material. In electrical transport, an external electric field $\vec{E}$ is applied. The charged carriers will drift under this electric field and at the same time they are scattered due to the interaction with the ions of the material (phonon scattering) or impurities of the material. Hence, the electric transport normally tells us the scattering properties. Besides this, a spatial chemical potential gradient $\vec{\nabla}\mu$ or temperature gradient $\vec{\nabla}T$ can also drive the carriers and cause the carriers to diffuse. In general, a heat current $\vec{j}^{q}$ and a charge current $\vec{j}$ inside a material can be expressed in terms of the driving fields $\vec{E}$, $\vec{\nabla}\mu/e$ and $\vec{\nabla}T$ through macroscopic equations as:

$$\begin{cases} \vec{j} &= L^{11}\vec{\varepsilon} + L^{12}(-\vec{\nabla}T) \\ \vec{j}^{q} &= L^{21}\vec{\varepsilon} + L^{22}(-\vec{\nabla}T) \end{cases}, \text{ where } \vec{\varepsilon} = \vec{E} + \frac{\vec{\nabla}\mu}{e} \qquad \text{(Eq. 4.1)}$$

The processes described by these equations are reversible. The coefficients L^{11}, L^{12}, L^{21} and L^{22} are related to each other through Onsager relations and they determine the thermoelectric coefficients in thermoelectric effects. The coefficients L^{11}, L^{12}, L^{21} and L^{22} can be directly derived from Boltzmann transport equations, which describe the material properties and will be discussed in secession 4.1.4.

4.1.1 Seebeck effect

In Seebeck effect, a constant temperature gradient is built up along the sample as the "driving field". As shown in Fig 4.1, a temperature gradient $\vec{\nabla}T$ is applied onto a rectangular sample with p-type carrier. Due to this temperature gradient, the carriers inside the material will diffuse toward the low temperature side of the sample and will accumulate there (open circuit measurement), which increases the chemical potential of the carriers and build up an opposite field $\vec{\nabla}\mu/e$. In the steady state, these two processes equalize and a voltage difference appears across the sample due to chemical potential difference. This voltage ΔV is so called thermo-voltage and the thermopower is then defined as $S = -\Delta V / \Delta T$.

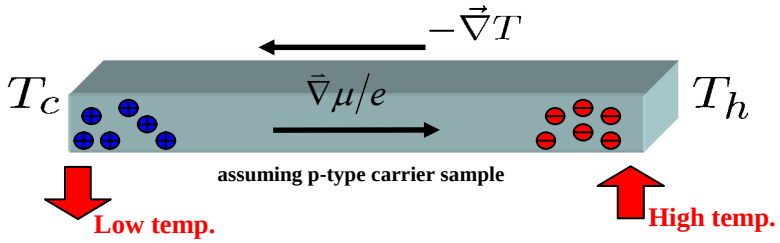

Fig 4.1 The schematic graph of the Seebeck effect in a p-type sample.

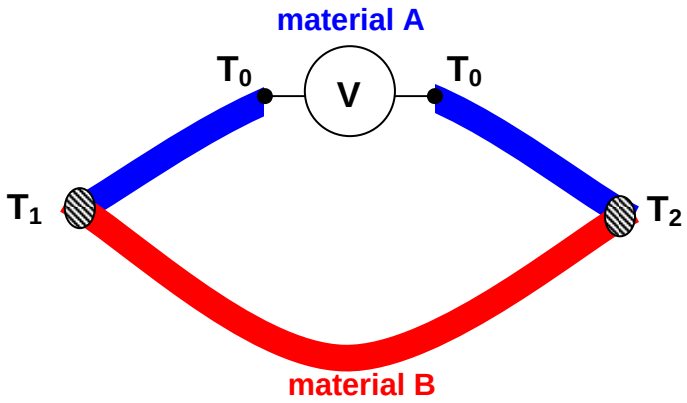

Fig 4.2 The standard geometry for the measurement of the thermo-voltage.

In actual measurements (Fig 4.2), we always need to use one material (material "A") as voltage leads to measure the thermopower of the other material (material "B"). A common setup for the measurement is demonstrated in Fig 4.2. Two materials with different Seebeck coefficient S_A and S_B are connected together at different temperatures T_1 and T_2. The voltage meter is connected to material "A" at a temperature point T_0. In the steady condition, there is no net charge current flow inside the materials. As mentioned in Fig 4.1, for material "A", a thermo-voltage between temperature T_0 and T_1 is $\Delta V_A^1 = S_A(T_0-T_1)$ and the thermo-voltage between T_2 and T_0 is $\Delta V_A^2 = S_A(T_2-T_0)$. Same for material "B", the thermo-voltage between T_1 and T_2 is $\Delta V_B = S_B(T_1-T_2)$. If material "A" and "B" have different Seebeck coefficient, there will be a net voltage on the voltage meter as $\Delta V = \Delta V_A^1 + \Delta V_A^2 + \Delta V_B = (S_A-S_B)(T_2-T_1)$. Therefore, by knowing the Seebeck coefficients of one material the Seebeck coefficient of the other material can be measured. Also, if the Seebeck coefficient of the measurement leads (material "A") is much smaller than that of the sample (material "B"), for example $S_A << S_B$, then the Seebeck coefficient of the sample can be estimated as $S_B = \Delta V/(T_1 - T_2)$.

4.1.2 Peltier effect:

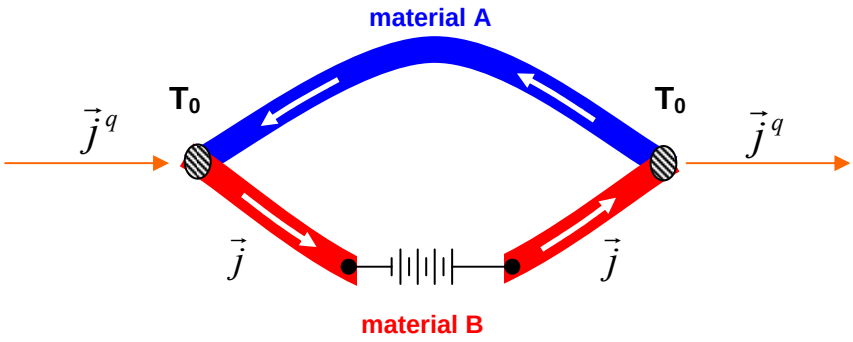

Fig 4.3 The geometry for the measurement of the Peltier effect.

A reversed process of the Seebeck effect is the Peltier effect, in which a charge current induces the flow of a heat current. During this process, the temperature of the material is held at constant T_0, so the flow of the charge carriers is isothermal. The isothermal charge current flow will be accompanied by a heat flow and the relation between them is described by the Peltier coefficient Π as: $\vec{j}^q = \Pi \cdot \vec{j}$. This equation implies that the Peltier coefficient represents the heat per charge of the charge carrier transfers.

To separate the heat current from the charge current in Peltier effect, a typical set up is demonstrated in Fig 4.3. Material "A" and "B" are connected at two points. They are both held at temperature T_0. A charge current $\vec{j}$ is passed through the loop, while keeping the temperature of the whole loop constant. The flow of $\vec{j}$ causes the heat flow inside material "A" and "B" separately as: $\vec{j}_A{}^q = \Pi_A \cdot \vec{j}$ and $\vec{j}_B{}^q = \Pi_B \cdot \vec{j}$. Because of the difference between the two Peltier coefficients Π_A and Π_B, a net flow of the heat current generated by this set up is $\vec{j}^q = \vec{j}_A{}^q - \vec{j}_B{}^q = (\Pi_A - \Pi_B) \cdot \vec{j}$.

4.1.3 Nernst effect

The Seebeck effect is related to the longitudinal voltage built up along the direction of the temperature gradient $\vec{\nabla} T$, while the Nernst effect is related to the transverse voltage built up perpendicular to the direction of the temperature gradient $\vec{\nabla} T$ under the presence of an external magnetic field. The basic mechanism of Nernst effect is similar to the Hall effect, whereas the flow of the carrier is induced only by temperature gradient $\vec{\nabla} T$.

Fig 4.4 demonstrates a typical setup for the measurement of the Nernst signal. Similar to the condition in Fig 4.1, upon applying a magnetic field a transverse voltage will be built up. Two diffusion processes with opposite directions exist inside the sample. One process is due to the

temperature gradient. The other process is due to the chemical potential difference. Because the carriers diffuse toward opposite directions, they bend oppositely under magnetic field. In the stable state, the Nernst voltage is the net transverse voltage between these two processes.

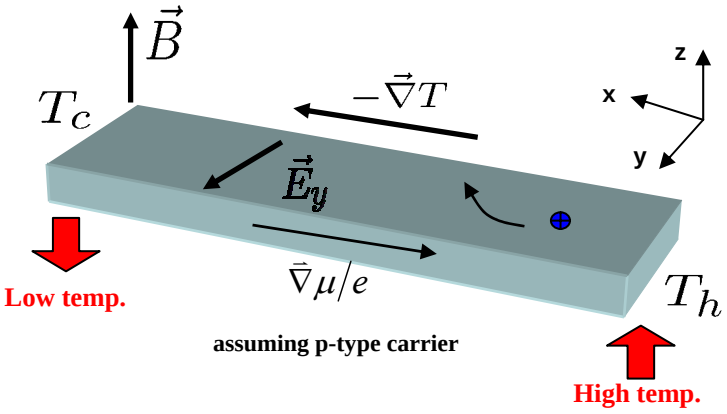

Fig 4.4 The schematic graph for the Nernst effect.

4.1.4 Boltzmann transport equation and thermoelectric coefficients

With Boltzmann transport equation, the evolution of a system is described by the non-equilibrium distribution function $g_n(\vec{r},\vec{k},t)$. Here *n* means the *n*th energy band. If the semi-classical trajectory is followed, then $\vec{r}$ and $\vec{k}$ will depend on time and can be determined through semi-classical equation of motion. Hence, we only consider the time dependence of the distribution function. Together with the scattering time approximation, the distribution function can be written as:

$$g(t) = g^0(t) - \int_{-\infty}^{t} dt' P(t,t') \frac{d}{dt'} g^0(t') \qquad \text{(Eq 4.2)}$$

Here $g^0(t)$ is the distribution function at the equilibrium state and $P(t,t')$ tells the possibility that a carrier survives from the scattering during time t' to *t*, which will contribute the distribution function at time *t*. Combining this equation with the semi-classical equations of motion and relaxation time approximation, the explicit form of the distribution function *g* can be derived. The charge current

density can be written as $\vec{j} = -e\int \frac{d\vec{k}}{4\pi^3}\vec{v}(\vec{k})g(\vec{k})$ and the heat current can be written as $\vec{j}^q = -e\int \frac{d\vec{k}}{4\pi^3}[\varepsilon(\vec{k}) - \mu]\vec{v}(\vec{k})g(\vec{k})$. Then the charge current density and heat current density can be expressed as:

$$\begin{cases} \vec{j} &= L^{11}\vec{\varepsilon} + L^{12}(-\vec{\nabla}T) \\ \vec{j}^q &= L^{21}\vec{\varepsilon} + L^{22}(-\vec{\nabla}T) \end{cases}, \text{ where } \vec{\varepsilon} = \vec{E} + \frac{\vec{\nabla}\mu}{e}$$

and

$$\begin{aligned} L^{11} &= \sigma(\varepsilon_F) \\ L^{21} &= T \cdot L^{12} = -\frac{\pi^2}{3e}(k_B T)^2 \frac{\partial\sigma}{\partial\varepsilon}\bigg|_{\varepsilon_F} \\ L^{22} &= \frac{\pi^2 {k_B}^2 T}{3e^2}\sigma(\varepsilon_F) \end{aligned} \qquad \text{(Eq 4.3)}$$

One important prerequisite for these equations to hold is that the system has to be under the degenerate limit, where the Fermi energy is much larger than the energy k_BT. In this regime, we can see that the Seebeck coefficient (at $\vec{j} = 0$) is simply the coefficient of $\vec{\varepsilon} = S \cdot \vec{\nabla}T$ and $S = \frac{L^{12}}{L^{11}} = -\frac{\pi^2}{3}\frac{{k_B}^2 T}{e}\frac{1}{\sigma}(\frac{\partial\sigma}{\partial\varepsilon})\bigg|_{\varepsilon_F}$. The Peltier coefficient is $\Pi = \frac{L^{21}}{L^{11}} = T \cdot S$. As discussed in section 4.1.2, we have $\vec{j}^q = \Pi \cdot \vec{j}$. Hence, we have $\vec{j}^q = T \cdot S \cdot \vec{j}$, which demonstrates that the Seebeck coefficient is directly the entropy per charge of carrier transfers.[43] From another point of view, $S = -\frac{\pi^2}{3}\frac{{k_B}^2 T}{e}\frac{1}{\sigma}(\frac{\partial\sigma}{\partial\varepsilon})\bigg|_{\varepsilon_F}$, which is the famous Mott's relation, tells us that the Seebeck coefficient is related to the energy derivative of the electric conductivity and it directly probes its energy distribution, therefore it is more sensitive in probing the electronic structures of the materials. These two aspects bring the Seebeck coefficient to be a very important quantity in electric transport in the degenerate limit.

4.2 Measurements of thermoelectric properties in micron-scale devices

4.2.1 Introduction

Building up a temperature gradient is an important step in the measurement of thermopower. In macroscopic samples (at size of several centimeters), the temperature gradient is built up by attaching a piece of resistive heater to one end of the sample wafer, while holding the other end of the sample substrate to a heat sink. Fig 4.5 demonstrates a typical thermopower measurement setup for a 2DEG sample.[44] The size of the sample is around 1 cm. With this set up, the sample can be sealed in vacuum at low temperature to prevent the loss of the heater power through the environment (He^4 gas or He^3 gas). The typical temperature difference that can be built along this macroscopic sample substrate is around 1 K / cm (reference) and is distributed linearly along the substrate except the region very close to the heater.

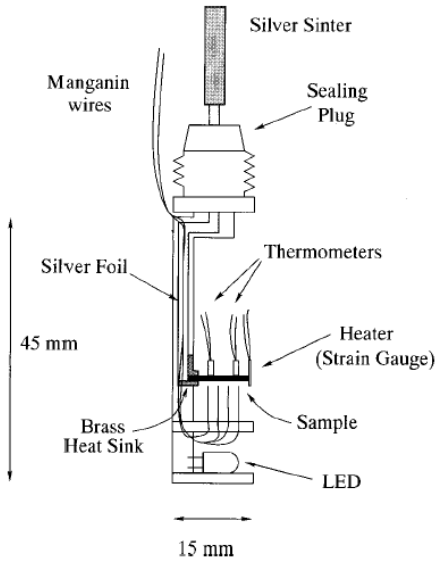

Fig 4.5 The setup for the low temperature measurement of the thermopower. This graph is from the paper of *Tieke, B. et. al., Phys Rev B (1998)*.[44]

However, as the small size of the nano devices (~ 10μm typically), if the nano devices are on top of the sample substrate of this setup, the temperature difference along the device is only in the range of 1 mK. Considering a material with the Seebeck coefficient in the level of 10 μV/K, this set up only provides a thermo-voltage of around 10 nV. In order to have a larger thermo-voltage signal in nano-devices, larger temperature gradient is necessary.

Local heater has been used a lot before in the measurement of thermoelectric properties of carbon nano-tubes to build up large temperature gradient over small length scale. Fig 4.6 demonstrates device geometry for measuring Seebeck coefficient of nano-tube. The bottom image of Fig 4.6 shows that the distribution of temperature gradient is not a constant. It becomes larger when the heater is closer to the sample. We utilize similar geometry as in our measurements.[45-47]

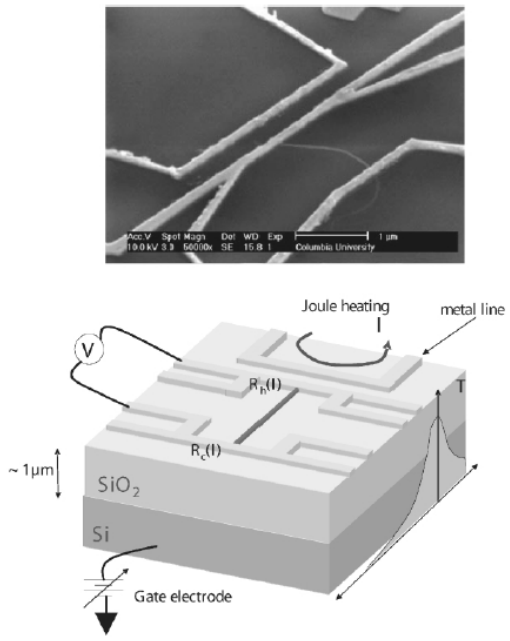

Fig 4.6 The device setup for the thermopower measurement of individual carbon nanotube. This device is from the paper of Small, J. P. *et. al., Solid State Commun* **127**, 181-186.

4.2.2 Design of the micron-scale devices

Graphene:

Fig 4.7 demonstrates a typical graphene devices. The graphene flake is exfoliated on top of 300 nm SiO_2 layer with heavily doped Si as substrate for applying gate voltage. After locating suitable graphene sheets, the flake is etched into a cross geometry by O_2 plasma etching for the purpose of measuring the Nernst signal. We perform standard electron-beam lithography to attach electrodes in the Hall-bar geometry (Fig 4.7). The electrodes consist of 7 nm of Cr and 100 nm of Au, and also serve as local thermometers. The 300 nm silicon oxide acts as the gate insulator. The substrate is sealed in a vacuum can. During the measurement, a heater power is applied using a DC current source, while the other end of the sample substrate is inserted into indium ingot as a heat sink to direct the heat flow through the sample substrate. Detailed methods for the measurement will be discussed in section 4.2.3 and 4.2.4.

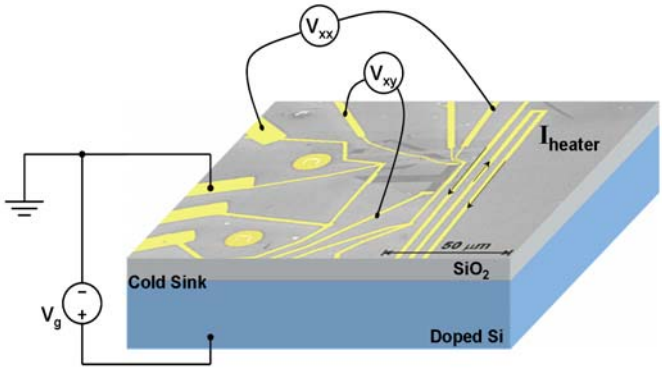

Fig 4.7 The geometry of our nano-device for the measurement of thermopower in graphene.

Graphene has been reported to possess very large thermal conductivity ~ 10^3 W/m • K at room temperature.[48,49] SiO_2 normally has a thermal conductivity of about 1.4 W/m • K at room temperature.

Although the thermal conductivity of graphene is very large, its thickness is very small. So the thermal conductance of the supporting SiO_2 (300nm) + Si substrate is still larger. Fig 4.8 shows an experiment data comparing the thermal conductance between graphene and the 300 nm SiO_2 supporting layer.[48] At about 100 K, the graphene thermal conductance is about 1/5 of the thermal conductance of the SiO_2 supporting layer. Fig 4.9 demonstrates a diagram of the heat channels in the graphene device. Most of the heat current will pass through the substrate and the temperature distribution profile of graphene will follow the distribution of the substrate.

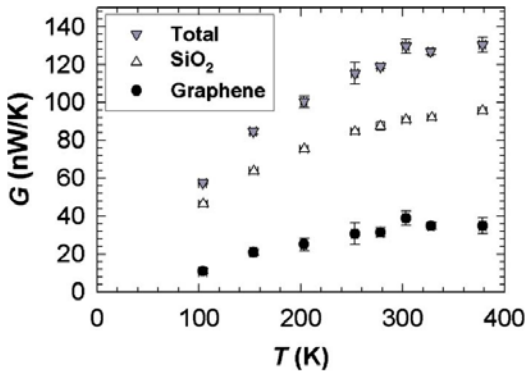

Fig 4.8 The thermal conductance of graphene and the thermal conductance of 300 nm SiO_2 supporting layer. This data is from the paper of *Seol, J. H. et. al., J Heat Trans-T Asme (2011)*.[48]

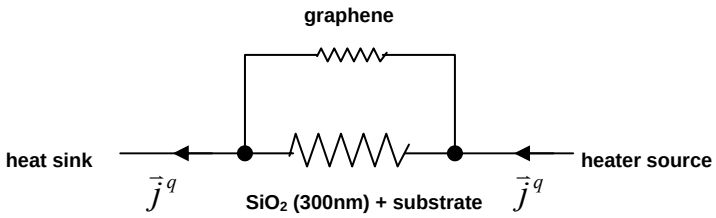

Fig 4.9 The circuit diagram of the heat flow through graphene and the supporting 300 nm SiO_2. Although graphene has very large thermal conductivity, its thermal conductance is still smaller than that of the 300 nm SiO_2. Hence, the temperature profile of the thermopower device is still determined by the substrate.

Bi_xTe_y nano-ribbon device:

Similar device can be fabricated on topological insulator related material, such as Bi_xTe_y nano-ribbon. Fig 4.10 demonstrates a typical device.

A key issue of the measurement of the Bi_xTe_y nano-ribbon device is the contact problem between the metal electrodes and the nano-ribbon. Unlike in graphene device, where a good electric contact can be obtained, the contact problem in Bi_xTe_y nano-ribbon device always brings in larger voltage noise and covers the thermo-voltage signal. Therefore, an AC thermopower measurement with lock-in technique is taken here to measure the Seebeck coefficient. The measurement details will be discussed in section 4.2.4.

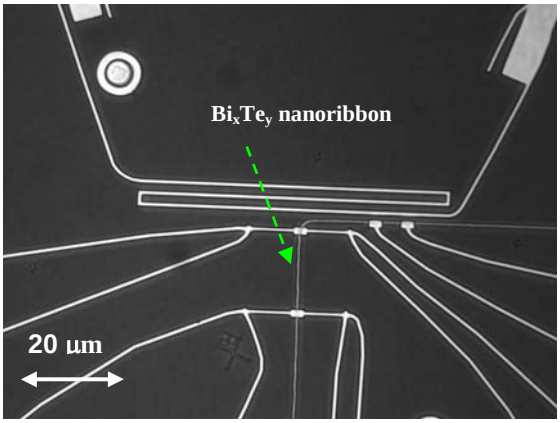

Fig 4.10 The optical image of our thermopower device for Bi_xTe_y nanoribbon.

4.2.3 Design of the device holder for cryogenic environment

The measurement is performed in an Oxford VTI (Variable Temperature Insert) system covering temperature range from 1.5 to 300 K with a magnetic field up to 8 T. The cooling of the sample is achieved by pumping helium gas from the liquid helium dewar. The sample is directly merged inside the helium gas environment, which will cause heat leakage from the heater to the environment and is not good for building up temperature gradient along the sample.

Fig 4.11 shows a typical design for the sample holder. The device substrate is merged into an indium block, which is connected to the heat sink of the sample holder. The heat sink is made of a big copper block to provide large heat capacitance. An indium ring on the copper heat sink is used to seal the copper can. The most distinct feature of our sample holder compared to the one in Fig 4.5 is that nano-devices can be mounted onto our sample holder. For nano-device, wire bonding is necessary to connect device electrodes to the holder's bonding pads, because the electrodes of nano-devices are usually very small, and furthermore, wire-bonder can provide good electrical ground to the devices to

prevent electrostatic shock. However, the wire bonding processes exert force onto the substrate and it requires the substrate to be supported while bonding. Our holder features these, while the device substrate can still be the suspended in the indium heat sink. The thermoelectric measurements of both macroscopic sample and nano-device can be measured with this holder in helium gas environment.

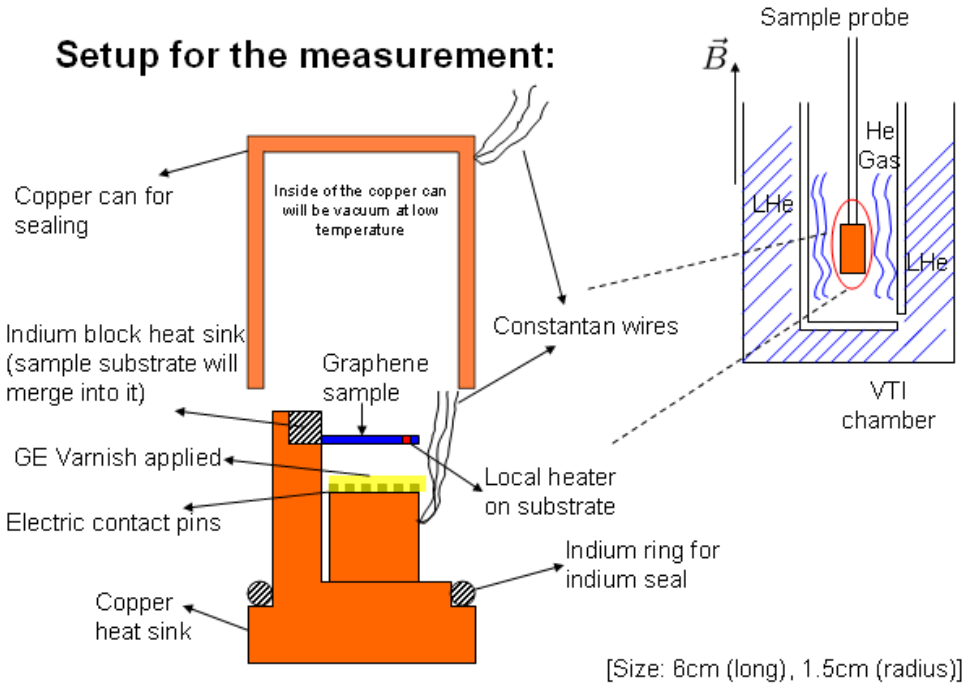

Fig 4.11 The low temperature setup for our measurement of thermopower of graphene device in the VTI chamber.

Fig 4.12 demonstrates the sample mounting processes. The top figure shows all the parts for the sample holder. In Fig 4.12(a), the supporting copper blocks are mounted on the copper heat sink to provide support to the sample substrate. The whole heat sink part is then heated by hot plate to the melting point of indium (~ 157 °C). Then the heat sink part is quickly taken away from the hot plate and the sample substrate is inserted into the melted indium at once. Tweezers are used to holder the sample substrate firmly onto the copper block holder while waiting for the indium to solidify. Therefore, after one end of the sample substrate is held by the solid indium (Fig 4.12(b)), the bonding pad part of the holder is mounted onto the copper heat sink (Fig 4.12(c)) and wire bonding can be performed to the supported device. After wire bonding, the supporting copper blocks can be unscrewed

and taken away, as a result, the sample substrate is suspended (Fig 4.12(d)). The top cap of the holder is then capped onto the copper heat sink (Fig 4.12(e)). An indium ring is applied between the cap and the copper heat sink to provide good vacuum seal. Because the top cap will be connected to the system ground and the copper heat sink is connected to the back gate of the device (the device substrate is doped silicon), electric insulating is necessary between the cap and the copper heat sink. We normally apply a thermo-tape on the rim of the cap before seal the can. After this, a clamp is used to tight the top cap onto the indium ring of the copper heat sink. A low temperature epoxy is applied around the slot between the cap and the heat sink to mechanically hold them. At cryogenic temperature, the air inside the can will be frozen and vacuum can be built inside the sample holder can.

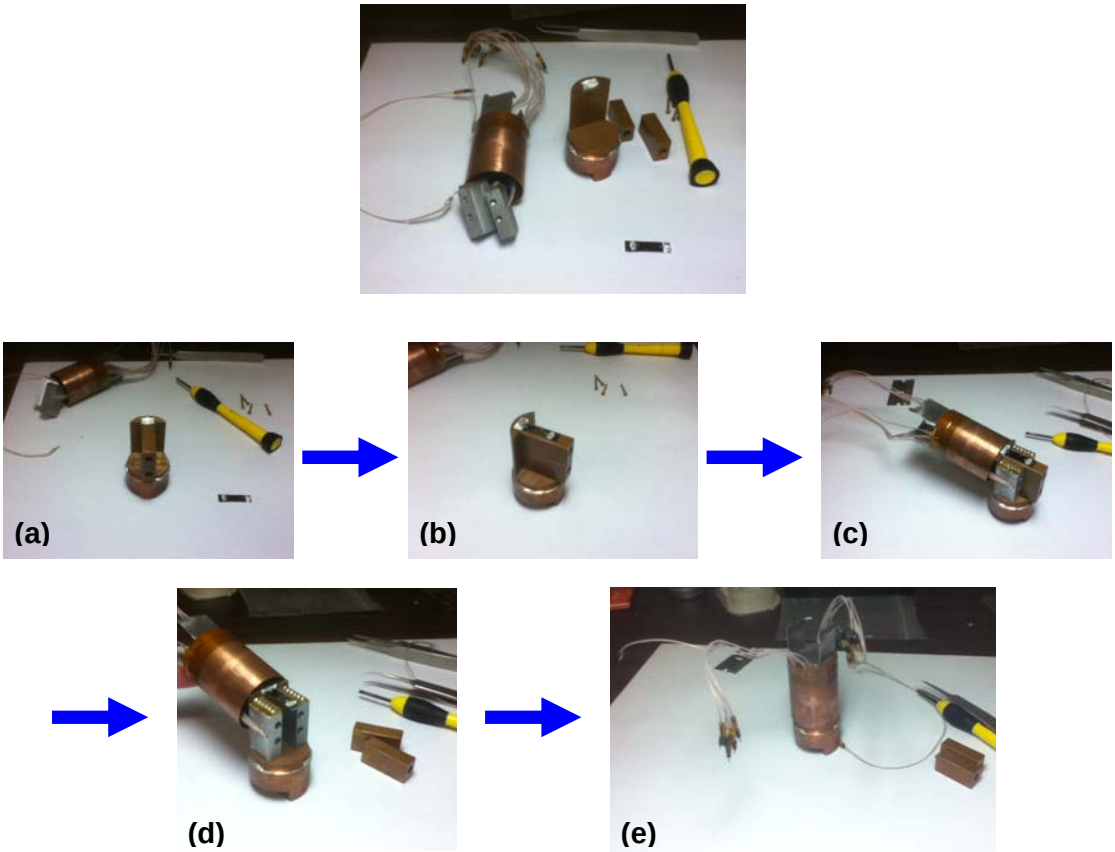

Fig 4.12 The processes of mounting our low temperature thermopower measurement setup.

4.2.4 Techniques for thermoelectric measurements

DC measurement: (utilized in graphene device)

The patterned electrodes of the graphene devices are usually in good electrical contact with graphene flake. The background DC voltage noise of two electrodes bridged by graphene is in the order of several 100 nV, while the thermo-voltage signal is in the order of μV. This level of noise ensures that DC measurement of thermal power of graphene.

Fig 4.13 is the raw data of the thermo-voltage of one of the graphene device (device #11) with device geometry similar to the one in Fig 4.7. The blue curve shows the applied heater current. Two different directions of the heater current is applied, however, the response of the thermo-voltage is exactly the same. This indicates that the voltage signal comes from the thermo-effect induced by the heater, not from the leakage of the heater voltage.

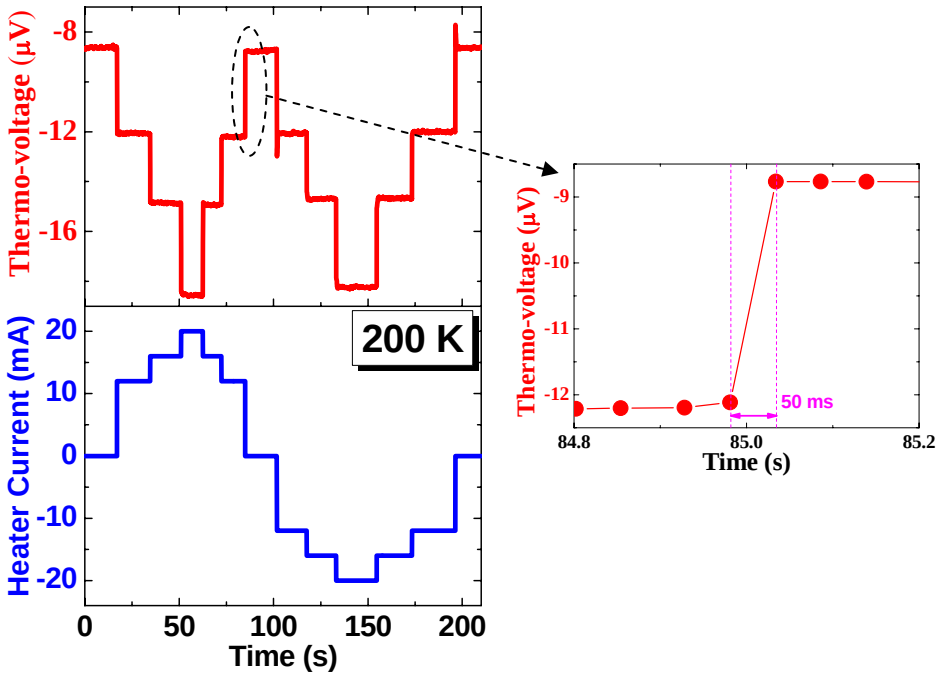

Fig 4.13 The thermo-voltage signal response upon changing of the thermopower. The response time is about 50ms.

The data in Fig 4.7 is the measurement at 200 K. At lower temperature (~10 K), the thermo-voltage will be smaller. Proper average processes need to be taken to extract out the signal. Fig 4.14 demonstrates the method we do the average. In the cryostat system, the electric signal of the device is taken out through many copper electric wires. These wires experience a large temperature gradient (from device temperature to room temperature) and contribute a background thermo-voltage. This is the reason that the open circuit signal of the device is not zero even the heater power is not applied. Because there are temperature fluctuations within the cryostat system, the open circuit voltage of the device tends to have small drift with respect to time. If the data taking time is too long, the background open circuit voltage drift will be counted in. The magnified graph in Fig 4.13 shows that

the response of the thermo-voltage to the heater power change is roughly 50 ms. Therefore, in our measurement, we average the data right before and after the heater is turned on/off (Fig 4.14). Thus, only the thermo-voltage response due to the sample heater is picked up. We call one heater on/off as one heater cycle and we normally take two heater cycles to get one thermo-voltage data point.

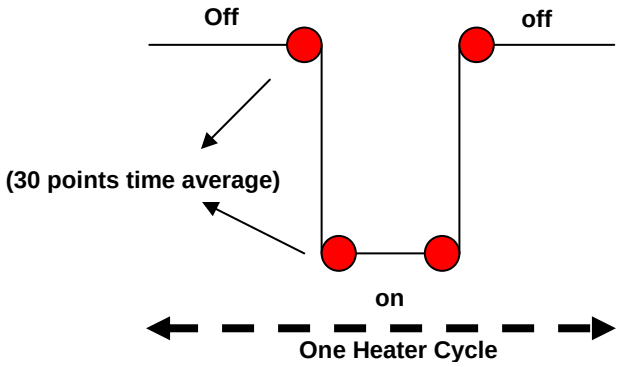

Fig 4.14 Our method of averaging sequences in the measurement of small signals of the graphene thermo-voltage.

The measurement of thermo-voltage is straight forward. The measurement of temperature gradient is more critical. As demonstrated in Fig 4.7, we measure the four terminal resistance change of two Cr/Au (7nm/100nm) metal wires (thermometer) to determine the temperature gradient. The temperature dependence of the resistance of the metal wires is shown in Fig 4.15. This data is from device #19. It behaves linearly and becomes flat at low temperature (< 10K).

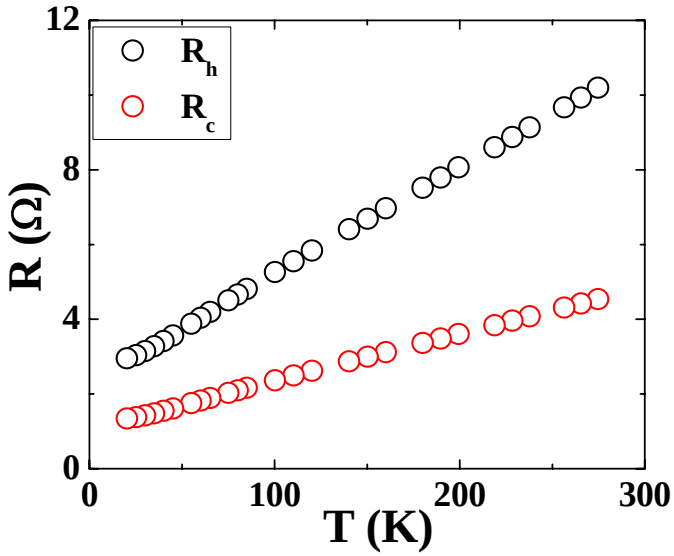

Fig 4.15 The temperature dependence of our metal thermometer wire.

Fig 4.16 demonstrates our method of thermopower measurement. The heater power is quickly raised up step by step for four consecutive steps. The resistances of the Cr/Au metal wires (thermometers) are measured simultaneously vs. the heater power. In the measurement, a constant current is passed through the thermometers, so the voltage in Fig 4.16 is directly proportional to the resistance. The time for this heater power ramping sequence needs to be short. We normally use 1 minute to finish one run. Four different runs are performed with a waiting time of 15 minutes between them. The heater is kept off during the waiting time in order to let the temperature of the device to relax to the value before applying the heater. From Fig 4.16 we can see that there are some fluctuations of the value of the thermometer resistance between each run. The curves of the thermopower, however obviously, shift down by a y-axis offset between each run, but their slopes are almost unchanged. This indicates a background voltage offset change, but it does not affect the relative thermo-voltage.

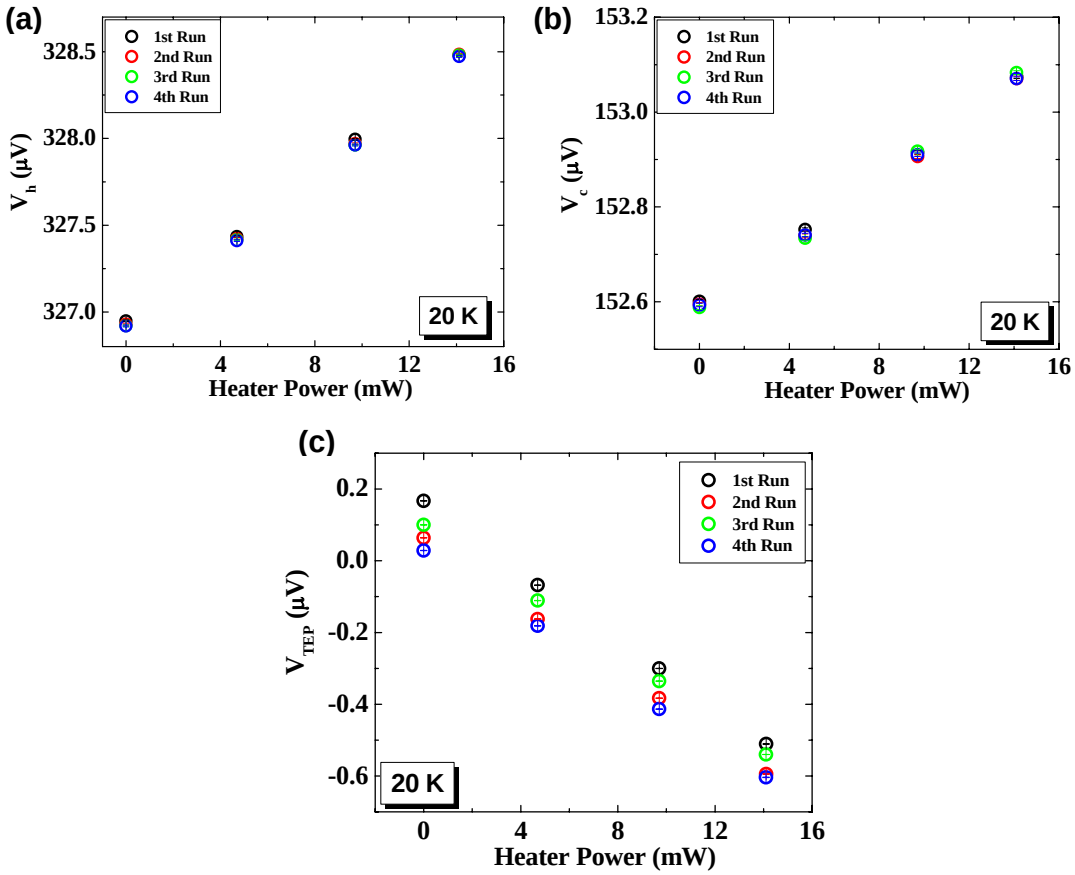

Fig 4.16 The method we used in extracting the Seebeck coefficient of graphene.

The fluctuation of the thermometer resistance and the background offset change of the thermo-voltage, although affect the absolute value; they do not affect the slope of these quantities vs. heater power. The slope of these curves actually tells us the response of the device to the heater. As long as the measurement is taken quickly enough (has to be longer than the response time of the thermopower to the heater Fig 4.13), the slope is reliable. From Fig 4.16, we can get the response of the two thermometer resistance to the heater power as dV_h/dP and dV_c/dP. We can also get the response of the thermo-voltage to the heater power as dV_{TEP}/dP. From Fig 4.15, we can get the

response of the thermometer resistance to the temperature as dV_h/dT and dV_c/dT. The response of the temperature raise of the thermometers to the heater power can be calculated as: $dT_h/dP = (dV_h/dP)/(dV_h/dT)$ and $dT_c/dP = (dV_c/dP)/(dV_c/dT)$. Then the response of the temperature difference to the heater power is calculated as: $d(\Delta T)/dP = dT_h/dP - dT_c/dP$. Thus, we have the response of the thermo-voltage to the heater power dV_{TEP}/dP and the response of the temperature difference to the heater power $d(\Delta T)/dP$. The Seebeck coefficient is simply $S_{xx} = [dV_{TEP}/dP]/[d(\Delta T)/dP]$. By using this method, we remove the effect of the unstable offset values.

AC measurement: (utilized in Bi_xTe_y nano-ribbon device)

If the background DC voltage noise is in the order of several μV, which is the case of Bi_xTe_y nano-ribbon device (Fig 4.10), the DC thermo-voltage signal will be covered by the noise and the DC measurement is not applicable. We attribute the large noise of the open circuit voltage to the high contact resistance between the metallic wire and the Bi_xTe_y nano-ribbon and perform the AC measurement to increase the signal from the noise.

In our measurement, a SR-830 lock-in amplifier is used. An AC voltage of 1.6 V amplitude at 2.971 Hz is applied through the heater on the device. From Fig 4.13, we can know that the response time of the thermo-voltage to a step jump of the heater power is at the level of 50 ms. In order to let the device thermo-voltage fully relaxed, the period of the AC voltage source needs to be large. However, it cannot be chosen arbitrarily large, because it will approach the DC limit and the lock-in can not extract the signal with too low frequency. After several tests, we choose the frequency to be around 3 Hz. Fig 4.17 demonstrates the heater voltage applied by the lock-in amplifier. The heater voltage can be written

as $V(t) = V_0 \sin(2\pi \cdot f \cdot t)$ (blue curve in Fig 4.17) and the heater power is $P_{heater}(t) \propto V^2(t) = V^2 \sin^2(2\pi \cdot f \cdot t) = \frac{V_0^2}{2}[1 - \cos(2\pi \cdot 2f \cdot t)]$ (red curve in Fig 4.17). The temperature difference and the thermo-voltage are then directly proportional to the heater power. Thus, a sine wave of the applied heater power will result in a thermo-voltage of cosine wave with twice of the frequency. In the measurement, we use the lock-in to lock the 2nd harmonic of the voltage input, while check the lock-in phase to see if the thermo-voltage signal has a π/2 phase shift relative to the applied heater voltage.

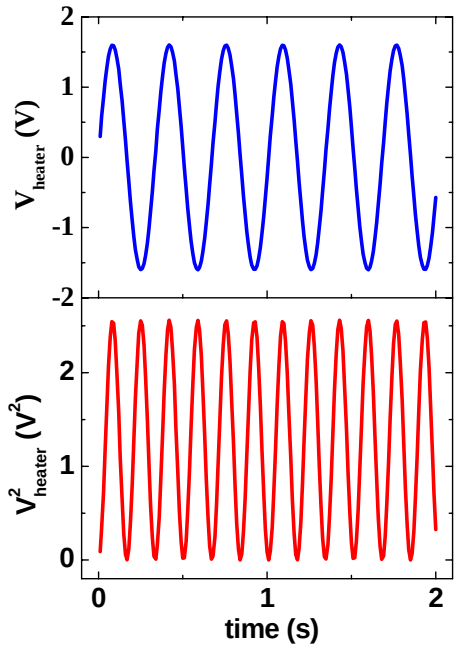

Fig 4.17 The simulated heater voltage and heater power in our AC measurement of thermopower.

Fig 4.18 demonstrates the AC thermo-voltage data of the device in Fig 4.10. The thermoelectric voltage is plotted vs. the applied heater voltage and heater power. A clear linear dependence of the thermo-voltage to the heater power can be seen, which indicates that the voltage signal is

thermo-voltage. The measurement of the thermometer resistance does not depend on the contact resistance. It is just the resistance of a metallic wire. The temperature difference can be determined by the similar DC measurement as discussed before.

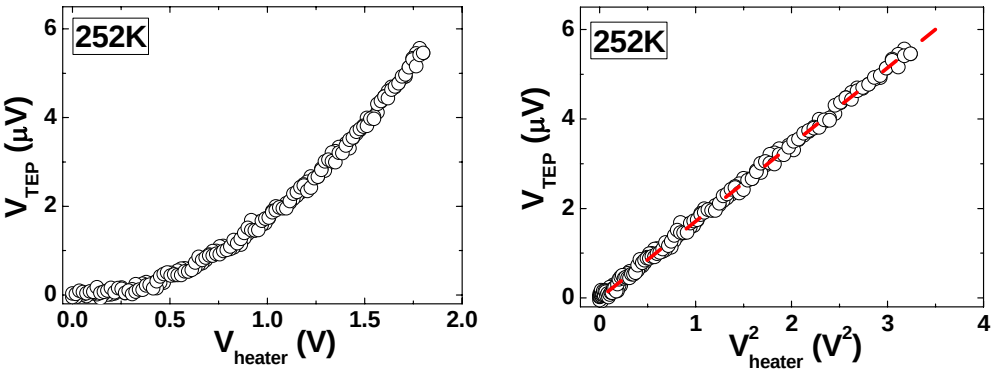

Fig 4.18 The AC measurement of the thermo-voltage. The signal is linear to the heater power.

4.2.5 Nernst signal under a magnetic field

The Nernst voltage can be measured in the similar way to the thermopower. Because the Nernst signal is contributed by the local temperature gradient at the position of the two transverse leads (Fig 4.19, which is the top view of Fig 4.7), which are very close to the heater, the temperature gradient of the Nernst signal may not be the same as the temperature gradient of the Seebeck signal. After we measured and calibrated the Seebeck coefficient of the device, we measure the thermo-voltage between one Nernst lead and the nearest thermometer. Then the temperature difference between the Nernst lead and the thermometer can be calculated. By dividing this temperature difference with the distance between the Nernst leads and the nearest thermometer, the temperature gradient over this small distance can be solved. We use this value as the temperature gradient at the Nernst leads.

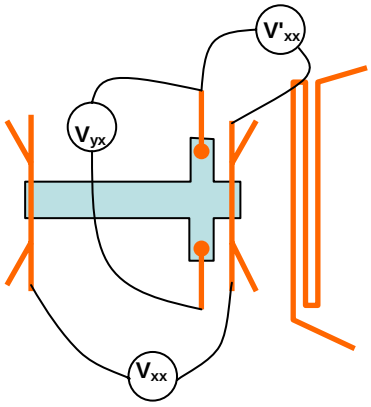

Fig 4.19 The schematic graph of how we determine the temperature gradient near the Nernst leads.

For the thermoelectric transport coefficients under magnetic field (Seebeck coefficient and Nernst coefficient), we can phenomenologically write equations as (similar as Eq 4.1):

$$\begin{aligned} j_x &= \sigma_{xx}\varepsilon_x + \sigma_{xy}\varepsilon_y - \alpha_{xx}\nabla_x T \\ j_y &= \sigma_{yx}\varepsilon_x + \sigma_{yy}\varepsilon_y - \alpha_{yx}\nabla_x T \end{aligned} \qquad \text{(Eq 4.4)}$$

, where

$$\alpha_{xx} = -\frac{\pi^2 k_B^2 T}{3e}\frac{\partial \sigma_{xx}}{\partial \varepsilon}\bigg|_{\varepsilon_F}$$
$$\alpha_{yx} = -\frac{\pi^2 k_B^2 T}{3e}\frac{\partial \sigma_{yx}}{\partial \varepsilon}\bigg|_{\varepsilon_F}$$

Here the electric field at both x-axis or y-axis directions affect the current at the other direction. We only apply a temperature gradient along the x-direction, so only $\nabla_x T$ is considered. At steady state, there is no net charge current flow, so we have $j_x = 0$ and $j_y = 0$. Because the Seebeck coefficient and Nernst coefficient are defined as:

$$S = \frac{E_x}{\nabla_x T}$$

$$\nu_N = -\frac{E_y}{\nabla_x T} \cdot \frac{1}{B}$$

(B is magnetic field)

We also have:

$$\sigma_{xx} = \frac{\rho_{xx}}{\rho_{xx}^2 + \rho_{xy}^2}$$

$$\sigma_{xy} = -\sigma_{yx} = -\frac{\rho_{xy}}{\rho_{xx}^2 + \rho_{xy}^2}$$

(Eq 4.5)

By solving Eq 4.4 we can get:

$$S = -\frac{\pi^2 k_B^2 T}{3e} \cdot \frac{\partial \ln \sqrt{\sigma_{xx}^2 + \sigma_{xy}^2}}{\partial \varepsilon_F}$$

$$\nu_N = -\frac{\pi^2 k_B^2 T}{3e} \cdot \frac{\partial \Theta_H}{\partial \varepsilon_F}$$

, where $\tan \Theta_H = \frac{\sigma_{xy}}{\sigma_{xx}}$ and Θ_H is the Hall angle.

Chapter 5 Anomalous thermoelectric transport of Dirac particles in graphene

The electrical transport in graphene is carried by Dirac fermions, which have demonstrated many exciting properties that cannot be observed in conventional condensed matter materials.[4-7,50,51,51] As equally fundamental as the electrical conductivity (Chapter 4), the thermoelectric coefficients in particular, involve the energy derivatives of the electrical transport counterparts such as the conductivity σ and the Hall angle Θ_H. The anomalies in the latter are very often amplified and cause markedly distinct features in the former near the Dirac point. Furthermore, in the regime where the Mott relation is applicable, the relationship between the measured electrical conductivity and the Seebeck coefficient reveals how the chemical potential depends on the gate voltage or carrier density, which is dictated by the energy dispersion. Therefore, the thermoelectric transport coefficients can offer unique information and are complimentary to the electrical transport coefficients.[50,52,53] In this chapter, we will demonstrate our experimental studies on the thermoelectric transport properties of Dirac fermions.

5.1 Modulation of the thermopower through electrostatic gate

The geometry for the gating is demonstrated in Fig 5.1. Because graphene only consists of a single layer of carbon atoms, this geometry of gate tuning can effectively tune the carrier density of the whole graphene flakes.

The data in Fig 5.1 comes from Device #14. Upon applying the gate voltage, the conductivity of the device undergoes a minimum, while the Hall resistance changes sign indicating a carrier type change at the Dirac point of graphene. If we calculate the 2D carrier density of the device v.s. gate voltage, we can see that it becomes linear in the region away from the Dirac point. The slope of the

linear curve gives a carrier density change per gate voltage of about 8.0×10^{10} cm^{-2} V^{-1}. This is in a good consistence to the value calculated from the capacitance of 300nm SiO_2 gate insulator as 7.2×10^{10} cm^{-2} V^{-1} (115 aF/μm^2).

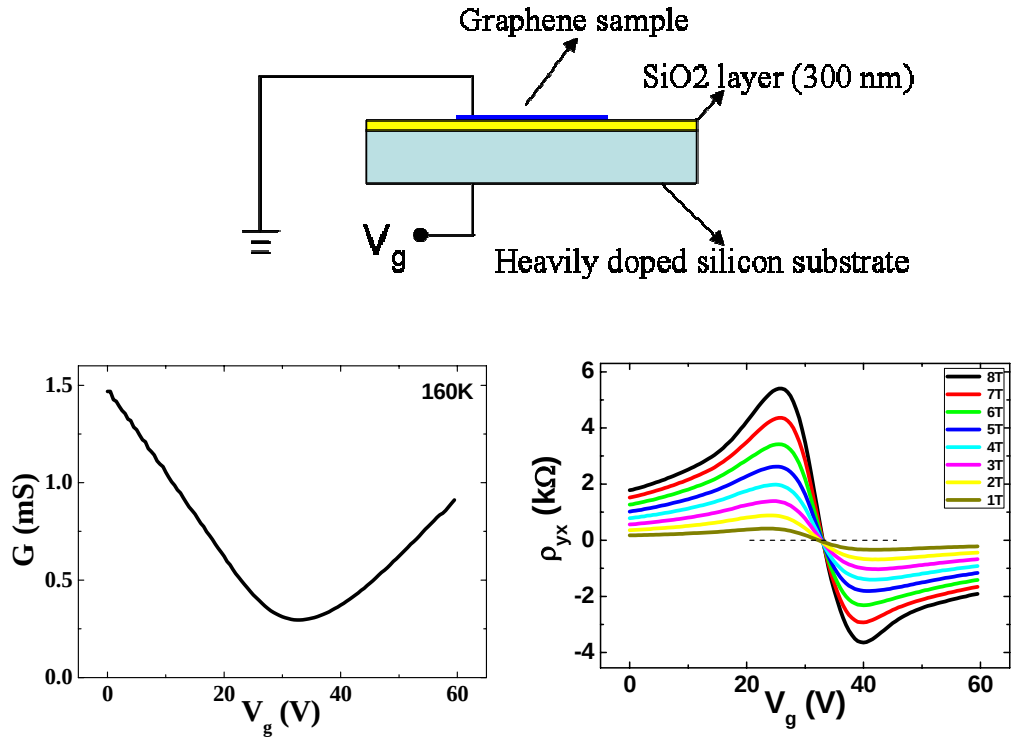

Fig 5.1 The gate tuning of graphene conductivity and Hall resistance. A clear minimum of the conductivity can be observed accompanied by the sign change of the Hall resistance. The top image demonstrates the geometry for electro static gate tuning.

The electric back gate acts like a parallel capacitor with graphene as one of its metal plates. The change of the voltage across the capacitor directly adds or removes electrons of the graphene flake, which causes a carrier density change of graphene.[4] The thermopower signal can also be tuned by this electron static gate, since it depends on the carrier density of the material. The details about measuring thermopower have already been discussed in section 4.2.4. Fig 5.3 shows the thermopower signal for

this device at 160K. It changes sign exactly at the Dirac point indicating a change of the carrier type of the graphene device.

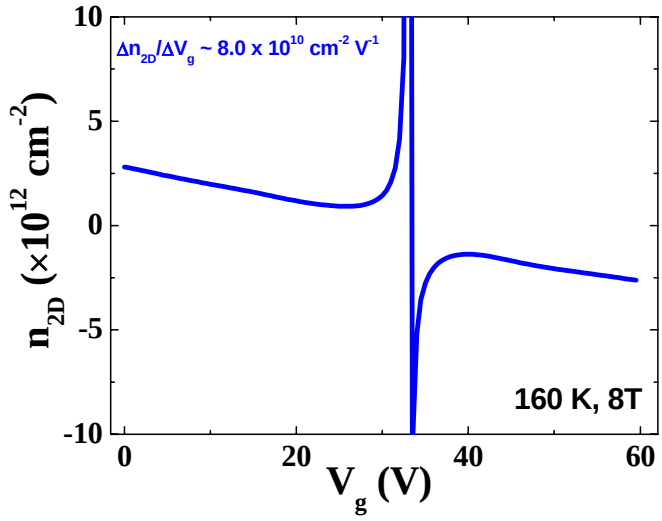

Fig 5.2 The carrier density v.s. gate voltage. The carrier density is calculated from the Hall resistance data. The slope of the carrier density change fits very well with the parallel capacitor model of the 300 nm SiO_2.

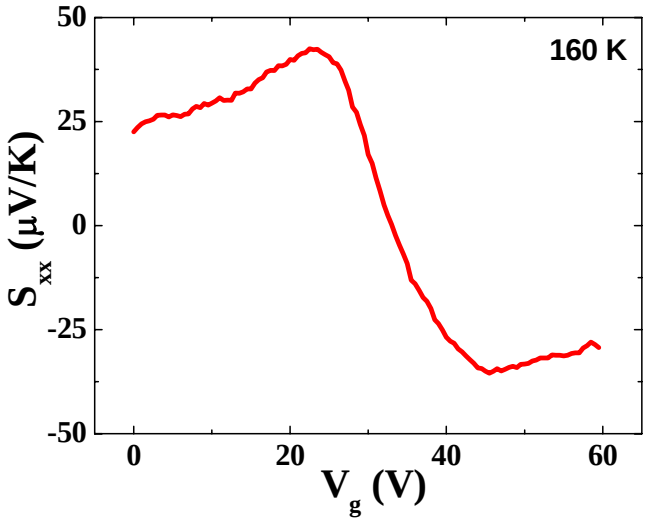

Fig 5.3 The sign change of the thermopower of the same graphene device as in Fig 5.1.

5.2 Diverging behavior of the thermopower vs. carrier density

Comparing the Hall resistance data in Fig 5.1 and the thermopower data in Fig 5.3, we can see similar behaviors. They both pass zero at the Dirac point and gradually decrease as the gate voltage becomes larger. For the Hall resistance, we always have the equation as $\rho_{yx} = R_H \cdot B = \frac{B}{e \cdot n_{2D}}$ (B is the magnitude of the magnetic field and e is the electron charge), which doe not depend on the dispersion relation of the band structure. However, this expression will give an infinite large Hall resistance at the Dirac point, because the carrier density is zero. Actual data shows that the Hall resistance starts to decrease in the region near the Dirac point and passes zero at the Dirac point. This behavior can only be understood by considering the conductions of both electron channel and hole channel in the region near the Dirac point, where the Hall coefficient have to be written as $R_H = \frac{n_h \mu_h^2 - n_e \mu_e^2}{e(n_h \mu_h + n_e \mu_e)^2}$. The parameters n_h and n_e are the carrier density of hole and electron. μ_h and μ_e are the mobility of hole and electron. Hence, the Hall coefficient will vanish when the electron density is equal to the hole density.

From another point of view, if we estimate the thermal energy $k_B T$ at 160K, it has a value of about 14 meV. Consider a pure graphene with linear dispersion relation as $E(\vec{k}) = \hbar v_F \mid \vec{k} \mid$ ($v_F \sim 1 \times 10^6$ m/s). The total 2D carrier density calculated from the Dirac point can be expressed as $n_{2D} = \frac{E^2}{\pi \hbar^2 v_F^2}$. In Fig 5.1, the transition region for the Hall resistance is about ± 7 V with respect to the Dirac point. Simple estimation will give that the energy scale of the transition region in pure graphene is ± 83 meV, which is much larger than the thermal energy $k_B T$. This estimation simply tells us that the mix of electron conduction and hole conduction in our graphene device can not come from the thermal

widening of the Fermi level. It has to come from the imperfectness of graphene near the Dirac point, which is related to the impurity density.

Similar condition happens for the thermopower. However, because thermopower is related to the energy derivative of the conductive, the dispersion relation of the energy band will enter and affect the dependence of the thermopower v.s. carrier density. Fig 5.4 shows thermo-voltage V_{th} as a function of V_g for three temperatures. This data is from Device #3, which shows the best electron-hole symmetry as well as a narrow transition region near the Dirac point. V_{th} undergoes a sign change at the Dirac point $V_g = V_D = 10$ V, indicating the carrier type changes from hole to electron as V_g - V_D is swept from negative to positive. V_{th} has a finite slope near V_D over a 20 V range in V_g which corresponds to ~ ±100 meV change in chemical potential μ measured from the Dirac point. This region coincides with the minimum in σ, where charged impurities modify the conductivity. As V_g is further away from V_D on both sides, the magnitude of V_{th} decreases, scaling approximately with $1/\sqrt{|V_g - V_D|}$ (dashed line in Fig 5.4(a)). This V_g dependence is more noticeable in the linear dependence of $1/V_{th}^2$ on V_g (Fig 5.4(b)). The solid lines are the power-law fits with exponent ~ 0.95 and cross zero in the vicinity of the Dirac point from both sides, indicating a diverging behavior of S_{xx}. Note that near the Dirac point, V_{th} crosses zero, and the $1/\sqrt{|V_g - V_D|}$ -dependence breaks down, as denoted by the hatched region. For comparison, the same V_{th} data is also plotted as $1/|V_{th}|$ *vs.* V_g in Fig 5.4(c) and the straight lines are drawn in the linear region. Clearly, the $1/V_{th}^2$ plot shows a better linear relationship with V_g over the whole range. In addition, $1/V_{th}^2$ extrapolates to zero at almost the same V_g for different temperatures, but $1/|V_{th}|$ does not.

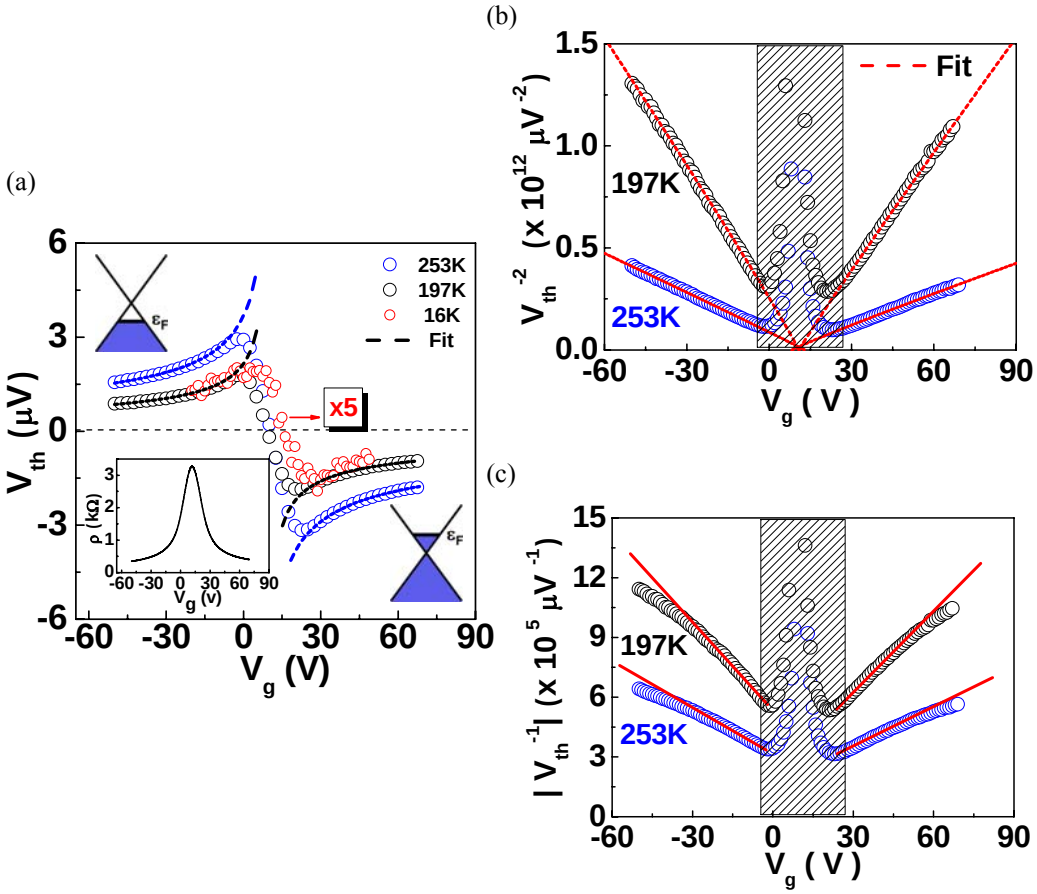

Fig 5.4 (a) V_{th} *vs.* V_g for three different temperatures. The 16K data (red circle) was multiplied by a factor of five. The dash lines are the fits described by $|S_{xx}| \sim 1/\sqrt{|V_g - V_D|}$. (b) $1 / V_{th}^2$ *vs.* V_g plot for the same data shown in (a). The shaded area is for $|V_g - V_D| < 10$ V. Red lines are the best power-law fits with exponent ~ 0.95. (c) $1 / |V_{th}|$ *vs.* V_g plot for the same data in (a). Red lines are straight lines as guides to the eye.

The fact that $|V_{th}|$ or $|S_{xx}|$ diverges as $1/\sqrt{|V_g - V_D|}$ is actually a direct manifestation of the linear dispersion of the Dirac particles in graphene. Let us assume $\sigma \sim |\mu|^{\alpha}$, which is sufficiently general to include both dirty ($\alpha \sim 2$) and clean ($\alpha \sim 1$) limits.[54,55] For degenerate electron systems, we

expect the Mott relation $S_{xx} = -\frac{\pi^2 k_B^2 T}{3e}\frac{\partial \ln\sigma(\mu)}{\partial\mu}$ to hold, yielding $S_{xx} \sim -\frac{1}{\mu}$ for highly doped regimes. On the other hand, for a 2D system with a linear dispersion relation, then we expect $\mu = \hbar v_F \sqrt{n_{2D}\pi} \propto \pm\sqrt{|V_g - V_D|}$, where the +(-) sign corresponds to the electron- (hole-) doped regime, and v_F is the Fermi velocity. Combining these relations, we have $S_{xx} \sim \frac{-\mathrm{sgn}(\mu)}{\sqrt{|V_g - V_D|}}$. This is in contrast to the ordinary 2D electron systems with a quadratic dispersion relation, in which $\mu \propto n_{2D}$, and hence $S_{xx} \sim \frac{-1}{V_g - V_D}$. From this diverging behavior of S_{xx}, we can conclude that the dispersion relation is linear rather than quadratic, as expected for Dirac particles. It is worth noting that the exponent α is absorbed in the pre-factor of S_{xx} and does not affect the functional dependence of S_{xx}, as is the case in σ. This makes the thermoelectric transport uniquely sensitive to the electronic band structure.

5.3 Temperature dependence of the thermopower

Not every device shows the electron-hole symmetry shown in Fig 5.4. Fig 5.5(a) displays S_{xx} *vs.* V_g of a different device with $V_D \sim 33$V for several values of T ranging from 11 to 255 K. Away from V_D on the hole side, S_{xx} decreases with decreasing V_g, similar to the behavior of the previous device. In contrast, S_{xx} stays flat on the electron side, indicating a strong electron-hole asymmetry as seen in σ by others.[54] Near V_D, we observe a broad transition region in S_{xx} connecting the electron- to hole-doped regimes. Furthermore, S_{xx} follows different T-dependence for different V_g (in Fig 5.5(b)). Near V_D, the magnitude of S_{xx} is close to zero. Away from V_D on the hole side, e.g. at V_g = 0 V or ~33 V left of V_D, S_{xx} is nearly a straight line for the whole temperature range. As V_g approaches V_D from the hole side, S_{xx} begins to deviate from the linear T-dependence at progressively lower temperatures. On the electron

side, however, even at V_g = 60 V (or ~30 V right of V_D), S_{xx} remains non-linear in T except at very low temperatures.

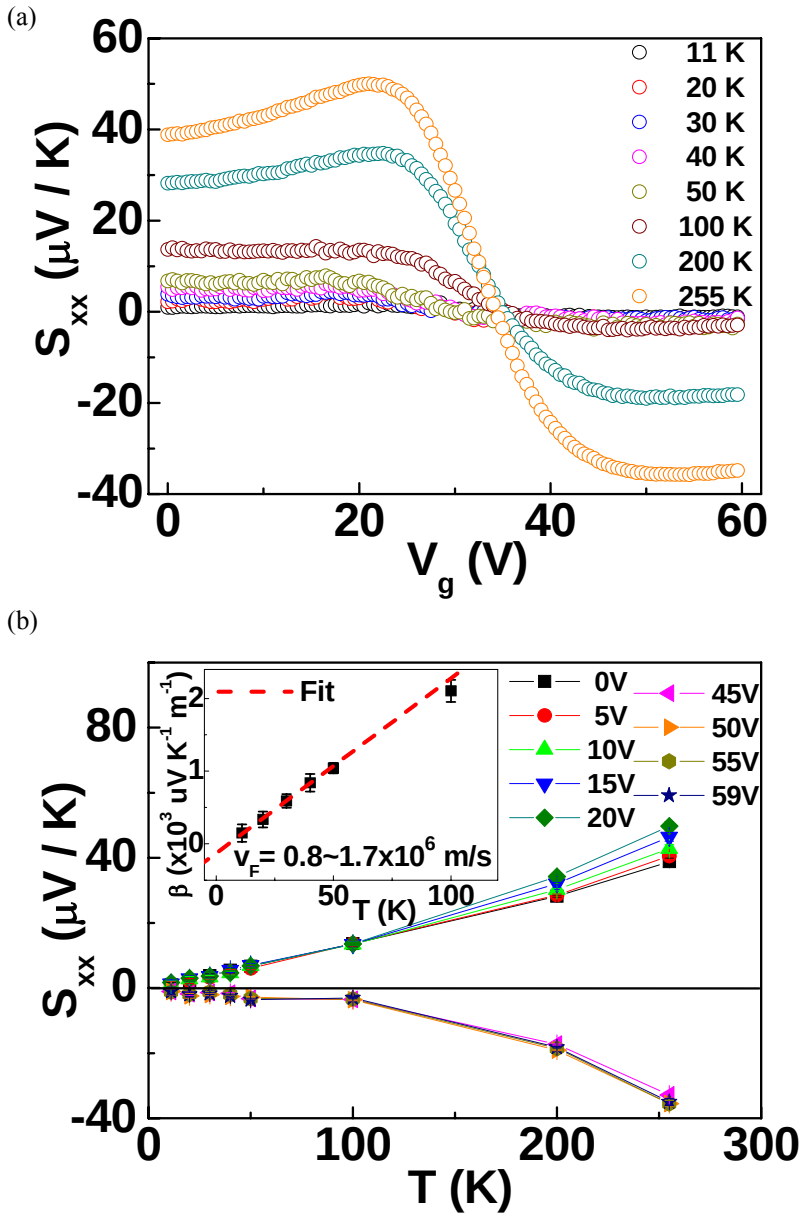

Fig 5.5 (a) V_g-dependence of longitudinal Seebeck coefficient S_{xx} at different temperatures (11K – 255K) and zero magnetic field. (b) T-dependence of S_{xx} at different gate-voltages. The inset is the T-dependence of $\beta = S_{xx}\sqrt{|n_{2D}|}$ at V_g=0 V for low temperatures. The slope of the linear fit is proportional to α / v_F.

The departure from the linear *T*-dependence is an indication of the potential breakdown of the Mott relation. For this device, when $|V_g - V_D|$ = 30 V, $|\mu|$ is about 160 meV measured from the Dirac point. It is reasonable to expect high-order corrections in the Sommerfeld expansion at relatively high temperature where the condition $|\mu| >> k_B T$ fails. For graphene, another relevant energy scale is the bandwidth γ of impurity states near the Dirac point. The Mott relation only holds if $\frac{\gamma}{k_B T} >> 1$, which ensures σ to be a slow-varying function of energy over this band of impurity states.[56] In the impurity scattering model, this band can be highly asymmetric due to the finite scattering potential. Here we attribute the departure from the linear *T*-dependence on the electron side to the asymmetric nature of the band of impurity states. For this reason we only focus on the relatively low-*T* region on the hole side where the Mott relation apparently holds. Since S_{xx} is proportional to αT, and inversely proportional to μ or $v_F\sqrt{|n_{2D}|}$, we plot $S_{xx}\cdot\sqrt{|n_{2D}|}$ (called β) vs. T in the inset of Fig 5.5(b). Extracted from the slope, v_F ranges from 0.8 to 1.6×10^6 m/s depending on the value of α (from 1 to 2), which is in good agreement with the values obtained by others.[57,58] In relating V_g to n_{2D} for above estimations, we use $n_{2D} = \frac{C_g V_g}{e} + \bar{n} = \frac{C_g}{e}\left(V_g - V_D\right)$, where C_g is the capacitance per unit area and $\bar{n}$ is the induced density by charged impurities at the Dirac point. A value of C_g = 103 aF/μm^2 is determined from our Hall data.

In Fig 5.6, similar temperature dependence data is repeated. This set of data is from Device #19. The Dirac point of this device is located very near to the zero gate voltage point. The gate dependence of the thermopower shows much clearer divergent behavior at the hole side of the data. However, at the electron side, a constant shift of the thermopower value exists in large positive gate voltage range,

which shows strong electron-hole asymmetry. The reason of this electron-hole asymmetry still needs further investigations.

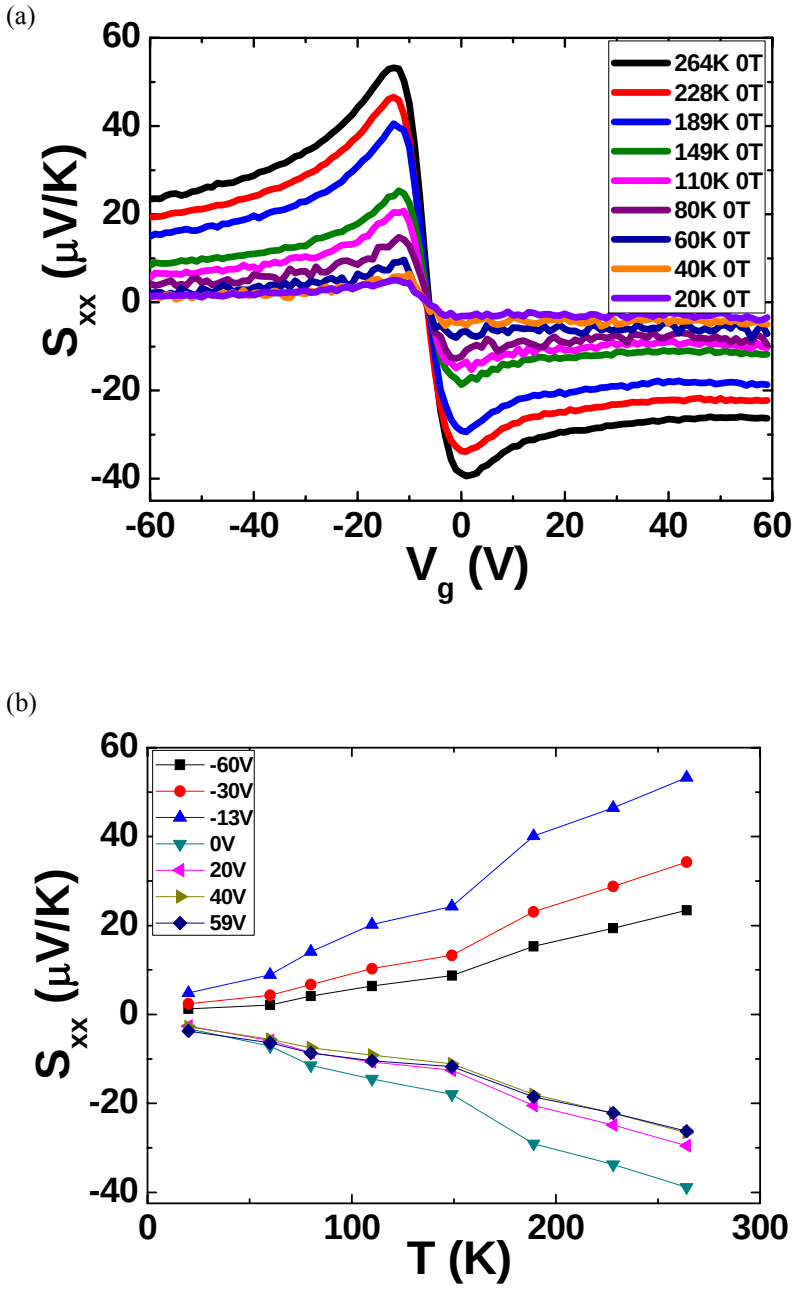

Fig 5.6 The temperature and gate dependence of the thermopower in Device #19. The gate dependence show more obvious divergent behavior.

5.4 Thermopower and Nernst signal in the quantum Hall regime

5.4.1 The effect of the Landau Level

One signature of the existence of massless Dirac fermion in graphene is the anomalous integer quantum Hall effect. Due to the relativistic nature, the energy of each Landau level in the quantum Hall regime can be written as $E_n = \sqrt{2e\hbar v_F^2 \mid n \mid B}$ with the Landau level index n (n = 0, 1, 2…). The quantized quantum Hall conductance can be expressed as $\sigma_{xy} = 2(2n+1)\frac{e^2}{h}$. At the zero filling n = 0, there still exist edge channels carried by the electron-hole pair near the Dirac point and contribute $2\frac{e^2}{h}$ to the quantum conductance.[5,6,51]

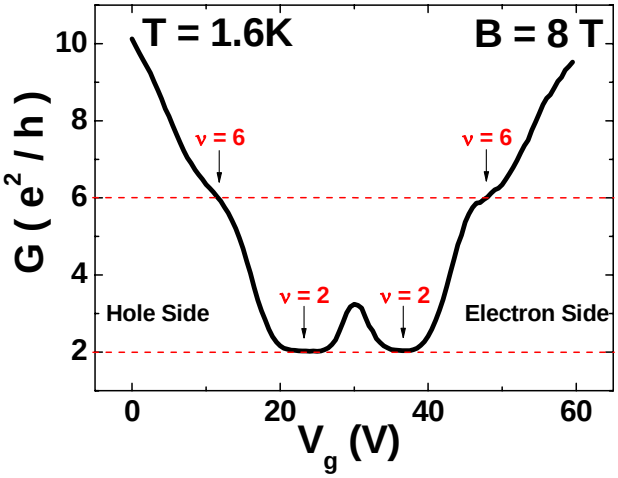

Fig 5.7 The two terminal resistance of the graphene device in quantum Hall regime. Plateau features develops exactly at each Landau level with determined filling factor.

Fig 5.7 demonstrates the gate dependence of the two terminal resistance of Device #14 under 8T perpendicular magnetic field. When the Fermi level is tuned in the region between two adjacent Landau levels, the conduction of the sample is carried by the edge channels and the transport is ballistic

like. The longitudinal resistivity ρ_{xx} will be zero, while the transverse resistivity ρ_{xy} provides a plateau. The two-terminal resistance directly measures the ballistic conductance of the edge channels, which has the same value as the Hall conductance in this region. We can clearly see the plateau value in Fig 5.7. If we scale it to the quantum conductance $\frac{e^2}{h}$, the filling sequence $\nu = 2$ and $\nu = 6$ exactly demonstrate the filling of the massless Dirac fermions.

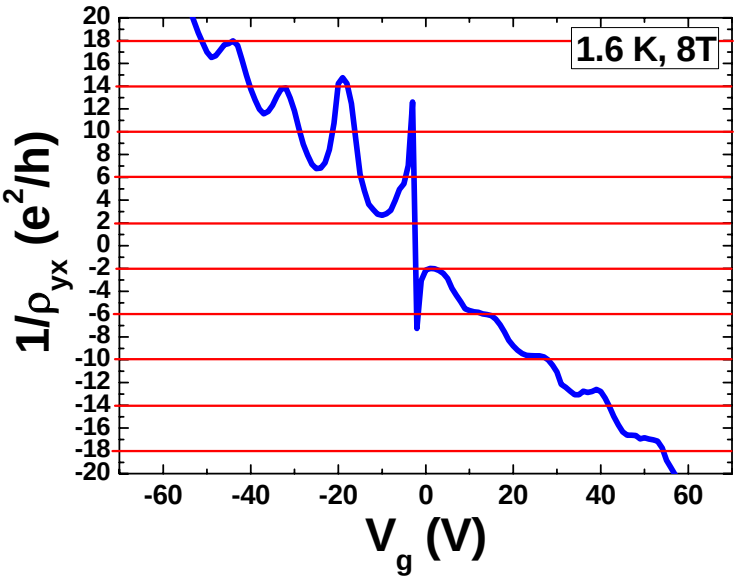

Fig 5.8 The Hall conductivity $\sigma_{xy} \sim 1/\rho_{yx}$ for Device #19. The Laudau level develops better at the electron side of this device.

Fig 5.8 demonstrates the Hall conductance of another sample (Device#19). From Eq 4.5, we can see that the Hall conductivity can be expressed as $\sigma_{xy} = -\frac{\rho_{xy}}{\rho_{xx}^2 + \rho_{xy}^2} = -\frac{1}{\rho_{xy}}$ exactly at each plateau value because of the vanishing ρ_{xx}. In this device, the Landau level develops better in the electron side.

In this quantum Hall regime, we also observe oscillations in S_{xx} (Fig 5.9(a) and (b)) that are reminiscent of the Shubnikov-de Hass oscillations in ρ_{xx}, and the side peaks and dips in S_{xy} that correlate with the oscillatory structures in S_{xx}. At T = 11 K, S_{xx} shows peaks (dips) as μ is inside the broadened Landau levels (LL) on the hole (electron) side. These peaks (dips) correspond to the LL indices n = 1 and n = 2 for holes (electrons). S_{xy} also changes sign at these fillings. It is also worth noting that S_{xx} crosses zero at the Dirac point (in the lowest LL), accompanied by an additional small dip (peak) on the hole (electron) side. In conventional 2D electron systems, the observed S_{xx} peaks at the LL's are consistent with the calculations in the integer quantum Hall regime. In graphene samples, the n =1 and n =2 peaks in S_{xx} on both electron and hole sides are also expected. However, we do not observe vanishing S_{xx} as μ is located between the two adjacent LL's. The non-vanishing S_{xx} was previously attributed to the activated behavior in ordinary 2D electron systems. In our samples, the relatively large magnitude of S_{xx} between the LL's may be caused by the broadened LL's due to disorders. We expect to see $S_{xx} \rightarrow 0$ at low temperatures and the predicted activated behavior at high temperatures in cleaner samples.

As the temperature increases, the oscillations in S_{xx} and S_{xy} become weaker, although the overall magnitude of both S_{xx} and the central peak in S_{xy} increases (Fig. 5.9(b)). As discussed earlier, the characteristic width of the Nernst peak is primarily determined by γ which is greater than k_BT. The Nernst width remains nearly unchanged as a consequence.

A more systematic data of how S_{xx} and S_{xy} vary vs. magnetic field and gate voltage is demonstrated in Fig 5.10. This data is from Device #19. Similar effects are observed in this device.

(a)

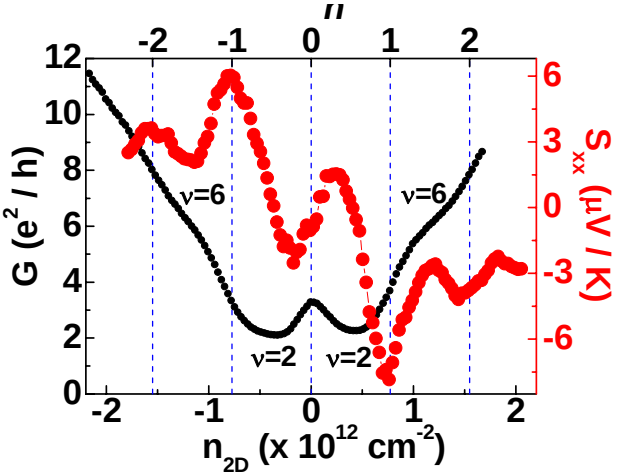

(b)

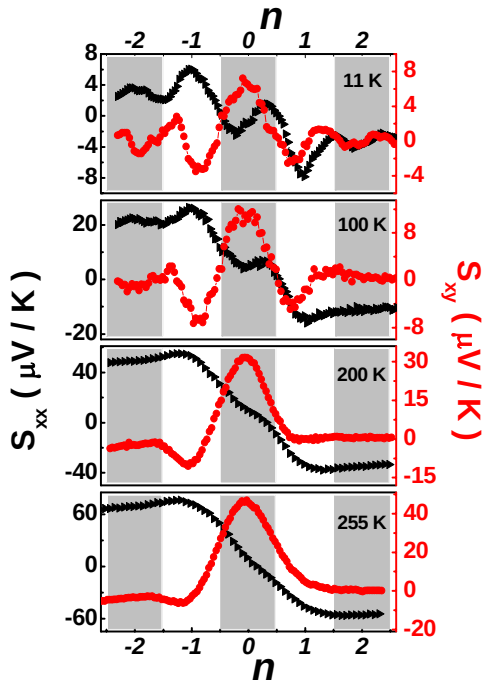

Fig 5.9 (a) Two-terminal conductance G and thermopower S_{xx} vs. carrier density n_{2D} at T = 11 K and $\boldsymbol{B}$ = 8 T. The corresponding Landau level index n is shown on the top axis. (b) S_{xx} (black triangle) and S_{xy} (red circle) *vs.* Landau level index n for four different temperatures at $\boldsymbol{B}$ = 8 T.

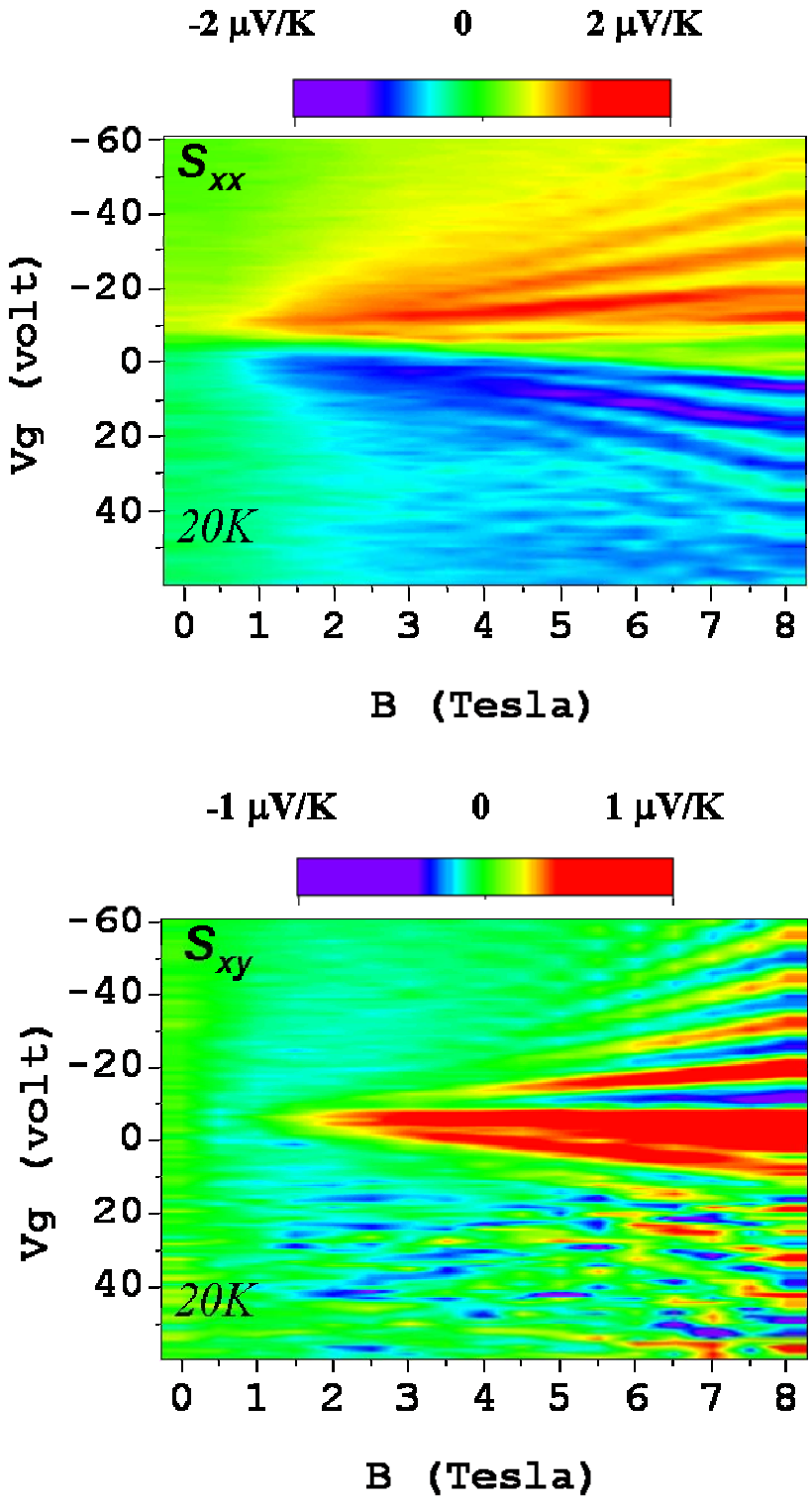

Fig 5.10 2D density plot of the S_{xx} and S_{xy} v.s. magnetic field and gate voltage in Device #19.

5.4.2 The Nernst peak at low carrier density

In a magnetic field, due to temperature gradient, the diffusing carriers experience the Lorentz force, resulting in a non-zero transverse voltage V_y. The transverse effect or the Nernst effect is measured by $S_{xy} = -\frac{E_y}{|\nabla T|} = \frac{\Delta V_y}{\Delta T_x}$. In non-magnetic metals, S_{xy} is negligibly small (~10 nV/K per tesla).[59,60] In ferromagnets, spin-orbit coupling can lead to a large spontaneous Nernst signal.[61,62] Here we observe an exceedingly large Nernst peak (~ 50 μV/K at 8 T) at the Dirac point (Fig 5.11(a) in Device #14), and we attribute it to the unique band structure of graphene. In classical transport, the Mott relation takes the following form:[50,63] $S_{xy} = -\frac{\pi^2}{3}\frac{k_B^2 T}{e}\left(\frac{\partial \Theta_H}{\partial \varepsilon}\right)_\mu = \frac{\pi^2 k_B^2 TB}{3}\frac{\partial}{\partial \mu}\left(\frac{\tau}{m^*}\mathrm{sgn}(\mu)\right)$. S_{xy} is directly proportional to the energy derivative of the Hall angle Θ_H or inversely proportional to the cyclotron mass m^*. For massless particles, the vanishing cyclotron mass can indeed lead to a diverging behavior in S_{xy}. In graphene devices, however, the anomaly is diminished by the impurity states near the Dirac point. Recall that the Mott relation breaks down in this region. Here we estimate the magnitude of S_{xy} at the Dirac point both from Θ_H outside this region where the Mott relation holds and from γ. Since we have $\Theta_H = -\mu_c \cdot B \cdot \mathrm{sgn}(\mu)$ (μ_c: carrier mobility), we obtain $\Delta\Theta_H \sim 2.2$ with an 8T magnetic field at 255 K. This change in Θ_H occurs over γ ~204 meV as estimated from the width of the conductance minimum, yielding S_{xy} ~ 68 μV/K. This is in very good agreement with the experimentally observed peak value (~ 50 μV/K). Additionally, Θ_H is directly proportional to $\boldsymbol{B}$, which indicates a linear $\boldsymbol{B}$-field dependence in S_{xy}, with an estimated slope of ~5.4 μV/K • T at 160 K. Indeed, the linear $\boldsymbol{B}$-dependence of S_{xy} is observed (Fig 5.11(a)), and the slope of the straight line is ~ 6 μV/K • T.

Similar to S_{xx} whose diverging behavior is greatly modified by the disorders, the anomaly in S_{xy} depends on the carrier mobility as well as γ. We expect to see more pronounced anomalous behavior in both S_{xx} and S_{xy} in cleaner samples.

(a) (b)

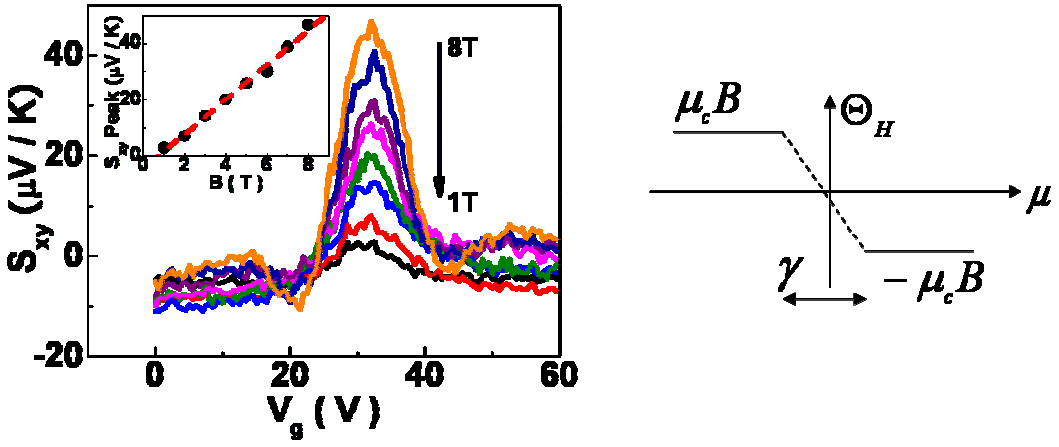

Fig 5.11 (a) The V_g-dependence of Nernst signal S_{xy} at 160 K with different magnetic fields (1 – 8 T). Inset: B-dependence of S_{xy} at $V_g = V_D$, and the red line is a linear fit. (b) The schematic graph of the sign change of the Hall angle at the Dirac point, which is related to the magnitude of the Nernst peak at the Dirac point.

Chapter 6 Conclusions

In conclusion, during my Ph.D. work I have studied the transport properties of two novel materials: the electrical transport of topological insulator-Bi_2Se_3 and the thermoelectric transport of graphene.

In our work of topological insulators, we have uncovered high-mobility states in the band gap of Bi_2Se_3 thin devices by systematically controlling the chemical potential via post-fabrication electron beam irradiation and electrostatic gating. We have designed a unique lithography-free fabrication technique to maintain the material properties in Bi_2Se_3 thin flakes. The high-mobility along with the characteristic WAL feature is attributed to the transport of the massless Dirac states in the band gap. We have also observed a signature of the Shubnikov-de Haas oscillations which result in a very high transport mobility. Our work paves the way of further studies and applications of the topological non-trivial surface states.

In our work on graphene thermoelectrics, the diverging behavior ($|S_{xx}| \sim 1/\sqrt{|n_{2D}|}$) of the Seebeck coefficient along with the exceedingly large Nernst peak at the Dirac point is characteristic of the massless particles in graphene. With disorders, these generic anomalies are somewhat masked near the Dirac point. However, the diverging behavior can be retrieved from those quantities as the chemical potential approaches the Dirac point. In higher mobility graphene samples, the anomalies are expected to be more drastically pronounced.

The structure and the symmetries of the condensed matter provide us enormous ways to create novel materials with novel properties. It is this process of discovery and study that revolutionize people's understanding of the surrounding world. Just like the discovery of new elements and the

understanding of the period table, the discovery and understanding of novel materials will lead us to a new era of human history.

References:

1 Bernevig, B. A., Hughes, T. L. & Zhang, S. C. Quantum spin Hall effect and topological phase transition in HgTe quantum wells. *Science* **314**, 1757-1761 (2006).

2 Kane, C. L. & Mele, E. J. Z(2) topological order and the quantum spin Hall effect. *Phys Rev Lett* **95**, 146802 (2005).

3 Kane, C. L. & Mele, E. J. Z(2) topological order and the quantum spin Hall effect. *Phys Rev Lett* **95**, 146802 (2005).

4 Novoselov, K. S. *et al.* Electric field effect in atomically thin carbon films. *Science* **306**, 666-669 (2004).

5 Novoselov, K. S. *et al.* Two-dimensional gas of massless Dirac fermions in graphene. *Nature* **438**, 197-200 (2005).

6 Zhang, Y. B., Tan, Y. W., Stormer, H. L. & Kim, P. Experimental observation of the quantum Hall effect and Berry's phase in graphene. *Nature* **438**, 201-204 (2005).

7 Castro Neto, A. H., Guinea, F., Peres, N. M. R., Novoselov, K. S. & Geim, A. K. The electronic properties of graphene. *Rev Mod Phys* **81**, 109-162 (2009).

8 Qi, X. L., Hughes, T. L. & Zhang, S. C. Topological field theory of time-reversal invariant insulators. *Phys Rev B* **78**, 195424 (2008).

9 Qi, X. L. & Zhang, S. C. The quantum spin Hall effect and topological insulators. *Phys Today* **63**, 33-38 (2010).

10 Klitzing, K. v., Dorda, G. & Pepper, M. New Method for High-Accuracy Determination of the Fine-Structure Constant Based on Quantized Hall Resistance. *Phys Rev Lett* **45**, 494 (1980).

11 Konig, M. *et al.* Quantum spin hall insulator state in HgTe quantum wells. *Science* **318**, 766-770 (2007).

12 Fu, L., Kane, C. L. & Mele, E. J. Topological insulators in three dimensions. *Phys Rev Lett* **98**, 106803 (2007).

13 Zhang, H. J. *et al.* Topological insulators in Bi_2Se_3, Bi_2Te_3 and Sb_2Te_3 with a single Dirac cone on the surface. *Nat Phys* **5**, 438-442 (2009).

14 Hsieh, D. *et al.* A topological Dirac insulator in a quantum spin Hall phase. *Nature* **452**, 970-U975 (2008).

15 Chen, Y. L. *et al.* Experimental Realization of a Three-Dimensional Topological Insulator, Bi_2Te_3. *Science* **325**, 178-181 (2009).

16 Zhang, T. *et al.* Experimental Demonstration of Topological Surface States Protected by Time-Reversal Symmetry. *Phys Rev Lett* **103**, 266803 (2009).

17 Roushan, P. *et al.* Topological surface states protected from backscattering by chiral spin texture. *Nature* **460**, 1106-U1164 (2009).

18 Qu, D. X., Hor, Y. S., Xiong, J., Cava, R. J. & Ong, N. P. Quantum Oscillations and Hall Anomaly of Surface States in the Topological Insulator Bi_2Te_3. *Science* **329**, 821-824 (2010).

19 Steinberg, H., Gardner, D. R., Lee, Y. S. & Jarillo-Herrero, P. Surface State Transport and Ambipolar Electric Field Effect in Bi_2Se_3 Nanodevices. *Nano Lett* **10**, 5032-5036 (2010).

20 Analytis, J. G. *et al.* Bulk Fermi surface coexistence with Dirac surface state in Bi_2Se_3: A comparison of photoemission and Shubnikov-de Haas measurements. *Phys Rev B* **81**, 205407 (2010).

21 Analytis, J. G. *et al.* Two-dimensional surface state in the quantum limit of a topological insulator. *Nat Phys* **6**, 960-964 (2010).

22 Checkelsky, J. G. *et al.* Quantum Interference in Macroscopic Crystals of Nonmetallic Bi_2Se_3. *Phys Rev Lett* **103**, 246601 (2009).

23 Chen, J. *et al.* Gate-Voltage Control of Chemical Potential and Weak Antilocalization in Bi_2Se_3. *Phys Rev Lett* **105**, 176602 (2010).

24 Peng, H. L. *et al.* Aharonov-Bohm interference in topological insulator nanoribbons. *Nat Mater* **9**, 225-229 (2010).

25 Xiu, F. X. *et al.* Manipulating surface states in topological insulator nanoribbons. *Nat Nanotechnol* **6**, 216-221 (2011).

26 Wallace, P. R. The Band Theory of Graphite. *Phys Rev* **71**, 622 (1947).

27 Katsnelson, M. I., Novoselov, K. S. & Geim, A. K. Chiral tunnelling and the Klein paradox in graphene. *Nat Phys* **2**, 620-625 (2006).

28 Young, A. F. & Kim, P. Quantum interference and Klein tunnelling in graphene heterojunctions. *Nat Phys* **5**, 222-226 (2009).

29 Hor, Y. S. *et al.* p-type Bi_2Se_3 for topological insulator and low-temperature thermoelectric applications. *Phys Rev B* **79**, 195208 (2009).

30 Teweldebrhan, D., Goyal, V., Rahman, M. & Balandin, A. A. Atomically-thin crystalline films and ribbons of bismuth telluride. *Appl Phys Lett* **96**, 053107 (2010).

31 Teweldebrhan, D., Goyal, V. & Balandin, A. A. Exfoliation and Characterization of Bismuth Telluride Atomic Quintuples and Quasi-Two-Dimensional Crystals. *Nano Lett* **10**, 1209-1218 (2010).

32 Wang, Z. Y. *et al.* Tuning carrier type and density in Bi_2Se_3 by Ca-doping. *Appl Phys Lett* **97**, 042112 (2010).

33 Greanya, V. A. *et al.* Determination of the valence band dispersions for Bi_2Se_3 using angle resolved photoemission. *J Appl Phys* **92**, 6658-6661 (2002).

34 Larson, P. *et al.* Electronic structure of Bi_2X_3 (X=S, Se, T) compounds: Comparison of theoretical calculations with photoemission studies. *Phys Rev B* **65**, 085108 (2002).

35 Hsieh, D. *et al.* A tunable topological insulator in the spin helical Dirac transport regime. *Nature* **460**, 1101-U1159 (2009).

36 Peterson, P. A., Radzimski, Z. J., Schwalm, S. A. & Russell, P. E. Low-Voltage Electron-Beam Lithography. *J Vac Sci Technol B* **10**, 3088-3093 (1992).

37 Pauw, v. d. A Method of Measuring the Resistivity and Hall Coefficient on Lamellae of Arbitrary Shape. *Philips Technical Review* **20**, 220 (1958).

38 Bianchi, M. *et al.* Coexistence of the topological state and a two-dimensional electron gas on the surface of Bi2Se3. *Nat Commun* **1**, 128 (2010).

39 Sacepe, B. *et al.* Gate-tuned normal and superconducting transport at the surface of a topological insulator. *arXiv:1101.2352* (2011).

40 Hikami, S., Larkin, A. I. & Nagaoka, Y. Spin-Orbit Interaction and Magnetoresistance in the 2 Dimensional Random System. *Prog Theor Phys* **63**, 707-710 (1980).

41 Checkelsky, J. G., Hor, Y. S., Cava, R. J. & Ong, N. P. Surface state conduction observed in voltage-tuned crystals of the topological insulator Bi_2Se_3. *arXiv:1003.3883* (2010).

42 He, H. T. *et al.* Impurity Effect on Weak Antilocalization in the Topological Insulator Bi_2Te_3. *Phys Rev Lett* **106**, 166805 (2011).

43 Rockwood, A. L. Relationship of Thermoelectricity to Electronic Entropy. *Phys Rev A* **30**, 2843-2844 (1984).

44 Tieke, B., Fletcher, R., Zeitler, U., Henini, M. & Maan, J. C. Thermopower measurements of the coupling of phonons to electrons and composite fermions. *Phys Rev B* **58**, 2017-2025 (1998).

45 Small, J. P. & Kim, P. Thermopower measurement of individual single walled carbon nanotubes. *Microscale Therm Eng* **8**, 1-5 (2004).

46 Small, J. P., Perez, K. M. & Kim, P. Modulation of thermoelectric power of individual carbon nanotubes. *Phys Rev Lett* **91**, 256801 (2003).

47 Small, J. P., Shi, L. & Kim, P. Mesoscopic thermal and thermoelectric measurements of individual carbon nanotubes. *Solid State Commun* **127**, 181-186 (2003).

48 Seol, J. H., Moore, A. L., Shi, L., Jo, I. & Yao, Z. Thermal Conductivity Measurement of Graphene Exfoliated on Silicon Dioxide. *J Heat Trans-T Asme* **133**, 022403 (2011).

49 Seol, J. H. *et al.* Two-Dimensional Phonon Transport in Supported Graphene. *Science* **328**, 213-216 (2010).

50 Gusynin, V. P. & Sharapov, S. G. Transport of Dirac quasiparticles in graphene: Hall and optical conductivities. *Phys Rev B* **73**, 245411 (2006).

51 Gusynin, V. P. & Sharapov, S. G. Unconventional integer quantum Hall effect in graphene. *Phys Rev Lett* **95**, 146801 (2005).

52 Dora, B. & Thalmeier, P. Magnetotransport and thermoelectricity in Landau-quantized disordered graphene. *Phys Rev B* **76**, 035402 (2007).

53 Peres, N. M. R., dos Santos, J. M. B. L. & Stauber, T. Phenomenological study of the electronic transport coefficients of graphene. *Phys Rev B* **76**, 073412 (2007).

54 Tan, Y. W. *et al.* Measurement of scattering rate and minimum conductivity in graphene. *Phys Rev Lett* **99**, 246803 (2007).

55 Bolotin, K. I., Sikes, K. J., Hone, J., Stormer, H. L. & Kim, P. Temperature-dependent transport in suspended graphene. *Phys Rev Lett* **101**, 096802 (2008).

56 Lofwander, T. & Fogelstrom, M. Impurity scattering and Mott's formula in graphene. *Phys Rev B* **76**, 193401 (2007).

57 Jiang, Z. *et al.* Infrared spectroscopy of Landau levels of graphene. *Phys Rev Lett* **98**, 197403 (2007).

58 Li, Z. Q. *et al.* Dirac charge dynamics in graphene by infrared spectroscopy. *Nat Phys* **4**, 532-535 (2008).

59 Clayhold, J. A., Linnen, A. W., Chen, F. & Chu, C. W. Normal-State Nernst Effect in a $Tl_2Ba_2CaCu_2O_{8+\delta}$ Epitaxial Film. *Phys Rev B* **50**, 4252-4255 (1994).

60 Xu, Z. A., Ong, N. P., Wang, Y., Kakeshita, T. & Uchida, S. Vortex-like excitations and the onset of superconducting phase fluctuation in underdoped $La_{2-x}Sr_xCuO_4$. *Nature* **406**, 486-488 (2000).

61 Lee, W. L., Watauchi, S., Miller, V. L., Cava, R. J. & Ong, N. P. Anomalous hall heat current and nernst effect in the $CuCr_2Se_{4-x}Br_x$ ferromagnet. *Phys Rev Lett* **93**, 226601 (2004).

62 Pu, Y., Chiba, D., Matsukura, F., Ohno, H. & Shi, J. Mott relation for anomalous Hall and Nernst effects in $Ga_{1-x}Mn_xAs$ ferromagnetic semiconductors. *Phys Rev Lett* **101**, 117208 (2008).

63 Sondheimer, E. H. The Theory of the Galvanomagnetic and Thermomagnetic Effects in Metals. *Proc R Soc Lon Ser-A* **193**, 484-512 (1948).